In compliance with the
Canadian Privacy Legislation
some supporting forms
may have been removed from
this dissertation.

While these forms may be included
in the document page count,
their removal does not represent
any loss of content from the dissertation.

Investigation of two-dimensional optical formatting for dense wavelength division multiplexing

Frédéric Thomas-Dupuis

Department of Electrical and Computer Engineering
McGill University
Montréal, Québec, Canada
November 2002

A thesis submitted to the Faculty of Graduate Studies and Research in partial fulfillment of the requirements of the degree of Master of Engineering

Your file Votre référence
ISBN: 0-612-88391-4
Our file Notre référence
ISBN: 0-612-88391-4

ABSTRACT

Many multi-channel free-space micro-optical components such as micro-mirror switches and (tunable) vertical-cavity surface emitting lasers (VCSELs) are arranged in two-dimensional arrays. This thesis explores the design, implementation and characterization of a two-dimensional optical wavelength (de)multiplexer designed to interface between wavelength division multiplexing (WDM) optical networks and 2D micro-mirror optical switch, VCSEL or detector arrays. The system uses multifacet gratings to map the light from a traditional optical (de)multiplexer to a 4×16 array with a pitch of 250 μm. The device is 6.05 mm in length and could be fabricated by plastic injection molding. The device successfully performs the two-dimensional mapping. The average efficiency for the device was measured to be 10.4%. The thesis ends with a list of future work that can be done to improve both the theoretical and practical efficiency of the device.

SOMMAIRE

Plusieurs composantes micro-optiques à plusieurs canaux fonctionnant à l'air libre comme les commutateurs optiques à micro-miroirs et les lasers (accordables) sont disposées en matrice à deux dimensions. L'objectif de cette thèse est la conception, l'implantation et la caractérisation d'un (dé)multiplexeur optique à deux dimensions faisant l'interface entre les réseaux optiques de plusieurs longueurs d'onde et les commutateurs optiques à deux dimensions, les matrices de laser ou les matrices de détecteurs. Des réseaux multi-facettes sont utilisés pour transformer la lumière d'un (dé)multiplexeur conventionel à une matrice 4×16 avec une distance de 250 μm entre les cellules. Le système a une longueur de 6.05 mm et peut être dupliqué par moule à injection de plastique. Le système reussit l'opération de transformation et l'efficacité moyenne est de 10.4%. La thèse conclue avec une liste d'améliorations pour augmenter l'efficacité théorique et pratique du système.

Acknowledgements

I would like to thank my thesis supervisor, Prof. Andrew Kirk, for helping me with this thesis and guiding me throughout my masters and a good part of my bachelors degree. Additional thanks go to the many members of the Photonic Systems Group who have helped me with this work. Special thanks go to Marc Châteauneuf, who taught me most of what I know about working in a photonics lab, for help with the preliminary design and assembly of the device. Michaël Ménard for the implementation of the AutoCAD mask generation script and the LabView test software and for help with the CodeV simulations. I would also like to extend my thanks to Prof. Lawrence Chen, Prof. David Plant, Rhys, FredL, MikeV, MikeA, Eric, Maddy, Cibby, Chris and all the other members of the Photonic Systems Group who made these two years most enjoyable.

Merci à Marc Simard pour son aide dans la gestion des ressources humaines.

Merci à Louis et Phil de m'avoir montré les secrets des études graduées (bouf bouf bouf) et de m'avoir divertie pendant tous ces midis!

Les derniers remerciements sont pour mes homies (Francois, Laurent, Crispy, Philou, Stinco, Tyler, Vincent, Max, Matthieu, et Scott), mes parents et mon frère Marc qui m'ont soutenu et encouragé, à l'intérieur et, surtout, à l'extérieur du milieu universitaire, pendant toute ma vie.

This work was funded by the Canadian Institute for Photonic Innovations (CIPI), the Canadian Institute for Telecommunications Research (CITR), and the "Fonds pour la formation de chercheurs et l'aide à la recherche" (FCAR).

TABLE OF CONTENTS

LIST OF FIGURES

LIST OF TABLES

1. INTRODUCTION

1.1 Motivation

The effects of technological improvements in the areas of computing and telecommunications have resulted in a shift towards an information based society. The rapid exchange of information permits cooperation on the planetary scale. News flows more freely and individuals can exchange volumes of text, music, or video with the click of a button. The current shift started in the early 1980's with the introduction of fully digital transmission and switching networks. These networks permit information to be carried in digital form from sender to receiver [1].

Concurrently, optical fiber communications have emerged as a viable transmission medium providing long-haul transmission while offering advantages such as: reduced cost, high bandwidth, low loss, and immunity from electro-magnetic fields [2]. The most important factor influencing the growth of the bandwidth is the increase of multimedia (sound, images, and video) content on the Internet and, in particular, peer-to-peer transfers of this content. The de-centralized nature of peer-to-peer communications creates the need for extremely flexible long-haul and, especially, metro area optical networks. Hence network systems and devices that offer high bandwidth and flexibility are needed to satisfy the requirements for the distribution of this content. Wavelength-division multiplexing (WDM), the technology that enables the combination of wavelengths into the same fiber, can satisfy the requirements for bandwidth and flexibility due to its key features: capacity upgrade by adding wavelengths, transparency to transmission format, wavelength routing, and wavelength switching [3]. The demand for wavelength switching has resulted in a series of initiatives to design and implement all-optical switches [4] using micro-electromechanical systems (MEMS) technology that can provision or protect wavelengths at speeds of milliseconds [5]. MEMS switches are often fabricated in 2D structures to maintain scalability with increasing port-count [6]. However, conventional wavelength (de)multiplexers (such as array waveguide gratings) have a one-dimensional output format. That is, all existing (de)multiplexers technologies

use dispersive effects to provide a direct mapping between wavelength (or frequency), which is a one-dimensional parameter, to a lateral separation of those wavelengths in a one-dimensional spread of frequency.

In addition, optical interconnections are being pushed into the realm of inter-board, inter-rack, and inter-chip communications. Two-dimensional parallel optical interconnects (2D-POIs) enable high-density, high-bandwidth, communications between VLSI chips in computing and switching systems. They can be implemented as single wavelength system or as 2D WDM optical interconnections [7],[8]. Moreover, wavelength tunable VCSELs are being developed [9]. Again, conventional wavelength (de)multiplexers have a one-dimensional output format.

Therefore, it is desired to produce a device that can directly interface between the two-dimensional layout of MEMS switches, optoelectronic VLSI 2D-POIs, or 2D WDM optical interconnections and WDM optical fiber networks. The device could also be used to interface between a fiber and an array of tunable VCSELs or detectors. We have chosen to investigate and develop design techniques for multifacet grating devices for optical telecommunications networks and to evaluate their performance. This particular system, whose specific objectives are discussed in Chapter 2, represents a good target design to test those ideas. Fig. 1 shows a schematic of one-dimensional versus two-dimensional optical wavelength (de)multiplexing.

S. Zhang and W. Yang present, in a US patent, a two-dimensional optical wavelength (de)multiplexer specifically for optical fiber communications [10]. The two-dimensional mapping is performed using a wedged-shaped optical component that is coated with a broad wavelength reflective coating. The fabrication of the wedged-shaped components would necessitate several fabrication steps. In the configuration of [10], the device cannot map to an arbitrary wavelength layout nor interface with MEMS, VCSEL, or detector arrays. To the author's knowledge, [10] is the only other two-dimensional optical wavelength (de)multiplexer to have been designed. No implementation or experimental results have been found for this device.

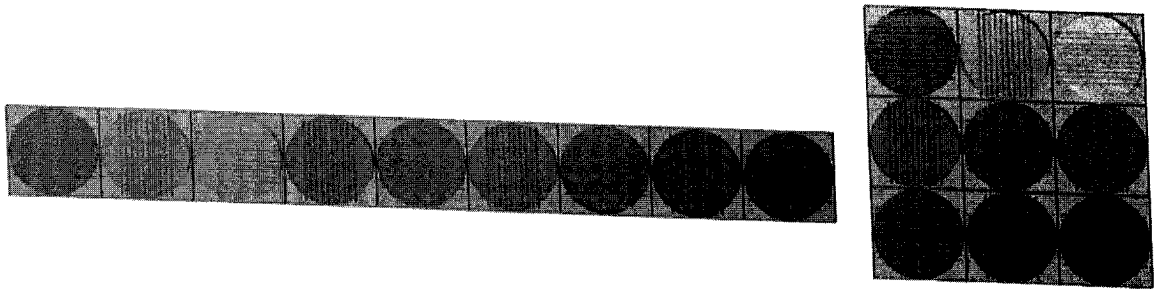

Fig. 1. Schematic of a 1D (left) and 2D (right) distribution of demultiplexed wavelengths

1.2 Principle of operation

As mentioned in Section 1.1, the objective is to (de)multiplex to/from a 2D array to interface between WDM optical networks and MEMS mirror arrays or VCSEL/detector arrays. Currently, (de)multiplexing signals (to a one-dimensional format) uses devices such as spectral gratings, fiber couplers, fiber Bragg gratings, arrayed waveguide gratings (AWGs), grating (de)multiplexers, etc. For DWDM systems, AWGs and grating (de)multiplexers are the most suitable technologies [11]. The objective of (de)multiplexing to/from a 2D array can best be implemented by separating the dispersion operation (which separates/combines the wavelengths) from the redirection operation (which maps the signals to a 2D array.) This method also saves resources as there is no need to re-invent a technology that already functions very well. The redirection operation then maps the linear array of WDM signals to/from a 2D array using multifacet gratings, which deviates the beams (see Section 1.3). The gratings are used as deflection elements instead of dispersive elements. The periods are sufficiently large and the wavelength (of each signal) narrow enough that dispersion should not affect the operation of the device. The mapping can be arbitrarily chosen by etching the proper multifacet grating periods. It will be demonstrated in Chapter 3 that when fabrication limitations are taken into account, it is necessary to search for the optimal grating

configuration and layout. Ideally, the redirection module should simply be attached to the output of a (de)multiplexer and perform the required two-dimensional mapping.

1.3 Overview of diffractive optical elements (DOEs)

A periodic array of diffracting elements, either apertures or obstacles, that has the effect of producing periodic alterations in the phase, amplitude, or both of an emergent wave is said to be a diffraction grating [12]. The grating equation ($p\sin\theta = m\lambda$) relates the wavelength of operation, the period and the angular deviation of the beam for each diffraction order. To maximize the energy in the first order, a blazed grating, such as the one shown in Fig. 2 (b), is used. This type of grating is called "blazed grating" because the shapes of the geometry of the grating grooves are controlled to maximize the diffracted energy into a specific diffraction order [13]. Maximum diffraction efficiency generally occurs when the direction of refraction of the incident beam through a prism (Fig. 2 (a)) equals the direction dictated by the grating equation [13]. (Due to the index of refraction, the groove angle exceeds the blaze angle (Fig. 2 (b) for a transmission grating [13].)

If only one beam needs to be deflected, then a single blazed grating can be fabricated on a silica substrate using a ruling machine [13]. However, in the case of the two-dimensional optical wavelength (de)multiplexer, several beams need to be mapped to a 2D array. Hence, it is desired to fabricate several blazed gratings, with different periods, on the same substrates. However, ruling engines cannot efficiently fabricate gratings that have several different periods. It is therefore necessary to etch the gratings using reactive-ion-etching (RIE) [14]. To do this, the grating profile shown in Fig. 2 (b) is quantized to N-levels such as in Fig. 2 (c) (which has 4-levels.) Then, masks are to be fabricated to allow the etching of several grating configurations on the same substrate. These are called multifacet gratings or diffractive optical elements (DOEs) because they contain several grating facets with different periods and orientations.

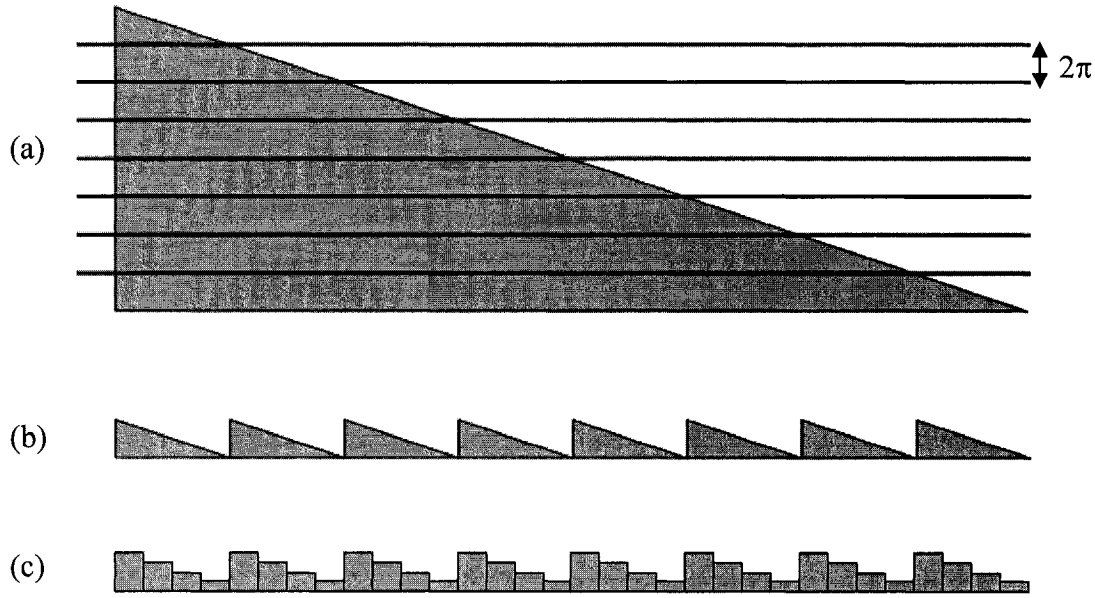

Fig. 2. Phase profile slicing:
(a) refractive phase profile; (b) slicing in 2π layers; (c) 4-level DOE

1.4 Thesis outline

Chapter 2 will present the specific objectives of the project including specifications and requirements for both the redirection module and the dispersion module. Chapter 3 will explain the design of the redirection module. Chapter 4 provides the simulation and optimization results which determine the assembly tolerances of the redirection module. Chapter 5 explains the design, implementation and characterization of a free-space grating dispersion module that can be interfaced with the redirection module to produce the two-dimensional optical wavelength (de)multiplexer. Chapter 6 demonstrates the packaging, fabrication, and assembly of the redirection module. Chapter 7 presents the performance results. Finally, Chapter 8 details future work to improve the performance of the device.

1.5 Original contributions

The original contributions presented in this thesis are:

1. The design of an optical reformatter for mapping a linear array of 64 multi-wavelength beams to a two-dimensional array. It is to the author's knowledge to be the first time that such as device has been conceptualized.
2. Designing the reformatter to interface between tuneable laser arrays, detector arrays, MEMS micro-mirror and free-space grating dispersion modules used in DWDM optical networks.
3. The use of cascaded multifacet diffraction gratings to perform the optical reformatting task
4. The development of an optimization approach which is used to obtain a layout that maximizes the average grating period and which respects fabrication limits.
5. The simulation of the device to determine its performance characteristics and its assembly tolerances
6. The assembly of the reformatter module.
7. The testing of the reformatter module.

1.6 References

[1] J.E. Midwinter, Photonics in Switching, Volume 1, Background and Components, Boston, Academic Press Inc., 1993, p.1-16.

[2] Lee Shi-Shen, Huang Long-Sun, Kim Chang-Jin, M.C. Wu, "Free-space fiber-optic switches based on MEMS vertical torsion mirrors", Lightwave Technology, Journal of , Volume: 17 Issue: 1 , Jan. 1999 Page(s): 7 –13.

[3] G. Keiser, Optical Fiber Communications, 3rd edition, McGraw-Hill, (2000), Chap. 10.

[4] J. Lacey, "Optical switching and its impact on optical networks", Optical Fiber Communication Conference and Exhibit, 2001. OFC 2001, Volume 2, 2001. Pages: TuW3-1 – TuW3-3.

[5] J. A. Walker, "The future of MEMS in telecommunications networks", Micromech. Microeng. 10 No 3 (September 2000) R1-R7.

[6] L.Y. Lin and E.L. Goldstein, "Opportunities and challenges for MEMS in lightwave communications", IEEE Journal of Selected Topics in Quantum Electronics, Vol. 8, p 163, (2002).

[7] A.E. Willner, C.J. Chang-Hasnain, J.E. Leight, "2-D WDM optical interconnections using multiple-wavelength VCSEL's for simultaneous and reconfigurable communication among many planes.", IEEE Photonics Technology Letters, Vol. 5, Issue 7, pp 838-841, (1993).

[8] J.J. Yoo, A.E. Willner, "A performance and implementation comparison of bidirectional and dual bus 2-D WDM multiple-plane optical interconnections with row-column multihop network structures", IEEE Journal of Lightwave Technology, Vol. 19, Issue 6, pp. 801-809, (2001).

[9] C. Hasnain, "Tunable VCSEL", IEEE Journal on Selected Topics in Quantum Electronics, Vol. 6, Issue 6, Nov-Dec, pp 978-987.

[10] S. Zhang and W. Yang, "Compact double-pass wavelength multiplexer-demultiplexer having an increased number of channels," US Patent #6108471, (2000).

[11] E. S. Koteles, "Integrated Planar Waveguide Demultiplexers for High Density WDM Applications", in Wavelength Division Multiplexing, Ray T. Chen, Louis S. Lome, Proc SPIE Vol. CR71, 3-32 (1999).

[12] E. Hecht, Optics, 3rd edition, Addison Wesley Longman Inc., (1998), Chap. 10.

[13] C. Palmer, Diffraction Grating Handbook, Richardson Grating Laboratory, 4th edition, (2000).

[14] B. Kress and P. Meyrueis, Digital Diffractive Optics: An Introduction to Planar Diffractive Optics and Related Technology, John Wiley & Sons, (2000).

2. OBJECTIVES OF THE PROJECT

2.1 Introduction

This chapter presents the objectives and the goals of the project. Section 2.2 presents the requirements and the objectives of the two-dimensional optical (de)multiplexer. Section 2.3 and Section 2.4 discuss, more specifically, the requirements for the redirection module and the dispersion module, respectively.

2.2 Requirements and objectives

The objective of the project, as described in Chapter 1, is to spatially (de)multiplex to a two-dimensional array several wavelengths emanating from a fiber. Evidently, the operation could be carried in reverse as a multiplexer. The two-dimensional (2D) optical wavelength (de)multiplexer comprises two distinct components: the *dispersion module* and the *redirection module*. A schematic of the system is shown in Fig. 3. The dispersion module can be implemented using a conventional optical demultiplexer such as those discussed in Section 1.2. Note that this device is more compact than conventional (de)multiplexers due to a reduced spatial separation at the output of the dispersion module (the input of the redirection module has a smaller pitch between wavelengths than a linear array of fibers.) The redirection module transforms the linear array into a 2D array with the proper output pitch.

The objectives of the project are:

- 64 wavelengths
- 100 GHz spacing on the ITU grid
- C band
- 250 μm output pitch
- Low Loss
- Optimized Length
- Easily Scalable

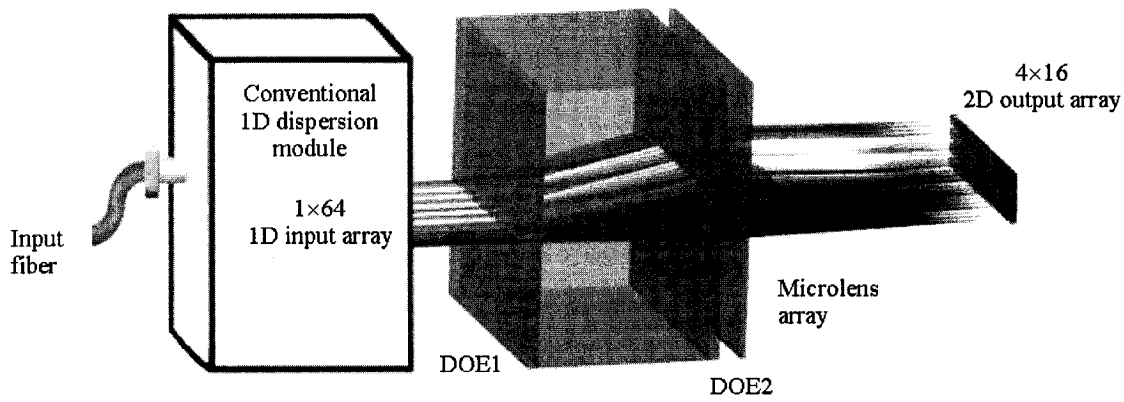

Fig. 3. Schematic of the 2D optical wavelength (de)multiplexer

2.3 Dispersion module requirements

The dispersion module will take an input fiber containing all wavelengths to be demultiplexed and separate each of them into a linear array of beams, which are directed onto the first diffractive optical element, the input of the redirection module. To minimize loss and crosstalk, each beam must illuminate one facet of the first element of the redirection module with no power overlap between them.

The input to the dispersion module is a fiber with 64 wavelengths with a 100 GHz spacing on the ITU grid. At the output, the wavelengths must be spatially separated by 62.5 μm (250 μm output pitch divided by 4 which provides $1/4^{th}$ scaling to the dispersion and redirection modules.) As will be discussed in Chapter 5, the free-space grating technology does not allow for a linear spatial separation of wavelengths. Hence, only the first wavelength will have 62.5 μm spacing and the others will have separations of greater than 62.5 μm. The impact on the redirection module is discussed in the next section. In addition, each beam must have a Gaussian beam waist, on the first diffractive optical element, of 20.8 μm, which corresponds to 99% power transfer.

Chapter 5 shows the design and implementation of a grating based free-space optical demultiplexer compatible with the redirection module whose design is presented in Chapter 3. Any other type of demultiplexer can be used as long as it satisfies the above requirements. The use of a device such as an AWG or etched grating demultiplexer

would also have the advantage of a constant lateral spacing between wavelengths which would make the redirection module perfectly scalable.

2.4 Redirection module requirements

The redirection module uses two multi-facet diffractive optical elements (DOEs) to map a linear array of wavelengths to a 2D array. The first DOE (DOE1) redirects the incoming light beam to the correct spatial position of the 2D array whilst the second DOE (DOE2) transforms the propagation angle such that it is parallel to the optical axis, or, perpendicular to the plane of the substrate. Next, a microlens array is used to relay the diverging light beam.

The input to the redirection module is 64 spatially separated wavelengths. The pitch between wavelengths is 62.5 μm and greater (see Appendix A for details). Note that the pitch is not exactly 62.5 μm due to the non-linearity of the dispersion module designed to be compatible with the redirection module. The output of the redirection module is a 4×16 array with an output beam separation of 250 μm, which is compatible with typical MEMS, VCSEL, or detector pitches. The facet size of the DOEs on the input (DOE1) is 62.5 μm and on the output, it is 250 μm. The layout of the facets of the DOEs is such that each set of 16 wavelengths is (de)multiplexed to a 4×4 array making the device scalable 16 wavelengths at a time, while scaling in width four times less than a 1D demultiplexer, without an increase in length.

2.5 Summary

The two-dimensional optical (de)multiplexer requirements and objectives were presented. The device must (de)multiplex 64 wavelengths spaced by 100 GHz on the ITU grid in the C-band to a 4×16 output array with a 250 μm pitch, which is compatible to MEMS, VCSEL, and detector pitches. This particular system represents a good target design to investigate and develop design techniques for multifacet grating devices for optical telecommunications networks.

3. DESIGN OF THE REDIRECTION MODULE

3.1 Introduction

This chapter presents the design of the redirection module. Section 3.2 explains the functioning of the module and the diffraction grating design. This is followed by a list of constraints imposed on the design. Section 3.4 explains the MatLab design script used to optimize the length of the system. Section 3.5 explains the substrate layout. Next the parameters of the microlens array are presented. Finally, a scalar efficiency analysis of the device is presented.

3.2 Diffraction grating design

As explained in Chapter 2, the redirection module uses two multi-facet diffractive optical elements (DOEs) to map a linear array of wavelengths to a 2D array. The first DOE (DOE1) redirects the incoming light beam to the correct spatial position of the 2D array. The second DOE (DOE2) is used off-axis to transform the propagation angle such that it is parallel to the optical axis of the device. Fig. 4 illustrates the reformatting operation.

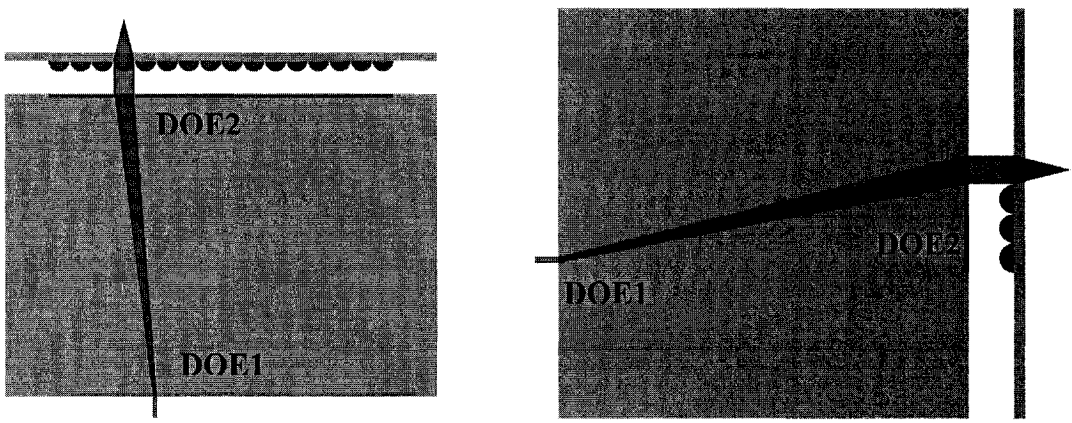

Fig. 4. Illustration of reformatting operation (left: top-view; right: side-view)

The beam redirection is given by the grating equation [1]:

$$m\lambda = p_i \sin\theta_i \tag{1}$$

where m is the diffraction order; λ is the wavelength of operation; p_i is the period of the grating and θ_i is the deflection angle (from the normal). This equation is only valid for one dimension. To deflect in θ_x and θ_y simultaneously, two period components (p_x and p_y) are needed. The absolute period of the grating can also be defined by an absolute period p and its corresponding angle of rotation θ_G:

$$p = p_x p_y / (p_x^2 + p_y^2)^{1/2} \tag{2}$$

$$\theta_G = \tan^{-1}(p_y / p_x) \tag{3}$$

where p_x is the component of the period in x; p_y is the component of the period in y; p is the absolute period; and θ_G is defined as being the angle of rotation from the x-axis. Hence, a grating which has a period in x (p_x) of infinity will have a θ_G of zero. A grating whose period in y (p_y) is infinity will have a θ_G of 90°. Fig. 5 illustrates a typical facet.

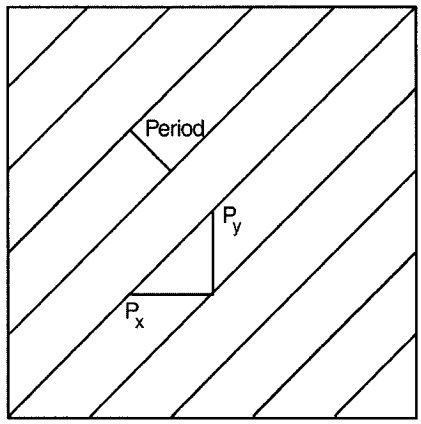

Fig. 5. Illustration of a typical grating facet

3.3 Design constraints

To maximize efficiency, it is desired that 99% of the light shine onto the grating facets. Hence, for Gaussian beams, it is required the beam radius be $1/3^{rd}$ of the facet size. As presented in Chapter 2, the facet size of DOE1 and DOE2 are set to be 62.5 μm and 250 μm, respectively. Hence, the waist, at DOE1, of the Gaussian beam must be 20.8 μm. The following equations model the expansion of a Gaussian beam [2]:

$$\omega(z) = \omega_o \left[1 + (z/z_R)^2\right]^{1/2} \tag{4}$$

$$z_R = \pi\omega_o^2/\lambda \tag{5}$$

where z is the distance from the waist, which, in this case, is at DOE1; ω_o is the beam waist size; $\omega(z)$ is the beam radius at distance z; and λ is the wavelength of operation. It is determined from equation (4) and (5) that the maximum length of the module for 99% power on the grating facets, at a wavelength of 1550 nm, is 3.4 mm. An in depth analysis

of Gaussian beam propagation is performed in Chapter 4. The above mentioned values are used as a basis for the design.

The gratings are used in the first order (positive or negative) to maximize efficiency. For the purposes of the design, it was defined that a grating used in the -1 order has its phase levels inverted. This insures that the strongest light intensity is directed in the proper direction. Essentially, DOE2, which transforms the propagation angle such that it is parallel to the optical axis, is always used in the -1 order while DOE1 is used in order 1. Therefore, DOE2 inverts the operation of DOE1.

Two limitations are placed on the absolute period p and one limitation on the resolution of the components p_x and p_y. First, the minimum period is dependent on the number of levels and the minimum feature size that can be etched by the vendor. The minimum feature size that can be etched is 1.5 μm. For cost purposes, only four levels are etched. This constrains the minimum period to be 6 μm (4 × 1.5 μm). It should be noted that there is a tradeoff between the number of levels used and the largest deflection angle that can be implemented in the system. Considering that the minimum features size (which can be etched by the vendor) is constant at 1.5 μm, the addition of levels increases the minimum period that can be implemented which, consequently, reduces the maximum angle of deflection that can be implemented in the system. It will be demonstrated in the Section 8.3 that the optimal number of phase levels is 8. The maximum period is given by the size of the smallest facet divided by three. This ensures that enough periods are illuminated (3) for the plane wave approximation to be valid [4]. Finally, all values of p_x and p_y must be in increments of 0.1 μm due to the resolution of the fabrication process. As a result, it is not possible to obtain an arbitrary deflection angle as the solutions are quantized. This is illustrated in Fig. 6. In addition, longer systems will have a higher misalignment due to this quantization.

The linear input array is defined as having 64 grating facets as shown in Fig. 7. Chapter 2 defined the lateral separation between facets to be 62.5 μm. Considering that the grating-based dispersion module does not have a linear output, the actual separation between facets varies between 62.5 and 67.1 μm as listed in Appendix A. The facets are

numbered from 1 to 64 and correspond to the Appendix. The coordinate system used for the optimization is defined as having the origin at the center of the first facet.

The two-dimensional output array also has 64 grating facets. They are arranged on 4×16 array with a 250 μm pitch between facets as shown in Fig. 8. The relative positioning (see Fig. 9) of the input and output arrays is undefined. Note that each set of 16 wavelengths is reformatted to a 4×4 array so that the device can be scaled 16 wavelengths at a time without an increase in length. The optimization routine will be used to find the positioning of DOE1 with respect to DOE2 that gives the device the shortest possible length.

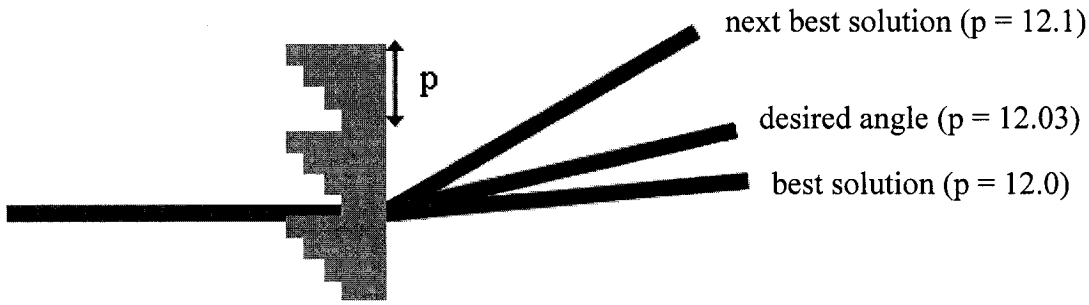

Fig. 6. Illustration of the quantization of the deflection angle due to the maximum resolution of the period

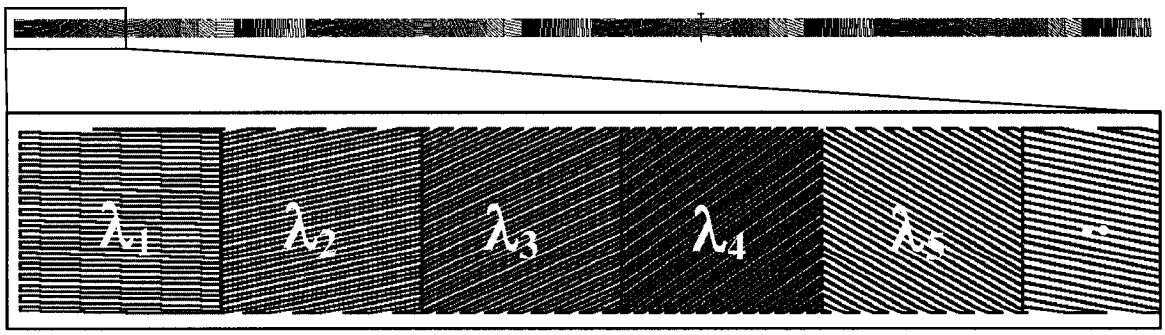

Fig. 7. Illustration of the wavelength mapping of the 64 grating facets of DOE1

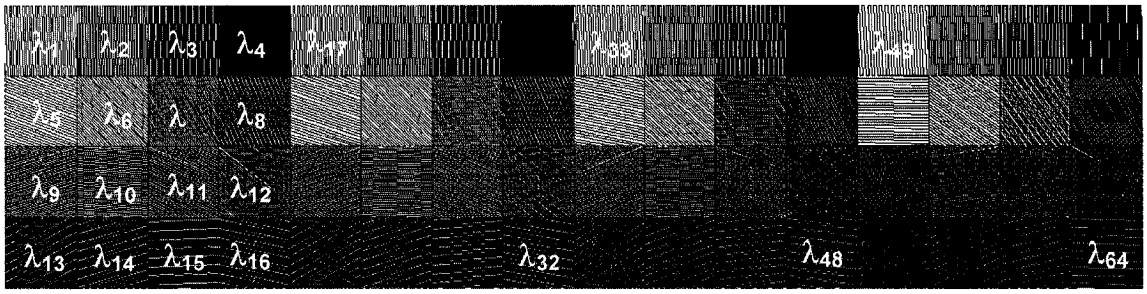

Fig. 8. Illustration of the wavelength mapping of the 64 grating facets of DOE2

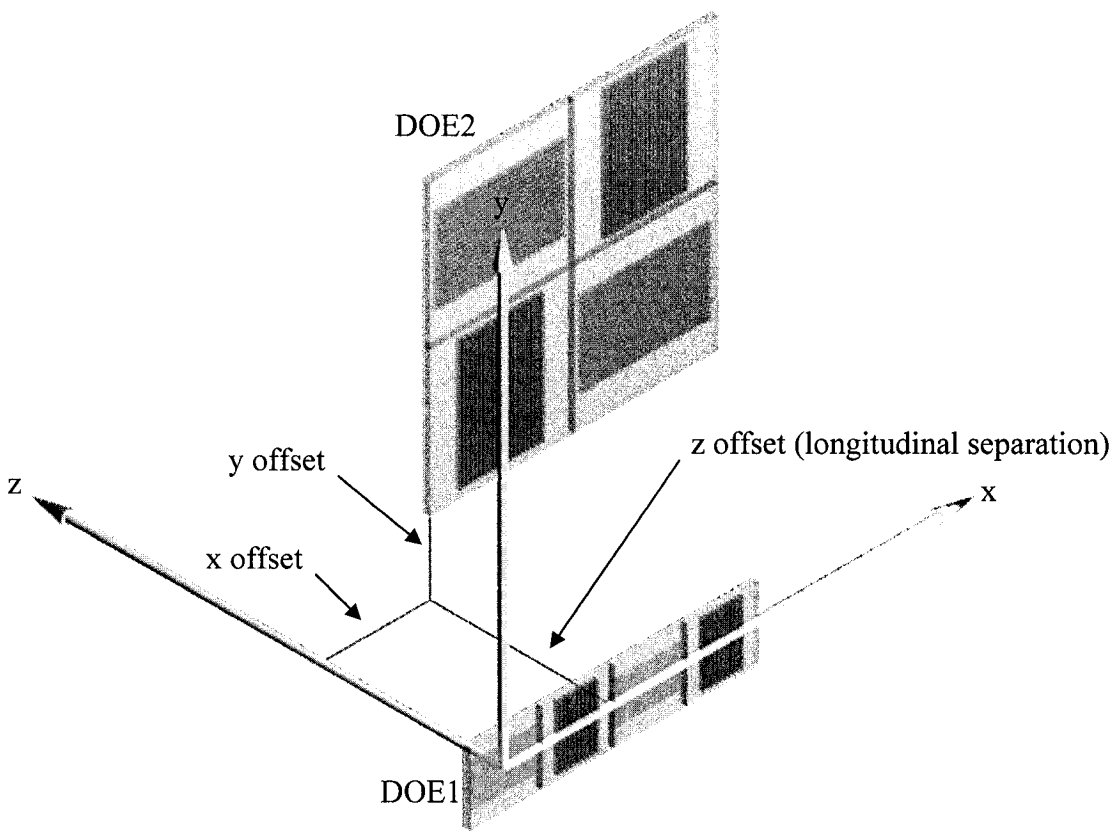

Fig. 9. Illustration of the coordinate system used for the design of the redirection module (not to scale, 4 wavelengths only)

3.4 Optimizing for length

The goal of the optimization script is to determine the positioning of the DOEs with respect to each other and the grating periods that generate the least positional error at the output of the redirection module. Fig. 9 shows the three positional parameters that are to be determined by the optimization routine: the x-offset, the y-offset, and the longitudinal separation of the DOEs. The primary goal of the routine is to find the positioning that gives the device the shortest length to avoid clipping at DOE2 due to Gaussian beam expansion. Again, for 99% efficiency, the device is constrained to a maximum length of 3.4 mm.

The flow chart of the optimization script is shown in Fig. 10. The script has five major functions. The arrows in the diagrams indicate the interaction between the functions. Essentially, the *FabricationPeriod* is the only function that does not "feedback" into the optimization routine. The functions are explained in the following paragraphs.

CoordinateSystem: This function reads from a file the coordinates of the input array and the layout of the output array (i.e. the 4×16 array with a 250 μm grating pitch.) It receives, from the top of the chain, the *optimization* function, the longitudinal separation and the x, y offset of DOE1 and DOE2. From all this data, the function generates a matrix which has the coordinates of all 128 grating facets in the XYZ space.

GetAngle: This function has as an input the matrix generated by *CoordinateSystem*. It generates a matrix of all the angles (both θ_x and θ_y) needed to deviate the beams from the corresponding facets on the input and output array.

GetPeriod: This function has a file input of the wavelengths associated with each facet and an input from *GetAngle* of the matrix of angles needed to redirect the beams. It uses equation (1) to generate the grating periods of all 128 facets.

Optimization: This function controls all the above mentioned functions by iterating them for longitudinal separation and x,y offset. It also verifies that the grating periods satisfies the constraints (20. $8 > p > 6$) and generates the result files shown in Fig. 11 and Fig. 12. Fig. 11 shows a color map of the shortest solution versus x and y offset.

Fig. 12 shows a plot of the maximum and minimum grating periods versus length for a redirection module whose x offset is 228 μm and y offset is -890 μm. The blue line represents the maximum period used in a design (versus length.) The brown line represents the minimum period used in the design (versus length.) The graph demonstrates that, at a length of 3480 μm, a solution exists where the maximum and minimum periods lie between the constraints of 6 μm and 20.8 μm (the black lines).

FabricationPeriod: This function has as an input the shortest solution found by the optimization function. It finds the best approximation to all p_x's and p_y's so as to minimize the positional error of the beam on DOE2. It outputs the list of all grating periods needed to implement the redirection module. This list is in Appendix B.

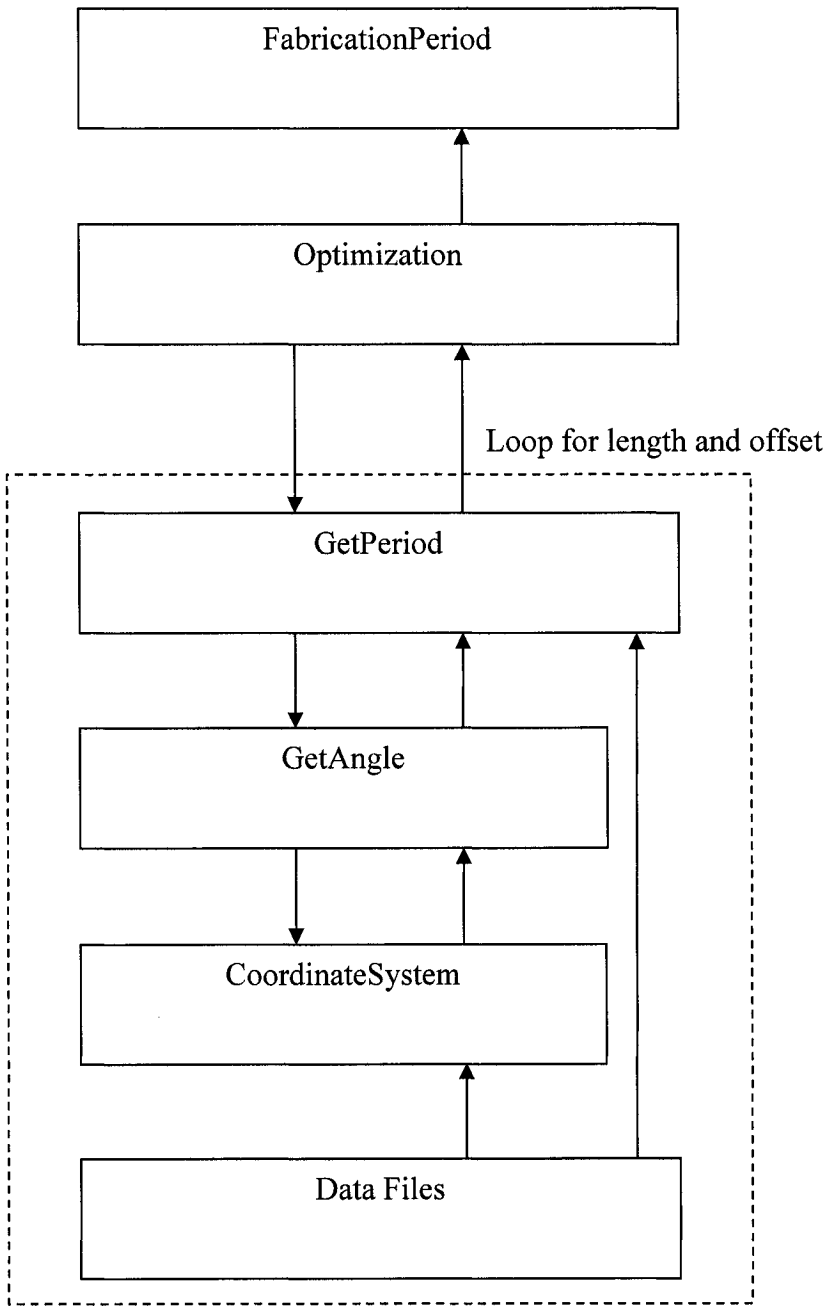

Fig. 10. Flow chart of the optimization script

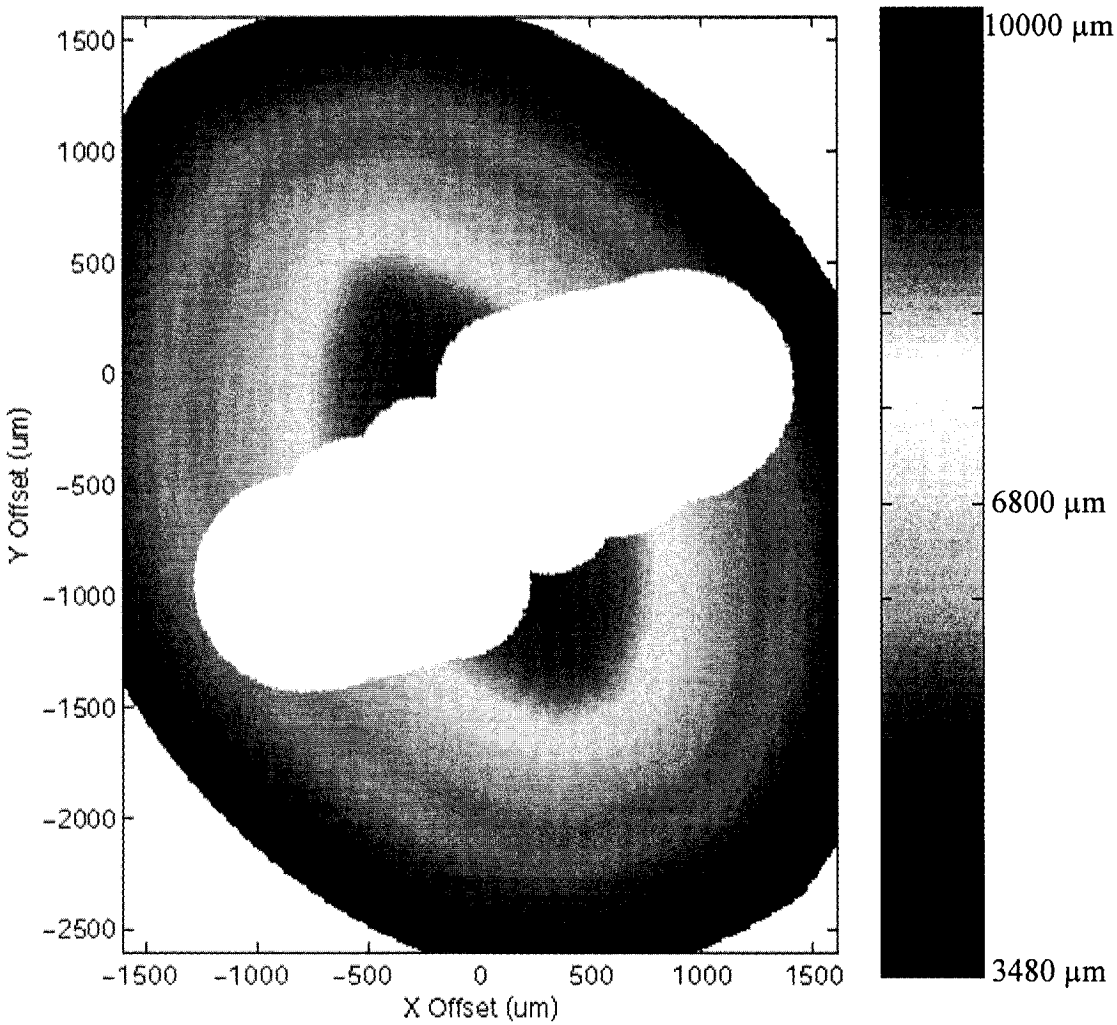

Fig. 11. Color map of shortest solution versus x and y offset

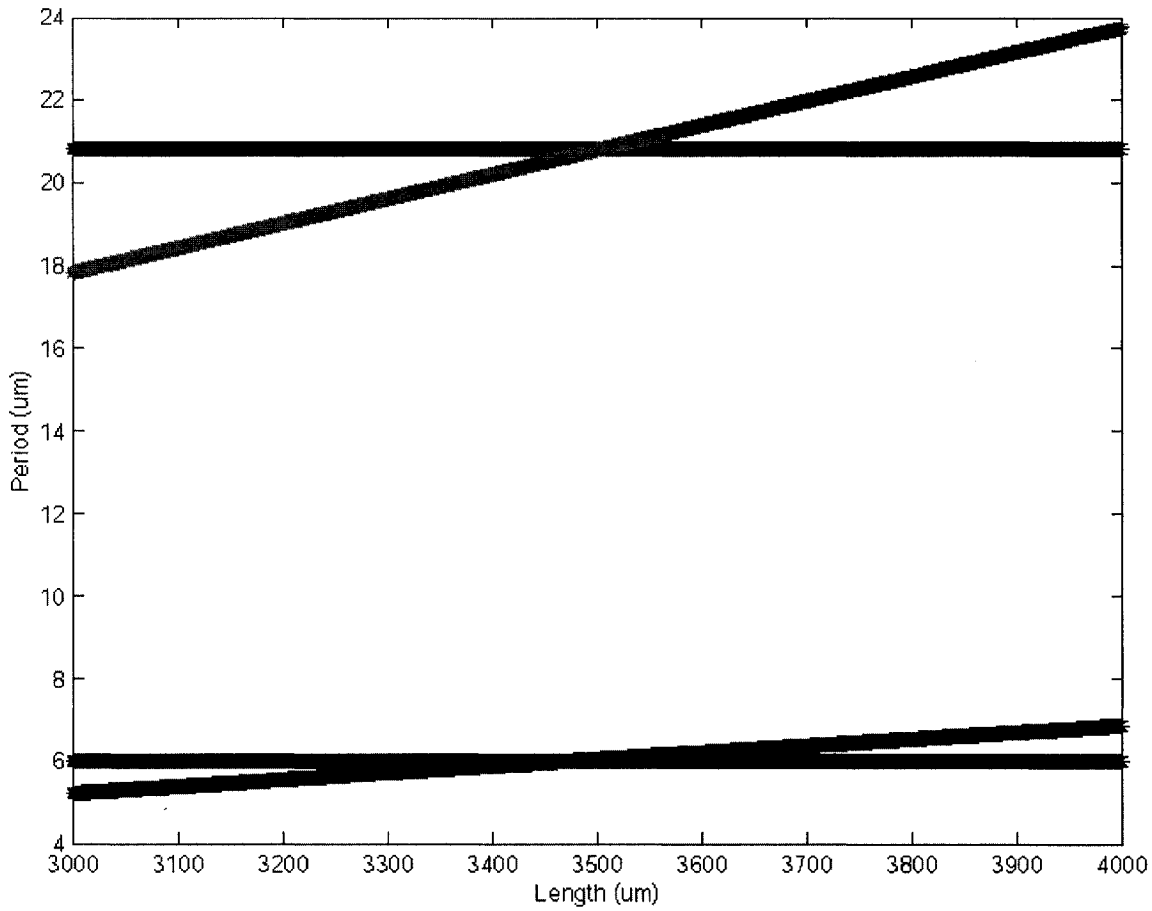

Fig. 12. Maximum and minimum period versus length
for an offset of x = 228 and y = -890 μm
(black = design constraints; Blue = maximum period; Brown = minimum period)

The maximum length (L_{max}) is proportional to the facet size of DOE1, which sets an upper limit on the grating period. Hence a larger facet size will permit a larger period and thus a smaller deflection angle allowing the separation between DOEs to be larger. The minimum length of a system (L_{min}) is inversely proportional to the maximum deflection angle which is dependent on the minimum feature size of that can be etched and the number of grating phase levels. L_{min} is also proportional to the output pitch of the grating facets at DOE2. Hence, a large output pitch needs a long length for a constant maximum deflection angle.

3.5 Substrate layout and preliminary specifications

The substrate layout is shown in Fig. 13. The DOEs used for redirection are shown in blue, the interferometric lenses used for alignment are shown in red, and the metal is shown in black (more information is provided in Section 6.4.) Section 3.3 demonstrated the layout of the wavelengths within the DOEs. Again, note that each set of 16 wavelengths is (de)multiplexed to a 4×4 to make the device scalable 16 wavelengths at a time without an increase in length. The relative positioning of the DOEs is 228 μm in x, -890 μm in y, and 3480 μm is z. The coordinate system is shown in Fig. 9. Note that the wavelength mapping was a constraint that was not optimized here. Section 8.2 explains that optimizing the wavelength mapping can lead to a more efficient design.

The interferometric lenses are placed far away from the DOEs to permit high precision rotational (as well as lateral) alignment of the substrates with respect to each other. Finally, the metal deposition surrounding the DOEs is used for two purposes. Firstly, the thin layer of metal which is deposited (10 μm) is used as a spacer for the microlens array which is positioned on top of the metal. Second, they are used as barriers to prevent the UV glue (used to cement the microlens array and the substrate together) from infiltrating itself to the DOEs.

Moreover, the layout is such that the substrates are used back-to-back. This is done for two reasons: First, the substrates are longitudinally separated by gluing them on opposite ends of a glass spacer. To avoid depositing glue on the features of the grating, they are placed on the outside. Second, it verifies that the system could be manufactured using plastic injection molding as all its diffractive features are on the outside.

The preliminary specifications for the fabrication of the device are as follows. The device has a distance between DOEs, in air, of 3.48 mm. For fused silica (n = 1.44), the total length becomes 5.01 mm. Assuming each substrate (DOE1 and DOE2) are 1 mm thick, then a 3.01 mm glass spacer will be needed to ensure the correct longitudinal separation (see Chapter 4 and Chapter 6 for more details.)

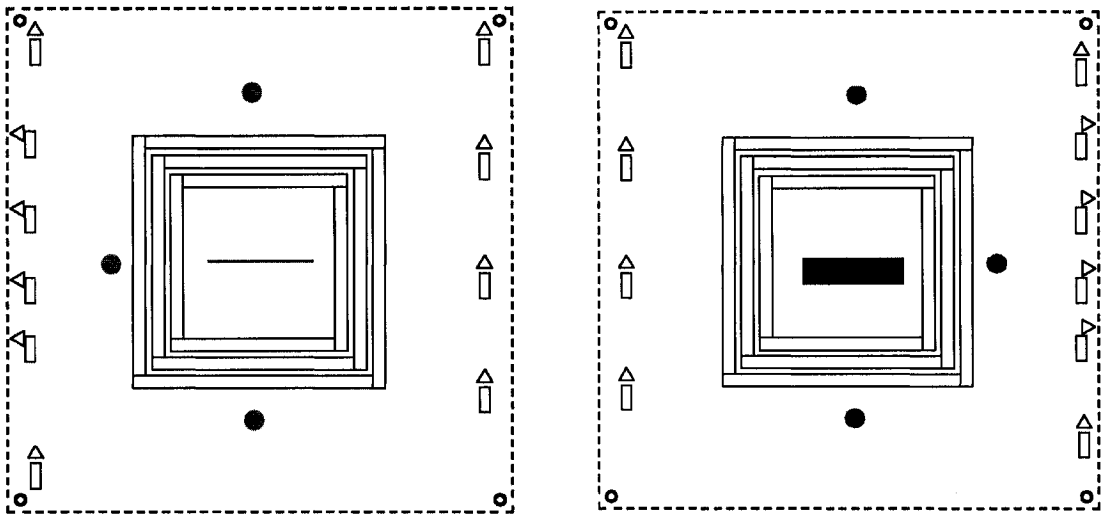

Fig. 13. Substrate layout (left: DOE1; right: DOE2)

3.6 Microlens array

The microlens array must relay the diverging beam onto a detector or MEMS array as shown in Fig. 3 and Fig. 4. The selected microlens array has a 776.1 μm focal length at 550 nm. Simulations show that the focal length becomes 803.8 μm at 1550 nm. Gaussian beam propagation predicts that the beam waist at the output of the device, after being relayed by the microlens, is 6.0 μm.

3.7 Scalar efficiency analysis

After the module was a designed, a scalar efficiency analysis was performed to predict the performance of the device. The scalar efficiency equation is dependent on the number of phase levels in the grating [3]:

$$\eta = [\sin(\pi/N)/(\pi/N)]^2 \tag{6}$$

where η is the efficiency and N is the number of phase levels. Fig. 14 shows a graph of efficiency versus the number of phase levels in the grating. The redirection module's gratings have 4 levels and therefore, scalar efficiency theory predicts an efficiency of 81%. Hence, scalar efficiency predicts that the device (2 gratings) has an efficiency of 66%.

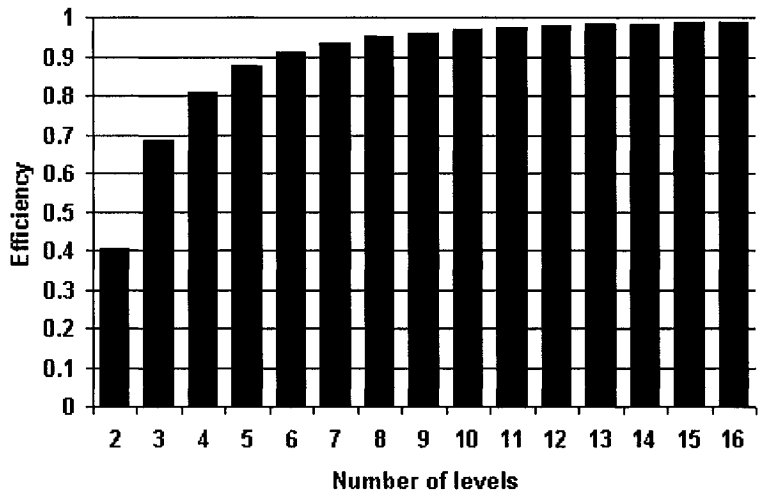

Fig. 14. Efficiency versus number of phase levels for a grating

3.8 Summary

Optimization of the design leads to a redirection module that is 3.48 mm long (in air) which can be scaled in increments of 16 wavelengths. The layout of the wavelengths is such that each section of 16 wavelengths is rasterized, on a 2D array, to a 4×4. The relative positioning of the DOEs is 228 μm in x, -890 μm in y, and 3480 μm in z according to the coordinate system shown in Fig. 9. Scalar efficiency predicts that the device will have 66% efficiency (with each grating having 81% efficiency.)

3.9 References

[1] E. Hecht, Optics, 3rd edition, Addison Wesley Longman Inc., (1998), Chapter 10.

[2] B.E. A. Saleh, M.C. Teich, Fundamentals of Photonics, Wiley & Sons Inc., New York (1991), Chapter 7.

[3] H. P . Herzig, Micro-Optics: Elements, systems and applications, Taylor and Francis, (1997).

[4] J.W. Goodman, Introduction to Fourier Optics, McGraw-Hill, (1996).

4. SIMULATIONS AND OPTIMIZATION

4.1 Introduction

This chapter presents the optimization and simulations of the design of the redirection module. The analysis is performed to determine the alignment tolerances for which the system can be assembled. Chapter 3 explained the MatLab computer script used to find the shortest possible solution that would permit the redirection of 64 wavelengths onto a 2D array. In this chapter, the design that was presented in Chapter 3 is simulated and optimized so as to evaluate and minimize misalignment of the output light beams and the components. In the design, the distance between DOEs was determined to be 3480 μm with an x-decenter of 228 μm and a y-decenter of -890 μm. First, a sensitivity analysis is performed to determine the alignment tolerances of the components. The maximum misalignment is defined by setting a minimum power through the "aperture" (facet of DOE2), which is calculated using Gaussian beam analysis. Second, due to the variance in optical path length of the 64 wavelengths, Gaussian beam propagation is performed for all 64 wavelengths. Finally, a software called GSolver™ is used to perform rigorous coupled wave analysis (RCWA) of the diffraction efficiency to predict the losses of the gratings and the redirection module.

4.2 Misalignment analysis

The maximum tolerable misalignment of the diffractive substrates (DOE1 and DOE2) is defined by determining the maximum *average of the absolute error* (from now on referred to as *absolute error*). Any positional error at DOE2 will induce beam clipping which will cause losses and crosstalk. This error is calculated by taking the absolute positional error at DOE2 for all 64 wavelengths and taking the average. A value for the amount of maximum *average loss* due to output beam positional error is arbitrarily established to be 3%. Hence, using [1]:

$$\text{Power} = 1\text{-}\exp[-2a^2/w^2(z)] \quad (7)$$

where *Power* is the percent of the power through the aperture of size *a* when the beam diameter is *w(z)*. It is found that, for 3% loss, the maximum "average error" for the beam misalignment at DOE2 is ± 6 μm.

To evaluate the component misalignment that causes the average beam positional error at the output, a ray-tracing software, CodeV ®, was used. Essentially, a model of the redirection module was implemented in the software and the beam positional error at DOE2 was evaluated for all 64 wavelengths for misalignments of the fused silica diffractive substrate (DOE1 and DOE2.) The chief ray position at DOE2 was calculated by CodeV ® and compared to the position of an ideal system. The minimum, average, and maximum beam positional error is graphed with respect to component misalignment. The following sub-sections show the results for angular, lateral, rotational and longitudinal misalignment of the diffractive substrates. Also, the effect of microlens misalignment is studied. Finally, the beam positional error due to the misalignment of the input beam to the redirection module is demonstrated. In all, 50 scripts were written in CodeV ® to simulate these misalignments. To keep this chapter brief, only the important results are shown.

4.2.1 Angular misalignment

Angular misalignments correspond to the pitch and yaw displacements of the diffractive substrates with respect to each other. Note that pitch is defined as the roll around the x-axis while yaw is defined as the roll around the y-axis. It is controlled by the flatness and parallelism of the spacer and diffractive substrates. The beam positional error at DOE2 is not very sensitive to angular misalignments. Fig. 15 shows that a misalignment of ±1° induces an average error of less than 1 μm. Misalignment errors in yaw are larger due to the facets' layout on DOE1. Since they are laid out on a line along the x-axis, change in pitch does not displace the center of any facets. However, misalignments in yaw change the position of the facets at both extremes of DOE1.

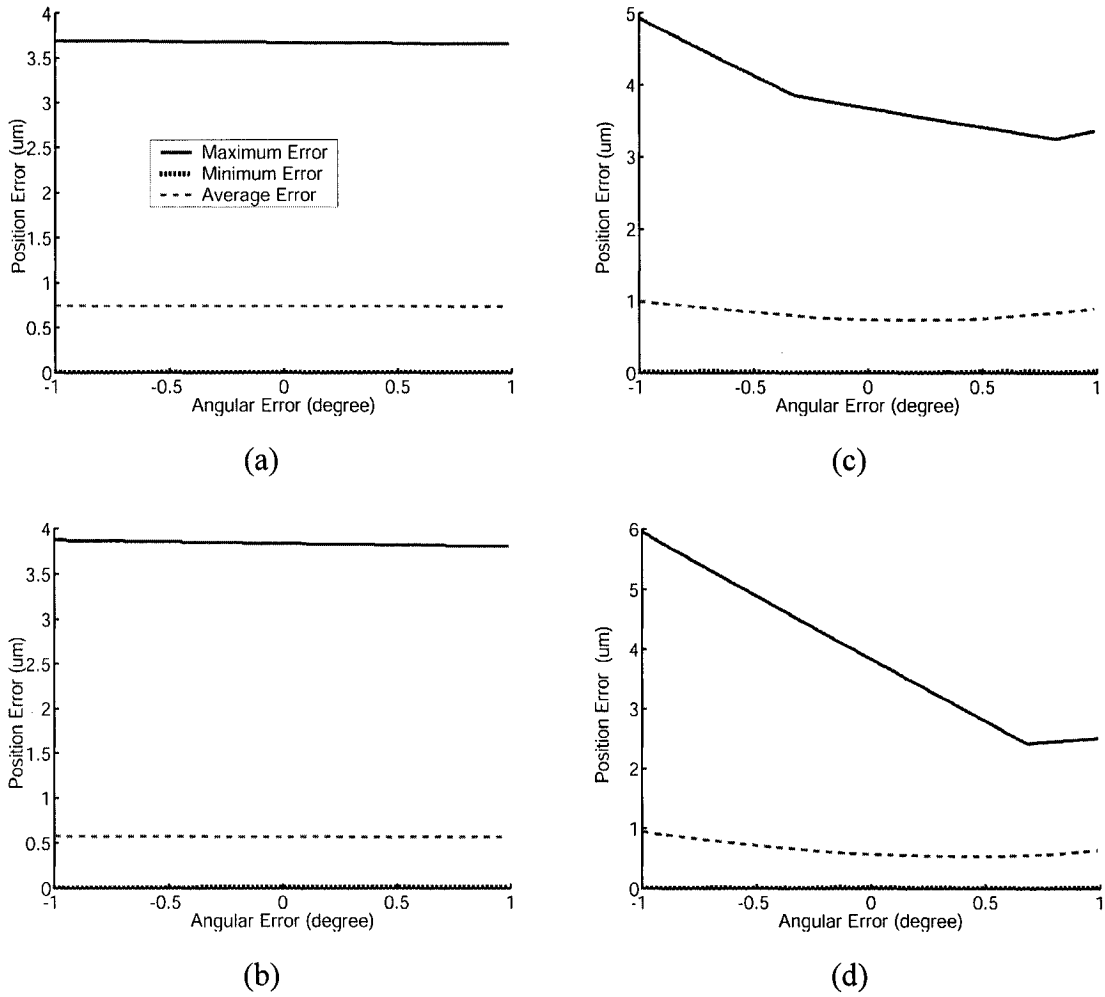

Fig. 15. Beam position error at the image plane vs angular misalignment of DOE1:
(a) error in x for pitch misalignment;
(b) error in y for pitch misalignment;
(c) error in x for yaw misalignment;
(d) error in y for yaw misalignment.

4.2.2 Lateral and rotational misalignment

The lateral and rotational misalignment correspond to the displacement in x and/or y of the diffractive substrates with respect to each other. This is controlled by the precision of the interferometric lens alignment technique used for alignment and

discussed in Chapter 6. Fig. 16 shows the lateral misalignments of DOE1 and the induced positional error at DOE2. DOE2 misalignments are not considered because all other misalignments were induced relative to its position. This is because DOE2 determines the optical axis at the output of the system. From the graphs above, one can see that a misalignment of ±5 μm induces an average beam position error of ±2 μm. The average positional error never drops to zero, when the system is perfectly aligned, because the photolithographic fabrication technique limits the resolution of the period to 0.1 μm (see Chapter 3 and Chapter 6). Note that the maximum error curve does not follow the same trend as the average error curve because it is dominated by the wavelength with the longest optical path length. Rotational misalignment is the combination of two lateral misalignments (x and y) and has the same alignment tolerances as the lateral positioning. Chapter 6 explains how the same technique that is used to laterally align the substrates is used to satisfy the rotational constraint.

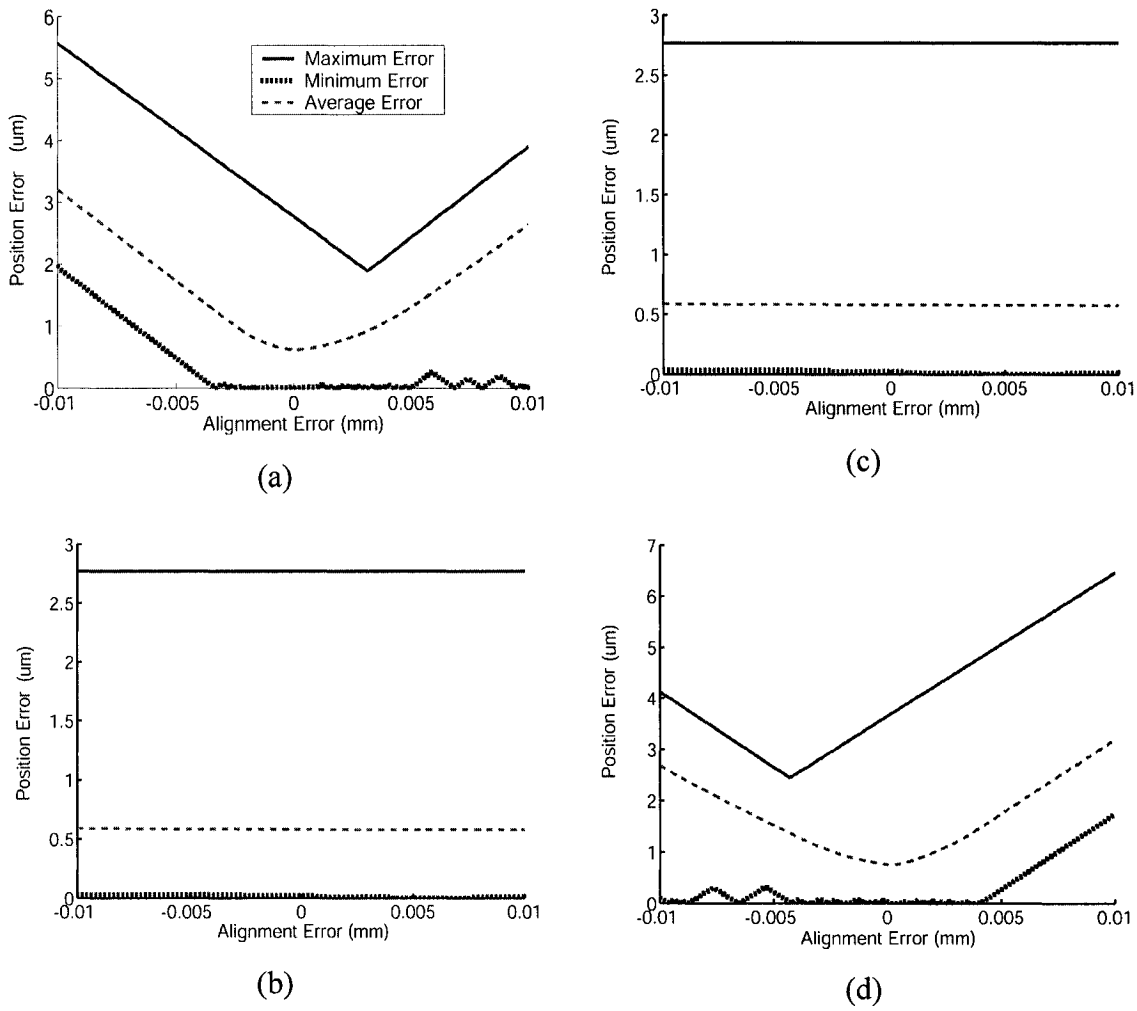

Fig. 16. Beam position error at the image plane vs lateral misalignment of DOE1:
(a) error in x for x misalignment;
(b) error in y for x misalignment;
(c) error in y for x misalignment;
(d) error in y for y misalignment.

4.2.3 Longitudinal misalignment

The longitudinal misalignment corresponds to the error in distance between the two diffractive substrates. This is controlled by the precision with which the spacer and substrate can be manufactured. Fig. 17 shows that a tolerance of ±50 μm provides a

maximum average beam position error of ±2 μm. In addition, the graph shows that the optimum length of the spacer is not 3.01 mm (as stated in Section 3.5) but 3.05 mm, where the average error is lowest. Hence, an increase in length of the spacer decreases the error in the system.

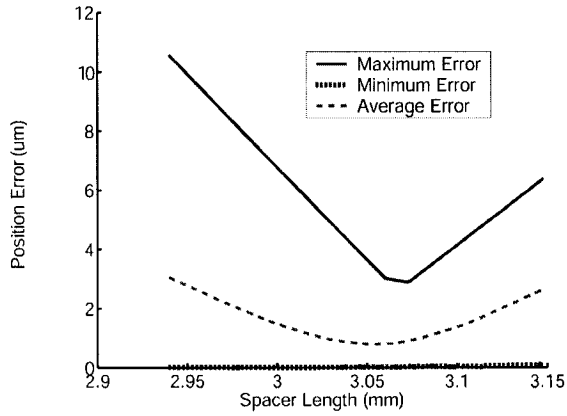

Fig. 17. Beam position error at the image plane vs longitudinal misalignment

4.2.4 Angular, lateral and longitudinal misalignment for the microlens array

Misalignment graphs for the microlens array were produced for angular and lateral misalignments of the microlens array with respect to the redirection module. No graphs were produced for the longitudinal misalignment because the lenses are deposited directly onto DOE2. The angular precision is controlled by the flatness of the diffractive and the microlens arrays substrates. The lateral precision is controlled by visual alignment of the two substrates with respect to each other. Hence, the lateral precision that was actually achieved is unknown (see Chapter 6 for more details.) In the case of the microlens array, the error is calculated at the image plane. Fig. 18 shows that the misalignment tolerance for ±4 μm of positional error (at the image plane) is ± 0.5°. The pitch misalignment tolerance is more severe because the array is wider than it is long. Fig. 19 shows that the misalignment tolerance for ±5 μm of positional error is ± 4 μm. In addition, there are no alignment features on the microlens array which will allow the positioning of the array within this tolerance. However, having a positional error at the

image plane of several microns does not impact the efficiency of the device, contrary to a misalignment at the DOE2 plane which induced clipping and thus loss and crosstalk.

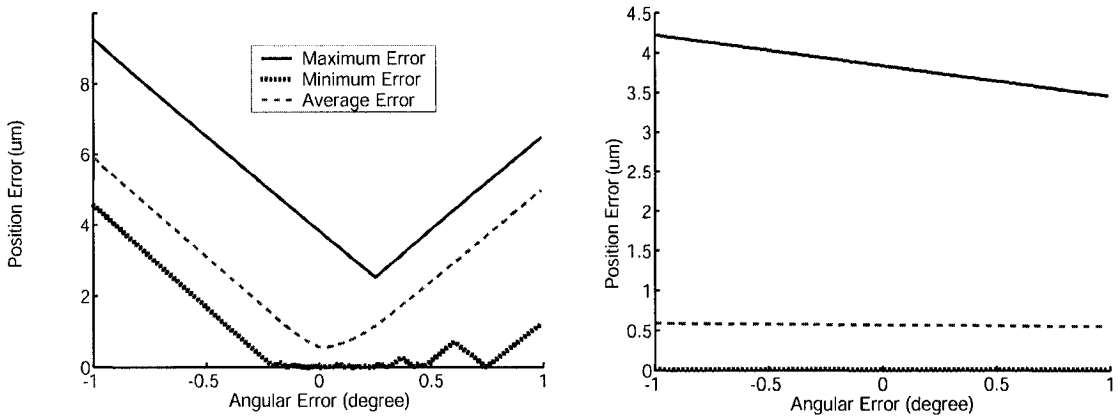

(a) (b)

Fig. 18. Beam position error at the image plane versus angular misalignment:
(a) error in y for pitch misalignment of the microlens array;
(b) error in y for yaw misalignment of the microlens array.

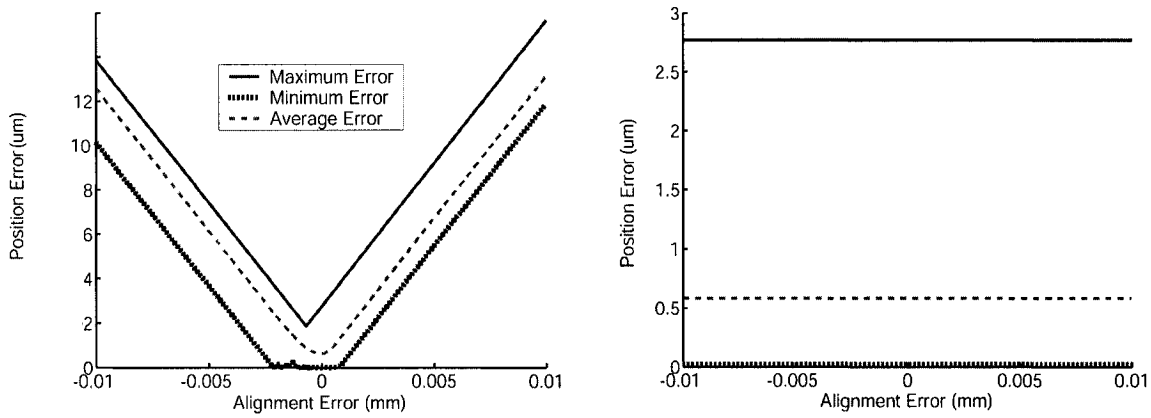

(a) (b)

Fig. 19. Beam position error at the image plane versus lateral misalignment:
(a) error in x for x misalignment of the microlens array;
(b) error in y for x misalignment of the microlens array.

4.2.5 Angular misalignment of the input beam to the redirection module

The input beam to the redirection module must, ideally, be perpendicular to the substrate. For testing purposes, it is controlled by the computer controlled rotational stage used to align the device with the testing equipment. Section 6.4 explains the technique used to actively align the device. The results shown in Fig. 20 indicate that the most sensitive alignment is the input beam with respect to the redirection module. A deviation of as little as 0.1° induces 10 μm of *average* misalignment at DOE2. This will cause clipping at the grating aperture which will decrease efficiency and induce unwanted diffraction effects. The effect of this misalignment is studied in the following section with the use of Gaussian beam propagation.

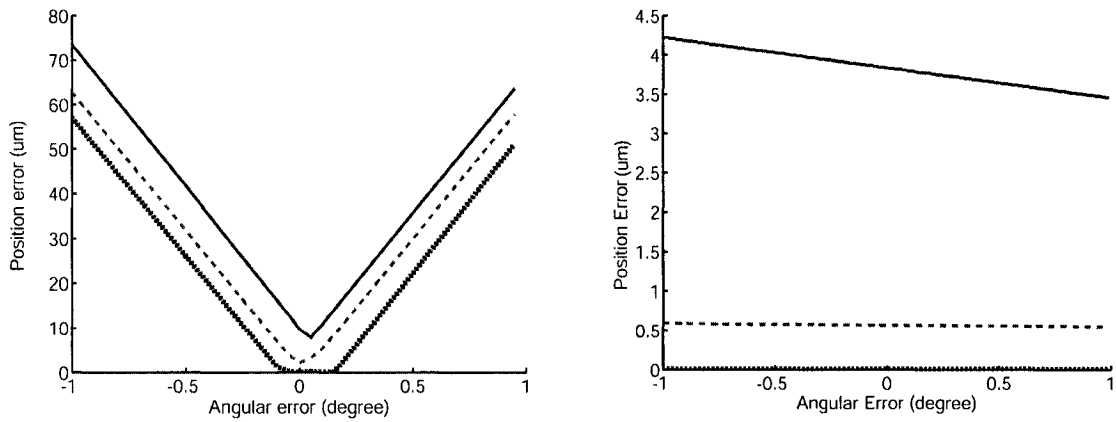

(a) (b)

Fig. 20. Beam position at DOE2 versus angular misalignment:
(a) error in x for yaw misalignment of redirection module;
(b) error in y for yaw misalignment of redirection module.

4.2.6 Summary of sensitivity analysis

Misalignment	Tolerance	Induced Beam Error
DOEs Angular	± 1°	±1 μm
DOEs Lateral	±5 μm	±2 μm
DOEs Longitudinal	±50 μm	±2 μm
Lens Lateral	±4 μm	±5 μm
Lens Angular	± 0.5°	±4 μm
Input Beam Angular	± 0.1°	±10 μm

Table 1. Summary of the sensitivity analysis

4.3 Beam propagation

Gaussian beam propagation is performed for all 64 wavelengths due to the variance in optical path length and to determine aperture clipping. The most sensitive misalignment (which was determined in the previous section) is the angular misalignment of the system with respect to the input beam. Therefore, Gaussian beam propagation was performed both for a perfectly aligned system and for a system whose angular misalignment (with respect to the input beam) is 0.1°.

For both an aligned and misaligned system (with respect to the input beam), the Gaussian beam expansion will be essentially the same. At DOE1, the average beam radius ($1/e^2$) is 20.8 μm with a minimum of 20.7 μm and a maximum of 20.8 μm. At DOE2, the average is 84.6 μm with a minimum of 82.3 μm and a maximum of 88.0 μm. To obtain 99% efficiency, the beam size needs to be 20.8 μm or less (at DOE1) and 83.3 μm or less at DOE2. Therefore, it is clear that beam clipping will occur even for a perfectly aligned system.

By performing beam propagation, it is possible to determine the amount of energy transferred through the apertures of the system, which, in this case, are the gratings. The analysis was performed for a perfectly aligned system and for a system where the input beam was misaligned by 0.1°. The average energy transferred through the grating apertures for a perfectly aligned system is 98.2% with a standard deviation of 0.2%. When the input beam to the system is misaligned by 0.1°, the energy transferred through

the grating apertures drops to 87.9% with a standard deviation of 1.5%. Fig. 21 and Fig. 22 show the energy transferred versus wavelength for an aligned and a misaligned system, respectively. Note that this neglects any reflection losses at the surfaces and assumes 100% diffraction efficiency (these factors will be dealt with in the following section).

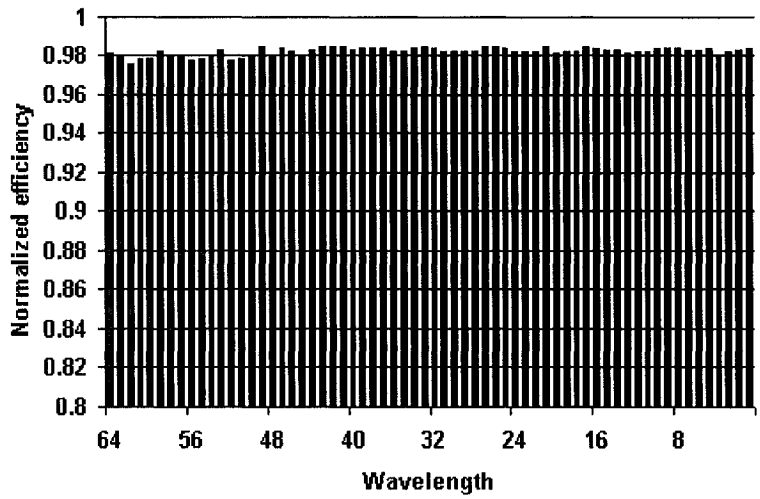

Fig. 21. Energy transferred through the apertures (perfectly aligned system)

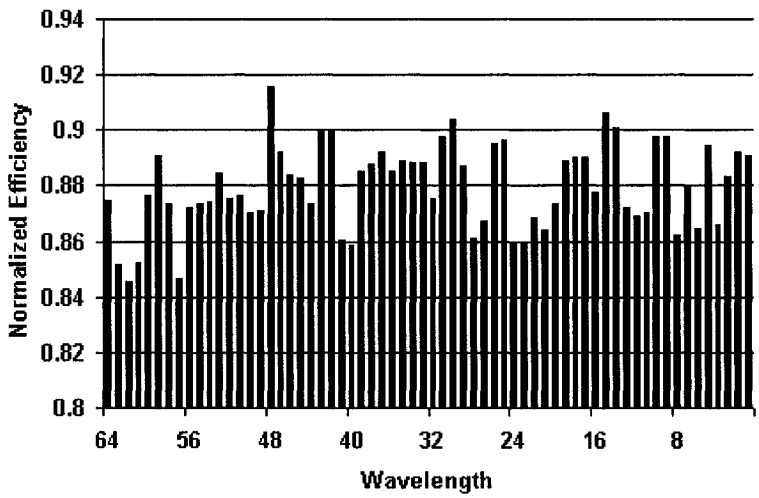

Fig. 22. Energy transferred through the apertures (0.1° system misalignment)

In addition, the Gaussian beam propagation showed that the clipped beams of the misaligned system are aberrated. Fig. 23 compares the intensity profile for a perfectly aligned system to a misaligned system. Note that for the perfectly aligned system, all the intensity profiles are identical whereas those of the misaligned system vary in shape and intensity. If the system were to be used with 64 output fibers or, as a multiplexer, with a single fiber, then more analysis would be needed to determine the coupling efficiency and hence, the total loss of the device.

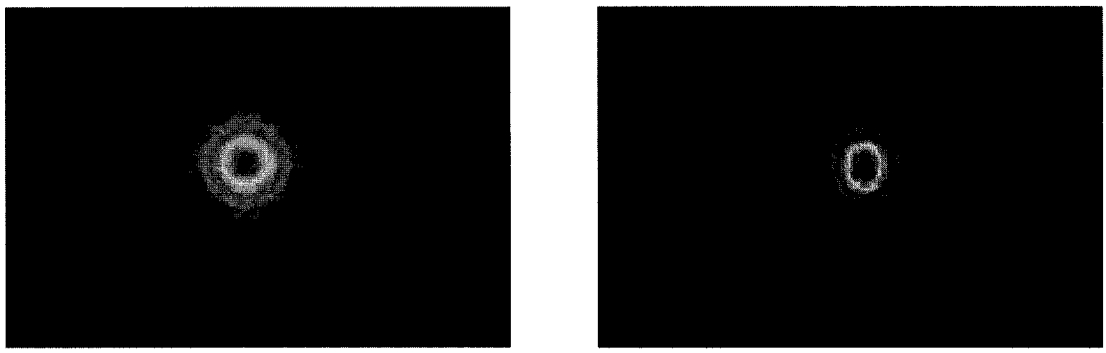

Fig. 23. Intensity profile for a perfectly aligned system (left) and a misaligned system (right)

4.4 Efficiency analysis

The scalar grating equation used in Chapter 3 to design the redirection module does not say anything about efficiency. As mentioned in that chapter, the smallest period (or highest deflection angle) used in the system was determined by the minimum feature size that can be etched. The largest period is given by $1/3^{rd}$ of the facet size so that at least three periods are illuminated by the beam (see Section 3.3.) Only scalar efficiency calculations of the gratings were performed (see Section 3.7) during the design of the module for lack of rigorous coupled wave analysis (RCWA) software. The scalar approximation is based on the following assumptions [2],[3]:

- Wavelet producing point sources are independent. There is no coupling between the electric and magnetic fields. Thus polarization of light is neglected.

- Lateral dimension L must be such that $L/\lambda >> 1$
- Grating period P must be such that $P/\lambda >> 1$
- Depth D of grating grooves must be such that $D/\lambda \approx 1$ (low aspect-ratio).
- Diffraction pattern must be observed a long distance away from the diffractive structure (far-field pattern) on the optical axis.

It is clear that several of these assumptions are not valid and thus scalar theory cannot accurately predict the efficiency performance of the gratings. Hence, once GSolver ©, a software which calculates diffraction efficiency rigorously, became available (which was after the device was fabricated), simulations were done to predict the diffraction efficiency of the gratings and the redirection module. The software uses the following assumptions to compute efficiency [4]:

- It assumes that an infinite number of periods are illuminated by a plane wave. There is no straightforward way to account for limited number of illuminated periods (in the redirection module, this can be as low as 3) or for Gaussian beam illumination.

The following subsections show the results of the efficiency analysis. Note that the efficiency results do not take into account beam clipping (for those beams and fabrication defects. However, the results do include the Fresnel losses due to the index mismatch between air and glass which could be reduced which can be reduced with the use of an antireflection coating.

4.4.1 Efficiency of a grating

Fig. 24 and Fig. 25 show the efficiency of a grating versus wavelength and period at normal incidence for P and S polarization, respectively. The etch depth of the grating is 2.64 μm (see Chapter 6) It is quite clear from the graphs that the gratings whose periods are between 6 and 10 will suffer from low efficiency and induce crosstalk and non-uniformity. P polarization has an average efficiency of 71.0% with a minimum of

62.2% and a maximum of 74.5%. S polarization has an average of 68.2% with a minimum of 72.9% and a maximum of 75.4%.

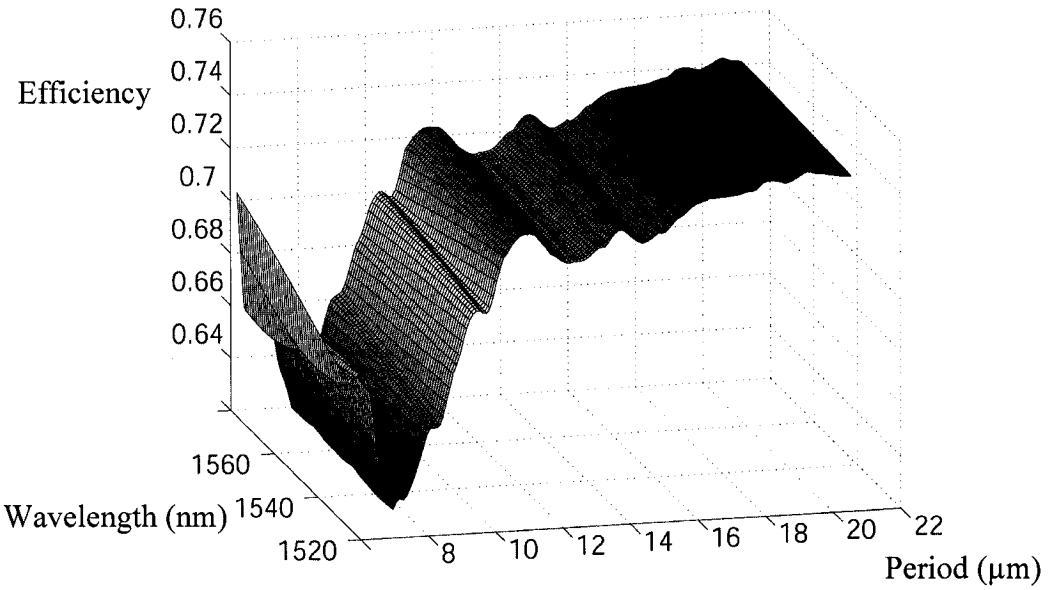

Fig. 24. Efficiency vs wavelength and period at normal incidence (P polarization)

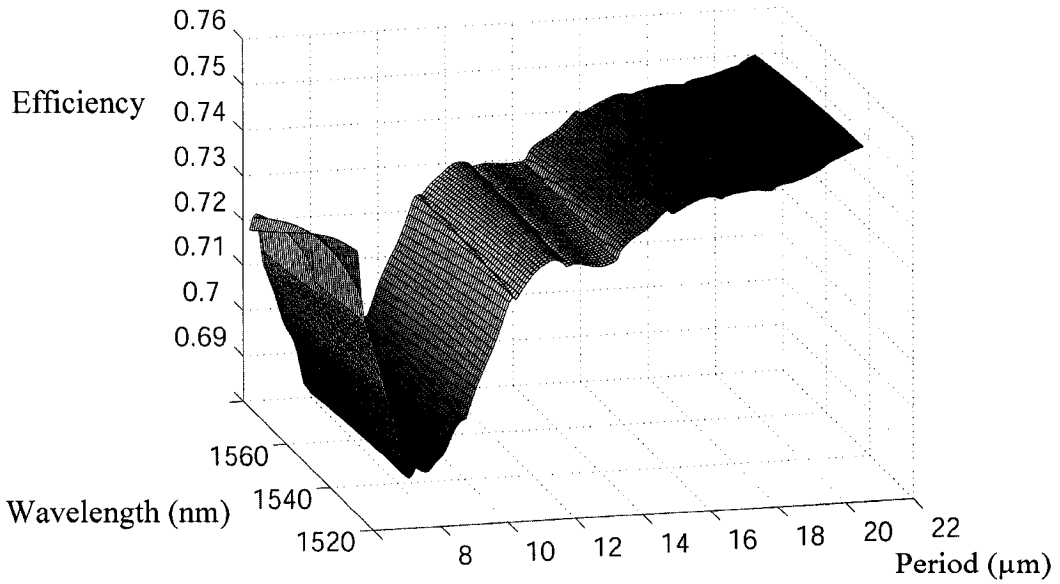

Fig. 25. Efficiency vs wavelength and period at normal incidence (S polarization)

4.4.2 Efficiency of the redirection module

Taking into account oblique incidence at the grating, the efficiency of the redirection module is shown, for all 64 wavelengths, in Fig. 26 and Fig. 27. The average efficiency for the P polarization is 44.8% with 5.0% standard deviation. For the S polarization, the average efficiency is 49.0% with a 2.9% standard deviation. The average efficiency could be improved by 5.9% using an antireflection coating.

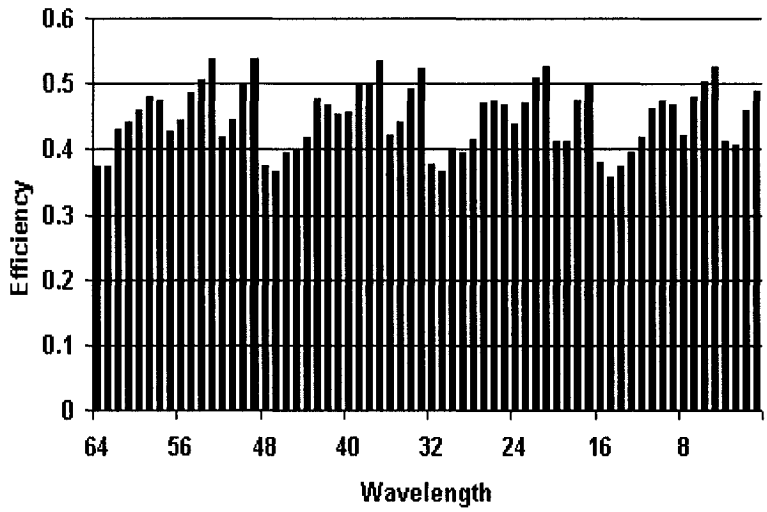

Fig. 26. Theoretical efficiency vs wavelength of the redirection module (p polarization)

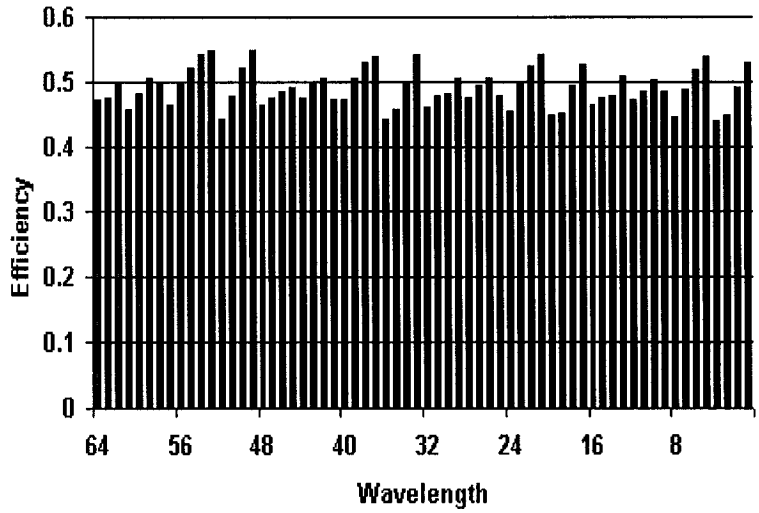

Fig. 27 Theoretical efficiency vs wavelength of the redirection module (s polarization)

4.5 Summary

This chapter presented simulations of the performance of the redirection module. These sensitivity analyses determined the specifications and tolerances for assembly and testing of the device. Those tolerances that deal with the assembly of the DOEs will be very easily met with current manufacturing techniques and interferometric alignment techniques (see Chapter 6.) However, the lateral misalignment of the microlens array, which is a very sensitive alignment, cannot be accurately predicted due to a lack of alignment features. Moreover, the alignment of the input beam to the redirection module is an extremely important alignment that will not be quantifiable beyond the tolerance listed in Section 6.4. In addition, Gaussian beam propagation and efficiency simulations were performed to get an idea of the performance of the device and to obtain a basis for comparison to the actual results presented in Chapter 7. The scalar efficiency calculations performed in Section 3.7 were not valid. Those results predicted an average efficiency of 66% where the RCWA predicts an average efficiency (averaged for s and polarizations) of 46.9%. In addition, the RCWA assumes perfect alignment. As shown in Section 4.3, an input beam misalignment of as little as 0.1° will cause additional loss through clipping and aberrations of the output beam.

4.6 References

[1] B.E. A. Saleh, M.C. Teich, Fundamentals of Photonics, Wiley & Sons Inc., New York (1991), Chapter 7.

[2] B. Kress and P. Meyrueis, Digital Diffractive Optics: An Introduction to Planar Diffractive Optics and Related Technology, John Wiley & Sons, (2000).

[3] H. P . Herzig, Micro-Optics: Elements, systems and applications, Taylor and Francis, (1997).

[4] www.gsolver.com

5. DESIGN, IMPLEMENTATION, AND CHARACTERIZATION OF A FREE-SPACE GRATING (DE)MULTIPLEXER

5.1 Introduction

The specifications given in Chapter 2 for the implementation of the 2D (de)multiplexer require the dispersion module to take an input fiber containing 64 wavelengths (1527.2 nm to 1577.8 on the ITU grid with 100 GHz spacing) and spatially separate them to the input (DOE1) of the redirection module. For simplicity, cost, and flexibility, the dispersion module was implemented using the free-space blazed grating approach used in the 1st order. This allows the use of low cost off the shelf lenses and gratings. However, as it will be shown in more detail in the design section, dispersion from a grating is non-linear (meaning that the spatial separation between wavelengths is not constant), therefore, the facet separation of DOE1 of the redirection module (see Appendix A) must follow the non-linearity of the dispersion module with the initial pitch between facets defined to be 62.5 μm. Finally, the beam waist at the DOE1 plane must be such that 99% of the energy is shining on the facet. Therefore, the beam waist must be 20.8 μm. Section 5.2 presents the design of the free-space grating (de)multiplexer. The implementation of the (de)multiplexer will be discussed in Section 5.3. Finally, testing results are presented in Section 5.4.

5.2 Design

The design of the dispersion module can be subdivided into three sections: the grating, the input lenses, and the output lens. A schematic of the design is shown in Fig. 28. The specifications of the design can be found in Appendix D.

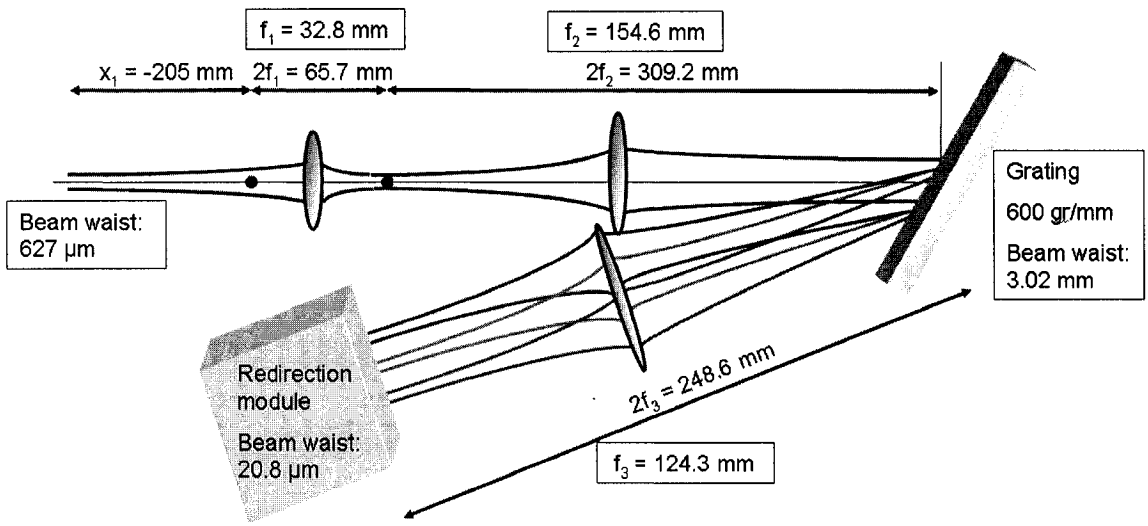

Fig. 28. Schematic of the dispersion module design

5.2.1 Grating

The blazed grating must be chosen such that it has high efficiency at the design wavelengths. A low cost solution is the aluminum coated ruled grating sold by Edmund Optics. The grating has 600 grooves per millimeter (larger numbers of grooves per millimeter provide higher angular dispersion, which will be discussed later) and a blaze angle of 28.41°. The efficiency of the grating at Litrow is 77%. This could be improved by the use of a gold coated grating.

Rayleigh's criterion states that the minimum resolvable wavelength difference is determined by the following relationship [1]:

$$(\Delta\lambda)_{min} = \lambda/mN \tag{8}$$

where m is the order and N is the number of grooves which are illuminated. Therefore, for a wavelength separation of 100 GHz or, approximately, 0.8 nm, used in the 1st order in

the 1550 nm wavelength band, the minimum number of grooves which must be illuminated is 1938 which translates into a beam diameter on the grating of 3.23 mm (1.62 mm beam waist.)

Considering the grating is used in the first order, there shouldn't be any problems of order overlap. The free-spectral range is defined as [1]:

$$(\Delta\lambda)_{fsr} = \lambda_o/m \tag{9}$$

where m is the order and λ_o is the center wavelength. Hence, in the 1st order, there is clearly no problem of overlapping orders.

The grating equation is defined as [1]:

$$m\lambda=d(\sin\alpha+\sin\beta) \tag{10}$$

where m is the diffraction order, λ is the wavelength of operation, α is the incidence angle (measured from the grating normal) and β is the diffracted angle measured from the grating normal. It is important to note that this equation is not linear and therefore, the angular separation between wavelengths is not constant. Consequently, the facets of the input of the redirection module are not on a constant pitch (the first one is 62.5 μm with the pitch increasing for all other facets.)

To maximize the angular dispersion, m should be maximized and d minimized. However, changing these values has a significant impact on efficiency. The grating used for the dispersion module is a low-cost reflection blazed grating. The grating is aluminum coated to enhance the reflection in the wavelength range of operation. Ideally, a gold coated grating should have been used but they are more expensive.

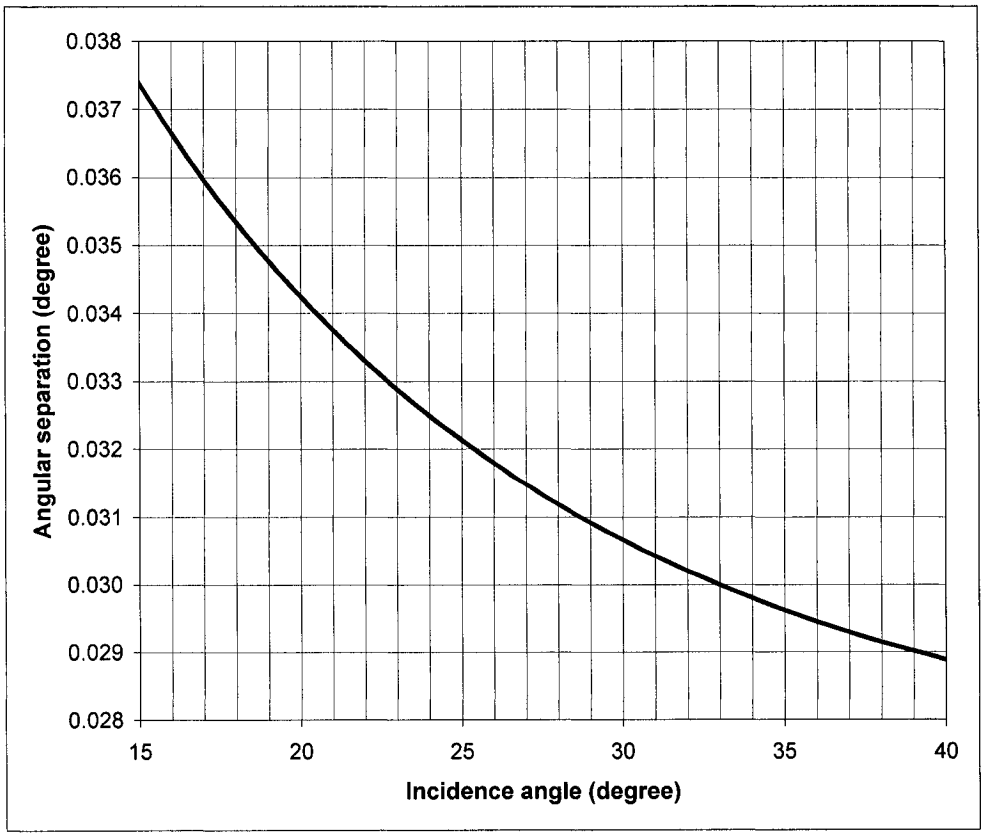

Fig. 29. Angular separation versus incidence angle on the grating at 1550 nm, $\Delta\lambda$=0.8nm

Maximum efficiency is achieved with the Littrow mount which is defined as having the incidence angle equal to the diffracted angle. For the chosen grating, the Littrow angle (for 1550 nm) is 27.80°. The angular separation between two wavelengths versus incidence angle is shown in Fig. 29. The system will not be used at Littrow for two very important reasons. First, the grating is used in reflection and the return path must be slightly different so that the light can be collected by the output lens. Second, as shown in Fig. 29, the angular separation between wavelengths can be tuned by changing the incidence angle of the grating. This will be used during implementation to fine tune the lateral separation of the wavelengths, which cannot be precisely predicted because the tolerances of the focal length of the lens used exceed the misalignment tolerance.

5.2.2 Output lens

The output lens design must satisfy two important constraints. First, it must illuminate the input facet (DOE1) of the demultiplexer with a 20.8 μm beam waist. Second, the channel separation between the first two wavelengths must be 62.5 μm. The coordinates of all other facets have been designed taking into account the non-linearity of the dispersion equation.

The lateral separation between two wavelengths which have been angularly dispersed is defined as:

$$p = f\tan\Delta\theta \tag{11}$$

where p is the lateral separation between wavelengths, f is the focal length and $\Delta\theta$ is the angular dispersion. A spreadsheet was written to determine the pitch between wavelengths depending on the departure from Littrow (α - 27.80°) and the focal length of the lens. For a lens with of focal length of approximately 124 mm (available at Melles Griots), the angular dispersion between wavelengths must be of 0.0289° which corresponds to an incident angle of approximately 32.8° (see Fig. 29.) To precisely obtain the necessary values for the pitch, the system will be implemented and the rotation of the grating will be tweaked until precisely the right pitch is measured at the output of the dispersion module. Hence it is unnecessary to find extremely precise values at this stage but rather a basis from which to work on in the implementation stage.

Having defined 124 mm as the focal length of the lens used, it is possible to work backwards and find the beam waist at the grating (whose diameter must 3.23 mm for enough resolving power.) The output lens is placed in a telecentric configuration and the output waist must be 20.8 μm for 99% power transfer. Hence, using the Gaussian beam relay equation [2]:

$$\omega_2 = f\lambda/\pi\omega_1 \tag{12}$$

is used to determine the beam waist size which must be illuminated on the grating. It is determined that the input lens must be designed to illuminate the grating with a beam that has a waist of 3.02 mm, which is more than sufficient to satisfy Rayleigh's criteria for the minimum resolvable wavelength difference.

5.2.3 Input lens

The input lenses must satisfy one constraint. It must transform the light emitted from the fiber to a 3.02 mm beam waist on the grating. It is important that the waist on the grating be of 3.02 mm so that the output lens will focus the light down to 20.8 μm at the output of the dispersion module so as to have 99% power transfer through the redirection module. For simplicity, a fiber collimator was used to collimate the diverging light emitted from the fiber. To produce the proper beam size on the grating, two lenses must be used (in addition to the collimator). The first lens has a focal length of 32.8 mm at 1550 nm (Melles Griots) and is placed ~17 mm from the collimator (and so the waist is 237.8 mm from the lens). The second lens has a focal length of 154.6 mm at 1550 nm and is placed ~188 mm from the first lens (about 0.5 mm more than the sum of the focal length of the two lenses.) Using Gaussian beam formulas for thin lens and the model for the collimator confirms the 3.02 mm waist on the grating.

5.3 Implementation

Fig. 30 shows the implemented dispersion module. A tunable laser is fiber coupled and input into the collimator. A series of two lenses collimates the beam onto the grating which diffracts the beam onto the output lens which focuses the beam for input into the redirection module. The device is implemented in several steps. First, the two input lenses are placed with the longitudinal separations given in Section 5.2.3. The laser is activated and a beam profiler is placed at the location where the grating is to be placed. The lens positions can be varied until a 3.02 mm waist is obtained. Next, the grating is glued to a rotational stage and the output lens is placed approximately one focal length

away from the grating. The laser is activated and the beam profiler is again used to optimize the beam waist size. Now, all the lenses are at the appropriate positions for the system to laterally separate the wavelengths by the pitch dictated by the design of the redirection module. The only remaining variable is the angular dispersion of the grating which is dependent on the incident angle of the beam. One of the functions of the beam profiler is to indicate the coordinate of the center of the beam on its detector. Hence, it can be used to evaluate the distance between two difference wavelengths. Therefore, the proper grating angle can be found by changing the grating angle and verifying the pitch between two wavelengths (by changing the wavelength of the tunable laser.)

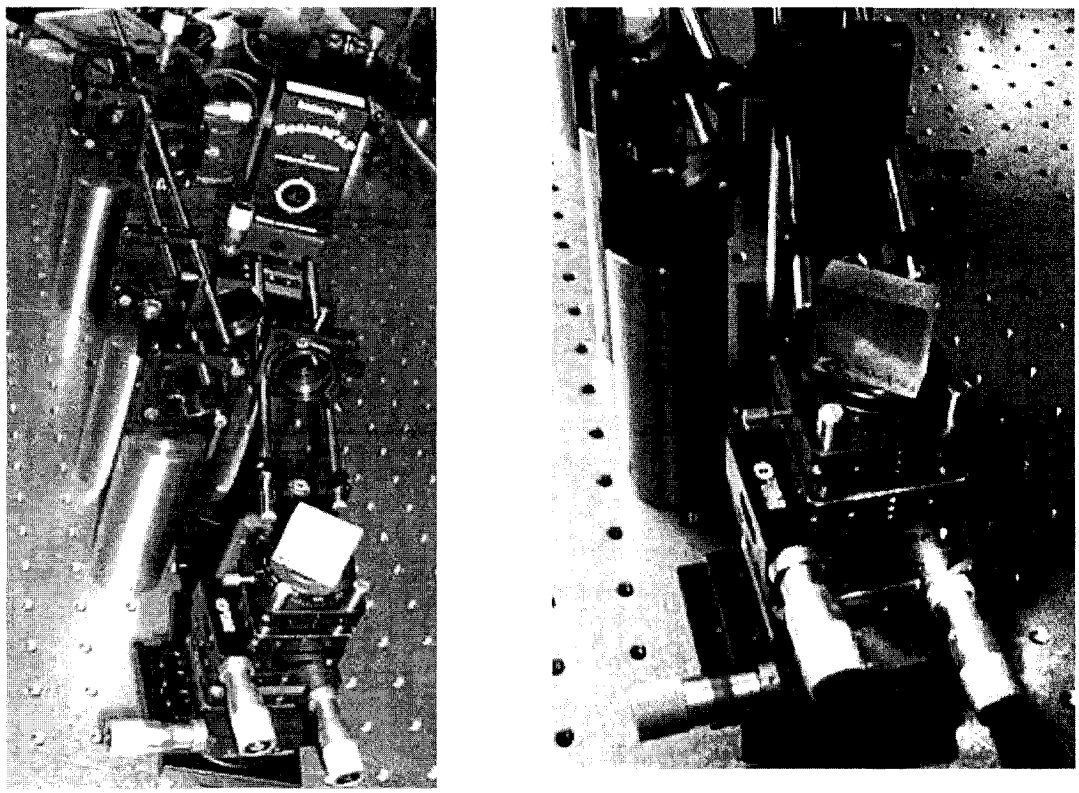

Fig. 30. Photograph of the implemented dispersion module

5.4 Testing

Tests were performed and logged after assembly to determine that the module performed to specifications. A summary of the results and specifications are shown in Table 2.

	Lateral spacing (μm)	Output waist (μm)	Loss (dB)
Specification	4084	20.8	N/A
Results	4088 ± 2	21.2 ± 0.5	1.93

Table 2. Summary of the system requirements and test results

5.4.1 Lateral channel spacing

The required lateral separation between the 1st and the 64th channel is 4084 μm. Using the beam profiler and the tunable laser, it was determined that the separation between the two 4088 μm with fluctuations in the reading of ± 2 μm. This translates to an average positional error on the facets of DOE1 of 0.06 μm per facet.

5.4.2 Output waist size

The input of the redirection module requires a 20.8 μm beam at the input for maximum power transfer. The output beam waist of the dispersion module was measured to be 21.2 μm with fluctuations in the readings of ± 0.5, which is slightly above the requirements.

5.4.3 Efficiency

The measured power losses of the system are due to Fresnel reflections on each of the six optical surfaces (~3%) and the diffraction efficiency of the grating (77%). The measured power losses, 1.93dB, were almost identical to the predicted loss of 1.94dB. This suggests that using the grating 5° off of the Littrow mount does not significantly decrease diffraction efficiency.

5.5 Summary

An overview of the design, implementation and characterization of a dispersion module was presented. The device was implemented to demonstrate the feasibility of incorporating a traditional wavelength (de)multiplexer to the redirection module for 2D wavelength (de)multiplexing. The implemented dispersion module satisfies the constraints of the redirection module while being implemented with off the shelf components without any custom alignment features and without using computation intensive optical design software. The lateral spacing between wavelengths is precise within 0.06 μm and the waist size is at most 0.9 μm (4.3%) larger than the design specifications. Finally, the loss of the device is 1.94dB.

5. References

[1] E. Hecht, Optics, 3rd edition, Addison Wesley Longman Inc., (1998), Chapter 10.

[2] B.E. A. Saleh, M.C. Teich, Fundamentals of Photonics, Wiley & Sons Inc., New York (1991), Chapter 7.

6. PACKAGING, FABRICATION, AND ASSEMBLY

6.1 Introduction

To produce the desired two-dimensional output array, it is important that the optical components be properly aligned. This chapter explains the optical component specifications as well as the optomechanical components used to assemble and test the module. Next, the fabrication process and vendor limits are detailed. Afterwards, the design of the alignment features is presented. After these two sections are presented, the CAD process that creates the masks used for lithographic fabrication of the redirection module substrates is given. Finally, the assembly of the device is presented.

6.2 Component specifications

The redirection module is implemented using four optical components: two fused silica substrates on which the diffractive features are etched, one fused silica spacer, and one fused silica microlens array. To assemble and test the system, two optomechanical components were fabricated. This section lists and justifies the specifications of these components.

6.2.1 Diffractive fused silica substrates

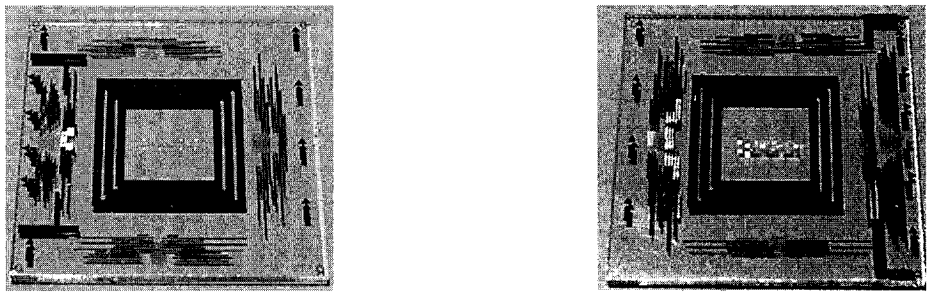

Fig. 31. Photograph of the fused silica substrates (DOE1: right; DOE2: left)

Two fused silica substrates, with the layout presented in Section 3.5, must be etched. The specifications of the substrate are shown in Table 3. The tolerance of the dimensions of the substrate is such that it cannot be diced smaller than 20.0 mm which assures that none of the features on the substrate are damaged. The thickness tolerance of the substrate is less than the ±50 μm tolerance for assembly listed in Chapter 4. In addition, any deviation from the 1.00 mm thickness can be compensated by the optical spacer. The parallelism and optical flatness of the substrate are more than enough to satisfy the angular tolerance of ±1° (see Chapter 4.) The fabricated substrates are shown in Fig. 31.

Material	Fused Silica (n = 1.444044 @ 1550 nm)
Dimensions	20.0 mm + 50 μm, - 0 μm
Thickness	1.00 mm ± 20 μm
Flatness	λ/4
Parallelism	5 arcsec (0.0014°)

Table 3. Specifications of the diffractive substrates

6.2.2 Fused silica spacer

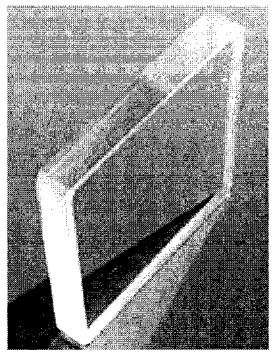

Fig. 32. Photograph of the fused silica optical spacer

An optical spacer made of fused silica is used to satisfy the longitudinal and angular constraints detailed in Chapter 4. The specifications are listed in Table 4. The dimensions are identical to the diffractive substrates. The thickness is such that that longitudinal constraint of 5.05 mm (in glass, 3.50 mm in air) is satisfied within the tolerance of ±50 μm. Note that several optical spacers were manufactured and the best one was chosen to compensate for deviations from 1.00 mm of the diffractive substrates. Again, the parallelism and optical flatness of the spacer is more than enough to satisfy the angular tolerance of ±1° (see Chapter 4.) The spacer is shown in Fig. 32.

Material	Fused Silica (n = 1.444044 @ 1550 nm)
Dimensions	20.0 mm + 50 μm, - 0 μm
Thickness	3.05 mm ± 20 μm
Flatness	λ/4
Parallelism	5 arcsec (0.0014°)

Table 4. Specifications of the optical spacer

6.2.3 Microlens array

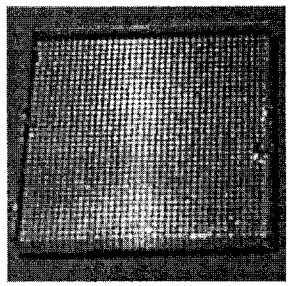

Fig. 33. Photograph of the fused silica microlens array

Table 5 lists the specifications of the microlens used to relay the diverging beam to the output (detector, MEMS, etc.) The tolerances on the dimensions and thickness of the microlens are unknown but irrelevant. The dimension of the microlens array is smaller than the diffractive substrates and this allows the use of the alignment features at the substrate edges (see layout in Section 3.5.) Had they been covered with microlenses, it would be impossible to align the perpendicularity of the redirection module with respect to the input beam. The tolerance on the lens pitch is lower than the alignment accuracy of the array (see Section 6.6) and therefore sufficient. The microlens array is shown in Fig. 33.

Material	Fused Silica (n = 1.444044 @ 1550 nm)
Dimensions	10.0 mm
Thickness	1 mm
Packing/Fill	Square/96%
Lens pitch	250 μm ± 0.25 μm
Focal length	776.1μm @ 550 nm

Table 5. Specifications of the microlens array

6.2.4 Redirection module holder

For testing purposes, it was required that a custom optomechanical part be designed to fasten the redirection module to computer controlled positioning stages. The holder (see Fig. 34) is designed to have a 3 mm ledge on which the redirection module is deposited. The ledge has been designed to be the same length as the spacer so that no mechanical stress would be induced on the substrates, which could result in misalignment when the redirection module is fastened to the holder. Four miniature set screws are used to secure the module to the holder by applying pressure to the spacer only (again to avoid inducing mechanical stress on the substrates.)

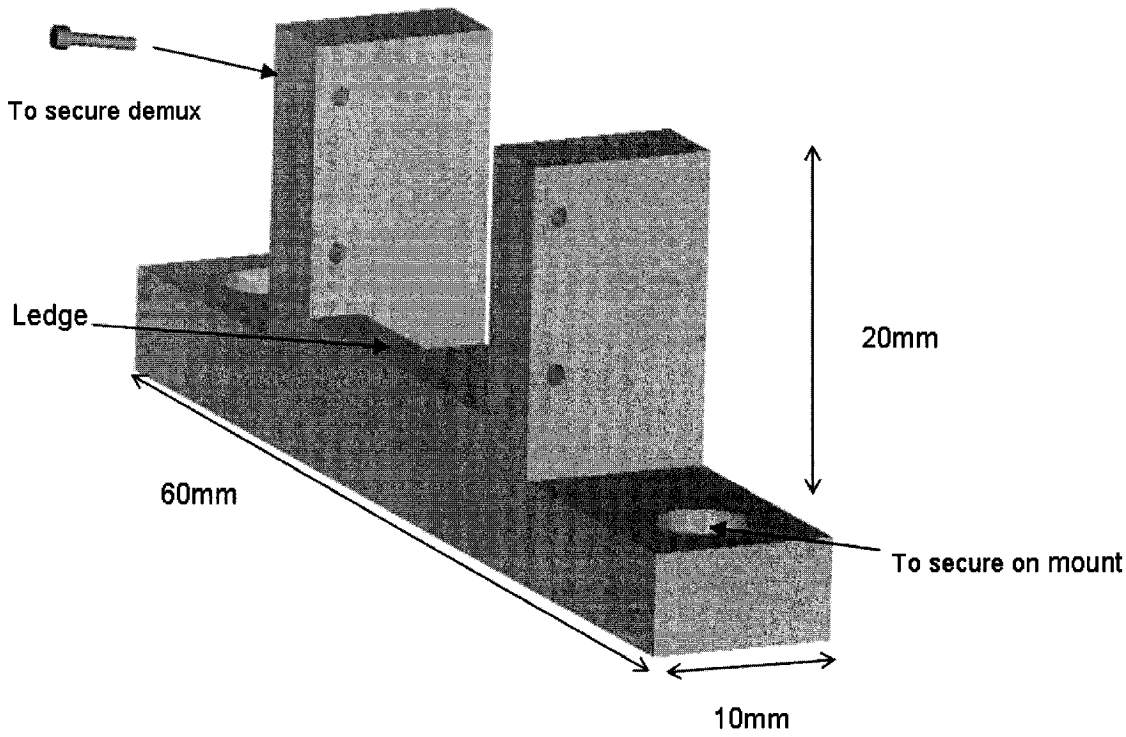

Fig. 34. Schematic of the redirection module holder

6.2.5 Vacuum chuck

To hold the substrates during assembly, a device is needed that can interface with computer controlled positioning equipment and the substrates while having a window through which the alignment features (discussed in Section 6.4) of the substrates can be seen with a CCD. In addition, the device must tolerate angular misalignments. To satisfy these requirements, a vacuum chuck (see Fig. 35) is designed to hold the substrates using suction cups which are connected to a vacuum pump. When the substrate is pressed onto the optical spacer, the flexible rubber of the suction cups compensates for any angular misalignment between the spacer and the vacuum chuck. Hence only lateral and rotational misalignments need to be adjusted.

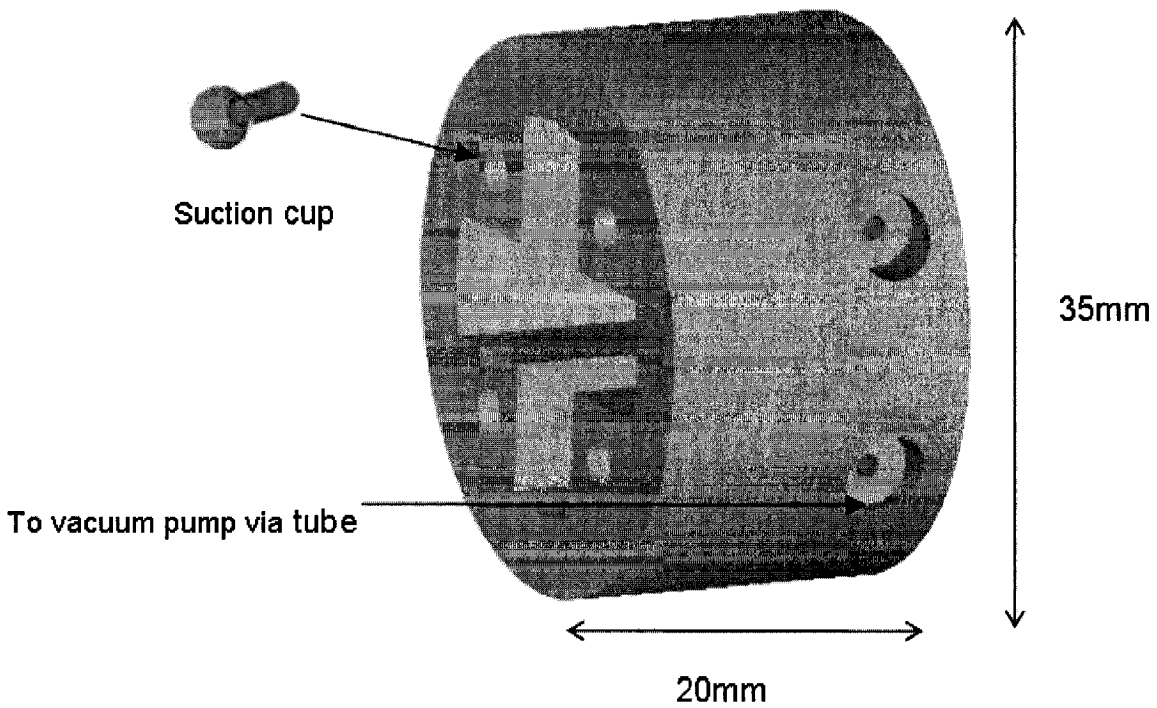

Fig. 35. Schematic of the vacuum chuck

6.3 Fabrication process and vendor limitations

The fabrication process and vendor limitations of this process dictated many of the constraints of the design (see Section 3.3) and of the CAD mask generation script (see Section 6.5) To fabricate the DOEs, binary chromium masks are prepared using electron-beam lithography and the features are etched into the substrates using reactive ion etching (RIE) [1]. Fig. 36 illustrates this. To produce DOEs with more than 2 phase levels, additional chromium masks are needed at the rate of 2^n phase levels where n is the number of masks. The minimum feature size that can be etched using the vendor specific process is 1.5 μm with a grid resolution of 0.1 μm. The impacts of these limitations on the design are explained in Section 3.3. Essentially, the minimum period dictates the maximum deflection angle of the beam and thus the minimum length of the redirection module. In this case, 4 levels (see Section 3.3) are used in the design. This imposes a minimum DOE grating period of 6 μm. The grid resolution quantizes the DOE grating period and consequently the deflection angle which induces positional error at the output.

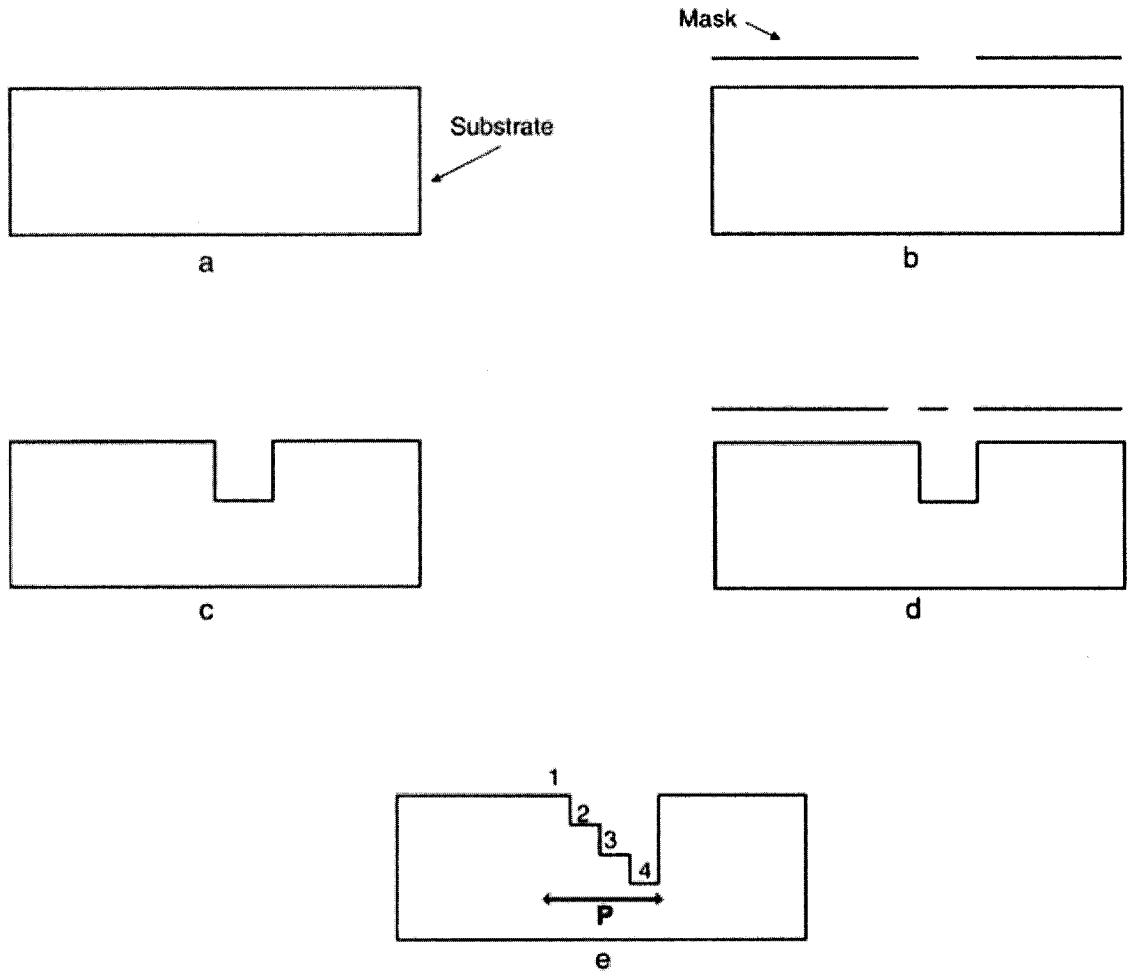

Fig. 36. Conventional lithographic etching steps for DOE production

The DOEs are fabricated using four masks. Two masks are used to produce the 4 level DOEs that are used to redirect the light to a 2D output array. One mask is used to etch the alignment features and the 4th mask is used for metal deposition. The etching steps are detailed below (the letters in brackets refer to Fig. 36 and the equations are taken from [1]). Note that the DOEs have a 25% duty cycle, which means that the "steps" of the quantized prism are of equal width.

1. Starting from a clean substrate (a), the first mask is used (b) to etch the equivalent of two level depths, at the position of levels 3 and 4 (c). The etch depth is given by the following equation:

$$h(\pi) = \lambda_{1.55}/2(n_{glass} - n_{air}) = 1.76\ \mu m \quad (13)$$

2. Then, the second mask is used to etch another level depth at the position of level 2 and 4, creating the four levels structure with the desired period (shown in red). In this case, the etch is equal to:

$$h(\pi/2) = \lambda_{1.55}/4(n_{glass} - n_{air}) = 0.88\ \mu m \quad (14)$$

3. Using the same method described in Fig. 36, the alignment features are etched into the substrate. The etch depth is given by equation (15) below and notice that the wavelength of operation has changed to 852 nm (see Section 6.4 for details of the design of the alignment features.)

$$h(\pi) = \lambda_{0.852}/2(n_{glass} - n_{air}) = 0.97\ \mu m \quad (15)$$

4. Finally, aluminum is deposited with a thickness of 10 μm (vendor specification.) This metal is used as glue barriers (see Section 3.5) and alignment features.

For the 4 level DOEs used to redirect the light, the total etch depth is 2.64 μm. Note that the etch depth is dependent on wavelength and that the depth was defined using the center wavelength of the band to be (de)multiplexed. Hence, this etch depth could be optimized for each facet (wavelength) to increase efficiency. This and other techniques to optimize the etch depth are detailed in Chapter 8.

6.4 Alignment features

The interferometric lenses (ILs), shown in Fig. 37, are used to laterally and rotationally (with the use of two IL pairs) align the substrates with respect to one another. When a plane wave is illuminating the first interferometric lens, approximately half of the power is focused and half the power remains collimated because the lenses are used at 632 nm and etched for 852 nm (hence they are purposefully inefficient.) If the focal length of the lens is designed such that it is half the length of the module, the two beams will recombine to form an interference pattern at the output if the two substrates are

misaligned. If the substrates are aligned, then no fringes will appear. See [2] for more information. The precision of the technique is a function of the size of the interferometric lens and the distance between the substrates:

$$\Delta x = f_A \tan[\sin^{-1}(N\lambda/D_L)] = 1.47\ \mu m \tag{16}$$

where Δx is the precision, f_A is the focal length (half the distance between the two substrates, 1.75 mm), N is the number of fringes (1 fringe), λ is the wavelength of operation (632 nm) and D_L is the size of the interferometric lens (750 μm.)

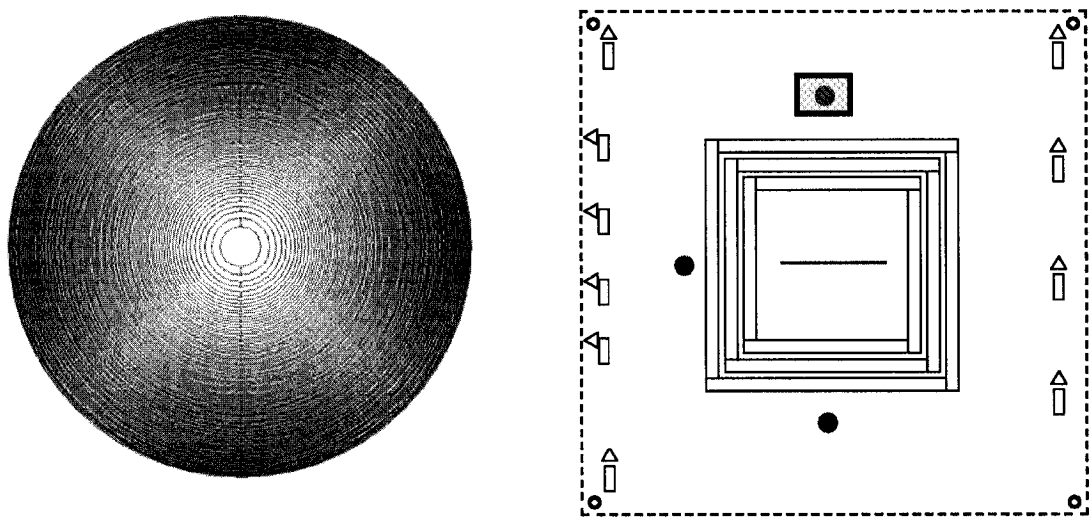

Fig. 37. Layout of a substrate (right) and the layout of an interferometric lens (left)

The center ring of the diffractive lens has a radius of approximately 33 μm. By centering the (focused) input beam to the redirection module through the center of a pair of ILs, the perpendicularity of the redirection module with respect to the input beam can be adjusted within:

$$\Delta\theta = \tan^{-1}(r/d) = 0.54^\circ \tag{17}$$

where r is the radius of the center ring of the IL and d is the distance between the two lenses. Simulations shown in Chapter 4 demonstrate that ±0.1° misalignment causes ±10 μm positional error at the output of the redirection module. Hence it is clear that this

technique is not sufficient to insure proper alignment of the device. This will cause losses and aberrations of the output beams. However, it will provide enough precision to demonstrate the wavelength mapping operation.

6.5 Mask generation

A script was written to generate a drawing of the masks required for the fabrication of the diffractive optical elements needed for the redirection module. The masks were generated in AutoCAD ® from data that was optimized in MatLab ® (see design in Chapter 3.) The input data to the script is as follows for each of the 128 facets:

- The period in x,
- The period in y,
- The net period,
- The facet sizes (calculated from data for x),
- The facet positions,
- And the offsets between the DOEs (only one value is needed)

It is defined that having a negative period is the same as operating the grating in the -1 order. Hence, the blaze angle is inverted for those gratings whose period is negative. The facet size of DOE1 in x is calculated by the script from the facet positions. All other facet sizes are hard coded in the script. The offset between the DOEs is controlled by the user when entering the starting coordinates for DOE1 and DOE2. Details of the offset are given in Chapter 3. In addition, the DOEs are 4 level structures and thus the script had to write the masks on different layers so that they could easily be converted to a GDSII file, which is the format required by the vendor. Fig. 38 shows an example of the two masks necessary to fabricate four facets with four level gratings. The masks generated by the script are composed of two layers. The surface inside the polygons of the first layer (shown in Fig. 38 (top)) is etched to a depth of π to produce the pattern shown in Fig. 36 (c). Then the second mask is used to etch $\pi/2$ to give the result shown in Fig. 36 (e). Polygons are drawn where the substrate needs to be etched and

their coordinates snap on 0.1 μm grid. Also note that it is the corners of the facets that snaps on 0.1 μm grid and not the centers. The distance between facets as well as the periods of the gratings are shown in Appendix B.

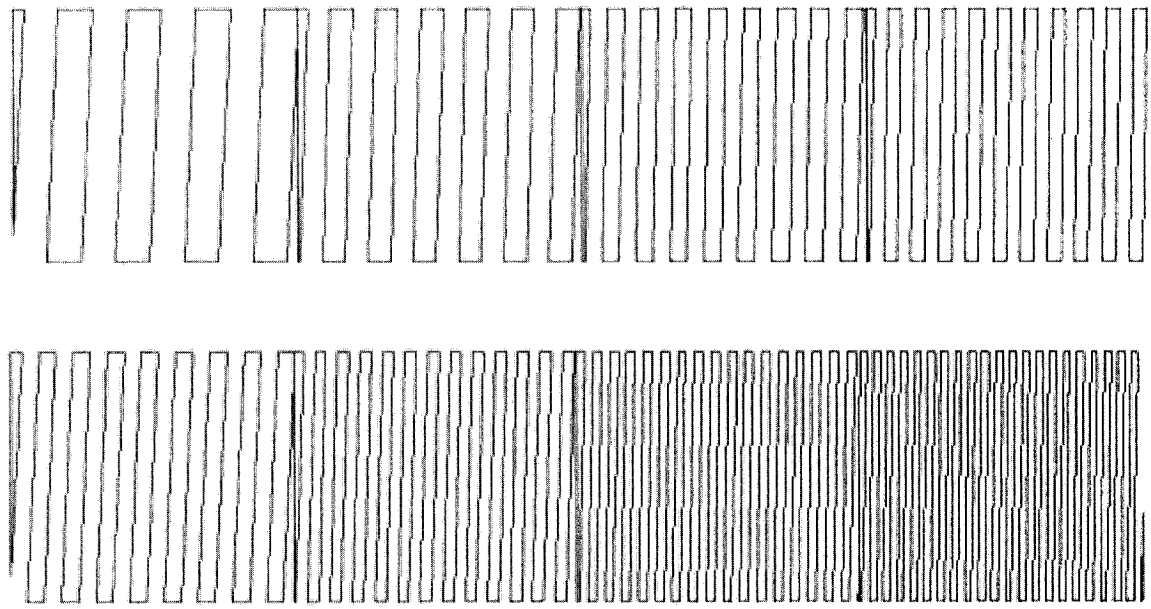

Fig. 38. Mask 1 (top); Mask 2 (bottom)

6.6 Assembly procedure and assembly

This section explains and illustrates the step-by-step assembly of the redirection module as well as the optical setup used for assembly.

The first step consists of gluing any one substrate to the optical spacer as shown in Fig. 39. The alignment is done visually so that the edges of the substrate and spacer coincide. Also, the spacer and the substrate must be firmly pressed together to insure parallelism. A UV-curing epoxy (Norland index matching optical adhesive NOA 61) is used to cement them together. The curing is done in two steps: first a rapid (5 minute) pre-cure is done to allow it to be moved without upsetting the alignment. Next, a long

(20-30 minute) cure is done to obtain full cross linking and solvent resistance of the adhesive.

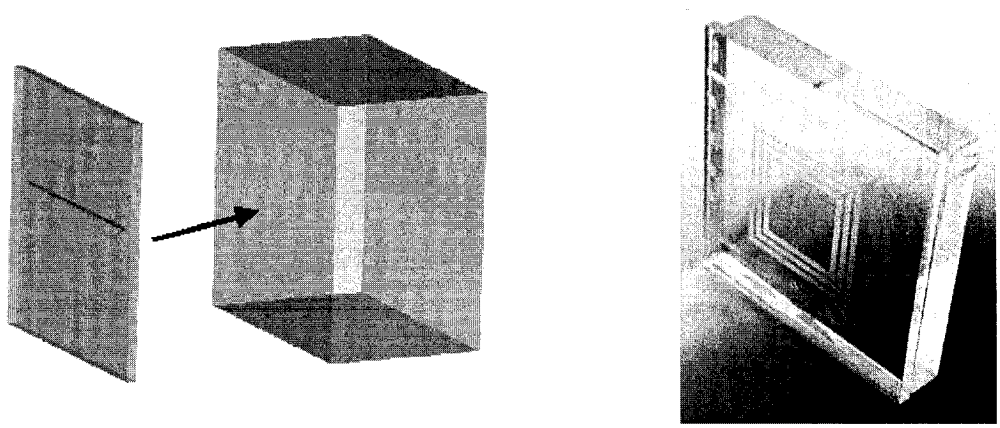

Fig. 39. Illustration (left) and photograph (right) of the first assembly step

Next, the optical spacer with the cemented substrate is placed on the redirection module holder and secured using four set screws as shown in Fig. 40.

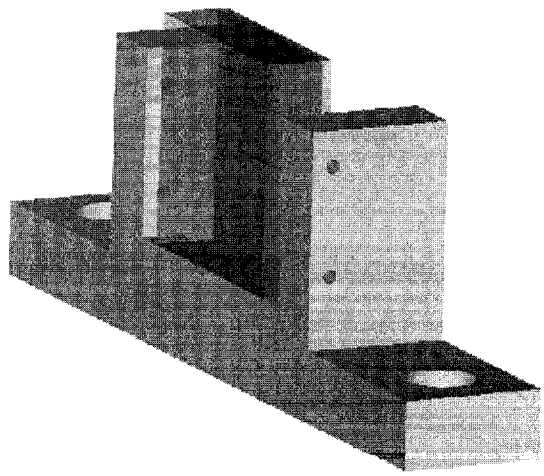

Fig. 40. Illustration of the second assembly step

Before completing the third step of assembling the second substrate (DOE), an optical setup must be constructed to operate the ILs (see Section 6.4) that will allow us to align the substrates. To operate, the IL technique needs a plane wave that is perpendicular to the substrate. To insure this, a retroreflection beam alignment technique [3] is used and a schematic of the experimental setup is shown in Fig. 41. The precision of this technique is given by [3]:

$$=0.5\tan^{-1}(\varepsilon/f_c) \tag{18}$$

where β is the angular misalignment, ε is the diameter of the pinhole and f_c is the focal length of the collimating lens. In this case, the pinhole diameter was 100 μm and the focal length of the collimating lens was 500 mm. Therefore, the perpendicularity of the plane wave will be within 0.005°. The error induced by the IL technique due to this misalignment is given by [2]:

$$\Delta x = 2f\tan\beta \tag{19}$$

where Δx is the error, f is the focal length of the IL and β is the plane wave beam misalignment from perpendicularity. Hence, with the plane wave misalignment of 0.005° calculated above, the induced error for a focal length of 1.75 mm (see Section 6.4) is 0.3 μm. This value is much less than the precision of 1.47 μm calculated for the ILs in Section 6.4. Hence, the plane wave perpendicularity is essentially perfect.

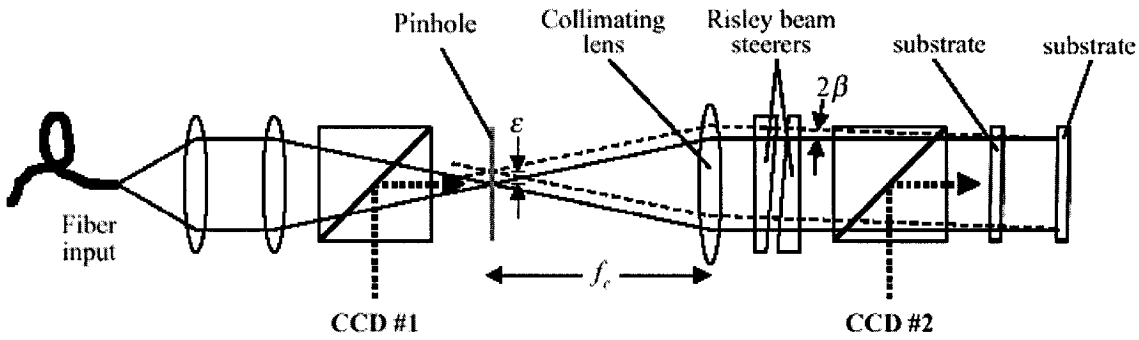

Fig. 41. Experimental setup that uses the retroreflection beam alignment [3] technique

After the experimental setup is constructed with the specifications explained earlier and the shown in Fig. 41, the third step is to position the redirection module holder and the optical components into the experimental setup and adjust the perpendicularity of the beam using the risley prisms. Once the beam is perpendicular, the second substrate is deposited onto the optical spacer (with a drop of UV epoxy in between) using the vacuum chuck which allows lateral, rotational and tilt alignment of the 2nd substrate with respect to the one which has already been cemented. Fig. 42 shows the ILs before and after alignment of the substrate. Once the substrate is aligned, the glue is cured and the result is shown in Fig. 43.

Fig. 42. Photograph of the IL when the substrate is misaligned (left) and aligned (right)

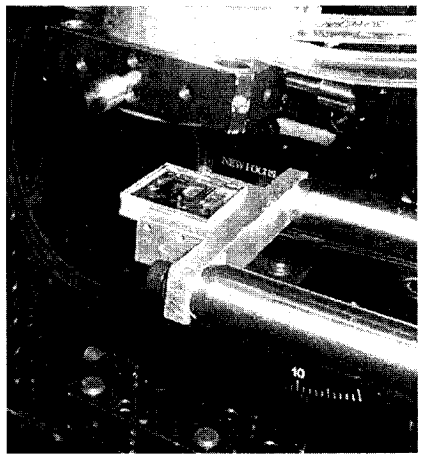

Fig. 43. Photograph of the redirection module after completing the third assembly step

The fourth step involves aligning the microlenses to substrate 2 (DOE2) of the redirection module. Low cost stock microlenses were used and therefore no alignment features are present to ensure high accuracy (i.e. > 2 μm) alignment. Unfortunately, as shown in Chapter 4, the microlens array misalignment has a strong effect on the positional output of the beams. Nevertheless, the lens array was visually aligned and glued to within ~5-10 μm. Despite the use of metal barriers, glue infiltrated itself into 9 facets of the DOEs rendering them useless. Fig. 44 shows the microlens array before and after alignment. Fig. 45 shows the assembled redirection module.

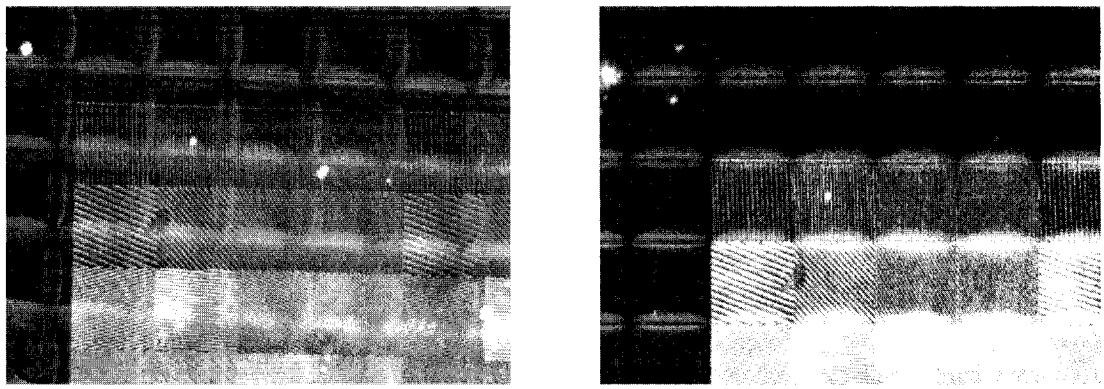

Fig. 44. Photograph of the lens array when it is misaligned (left) and aligned (right)

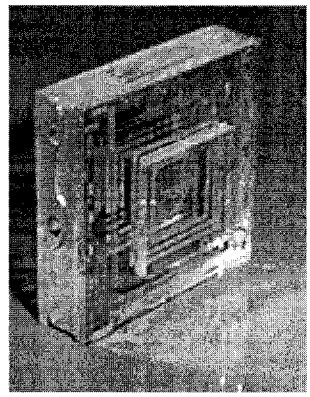

Fig. 45. Photograph of the assembled redirection module

6.7 Summary

This chapter presented the packaging, fabrication, and assembly of the redirection module. The procedure might seem lengthy and complicated but once the masks are created, it easy to reproduce multiple copies of the substrates. In addition, as detailed in Chapter XX, the redirection module could be reproduced by plastic injection molding.

6.8 References

[1] B. Kress and P. Meyrueis, Digital Diffractive Optics: An Introduction to Planar Diffractive Optics and Related Technology, John Wiley & Sons, (2000).

[2] B. Robertson, Y. Liu, G.C. Boisset, M.R. Tagizadeh, and D.V. Plant, "In situ interferometric alignment systems for the assembly of microchannel relay systems.", Appl. Opt. 36, pp9253-9260 (1997).

[3] M.H. Ayliffe, M. Chateauneuf, D.R. Rolston, A.G. Kirk, D.V. Plant, "Six-degrees-of-freedom alignment of two-dimensional array components by use of off-axis linear Fresnel zone plates.", Appl. Opt. 40, p. 6515 (2001).

7. EXPERIMENTAL RESULTS

7.1 Introduction

This chapter presents the performance results of the redirection module. First, scanning electron microscope scans of the fabricated substrates are shown and discussed. Next, the experimental test setup and test procedure is explained. Then, the grating efficiency of DOE1 and DOE2 are presented. Section 7.5 presents the efficiency and uniformity results. Section 7.6 shows the spatial power scan of facet 64. The chapter ends with a short summary of the results.

7.2 Scanning electron microscope scans

Scanning electron microscope (SEM) images (see Fig. 46) of the DOE facets were obtained to qualitatively evaluate the fabrication quality and efficiency of the gratings. It was observed with these scans that mask misalignment did occur during fabrication causing the duty cycle of the gratings to be non-ideal (i.e. not 25%). This also caused over-etching or under-etching leading to sudden valleys or mountain in the grating profile. All these defects reduce the efficiency of the DOEs.

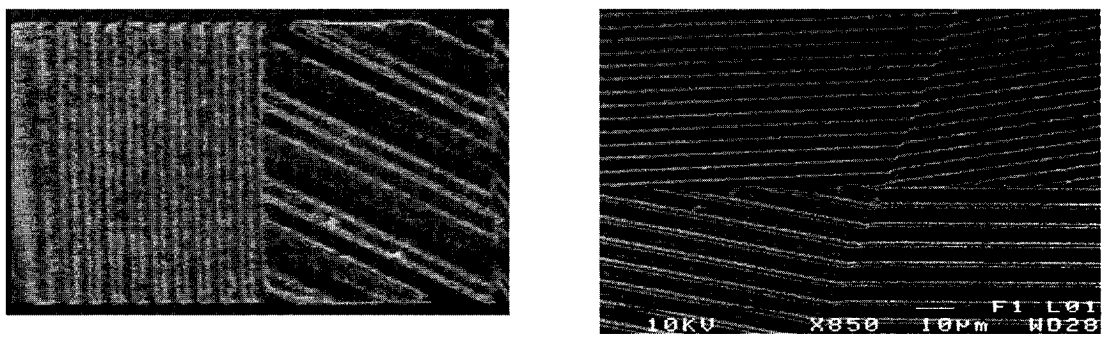

Fig. 46. SEM scans of DOE1 (left) and DOE2 (right)

7.3 Experimental test setup and procedure

There are three test setups used to characterize the redirection module. The first setup, shown in Fig. 47, is used to test the efficiency and uniformity of the individual gratings. The second setup, shown in Fig. 48, is used to measure the efficiency of the redirection module. The third setup, shown in Fig. 49, is used to measure the efficiency and crosstalk of the redirection module. All experimental setups are essentially the same. They all employ the same tuneable laser, collimating lenses, and motorized translation and rotation stages. The light from the tuneable laser is focused to a waist of 20.8 μm by the collimating lenses. A beam profiler was used to determine that the input was ~20.8 μm. A detailed schematic of the collimating system can be found in Appendix C. However, to characterize the efficiency of the gratings and the redirection module, a focusing lens is needed to project the beam onto the power wand. For these tests, no spatial scans are performed. The efficiency is measured by shining the diffracted spot onto the detector of the power wand. In the case of the redirection module, a 500 μm pinhole (mounted on a XYZ stage) is used to isolate the specific facet under test. To perform the spatial power scan, a 4f optical system is needed to image the output of the redirection module onto the power wand. In addition, the power wand is covered by a 5 μm pinhole which allows spatial scans of the output to be performed.

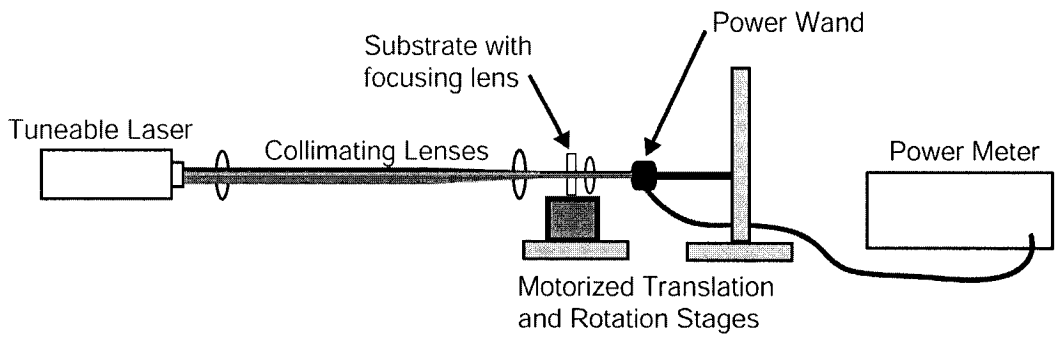

Fig. 47. Test setup to characterize the gratings

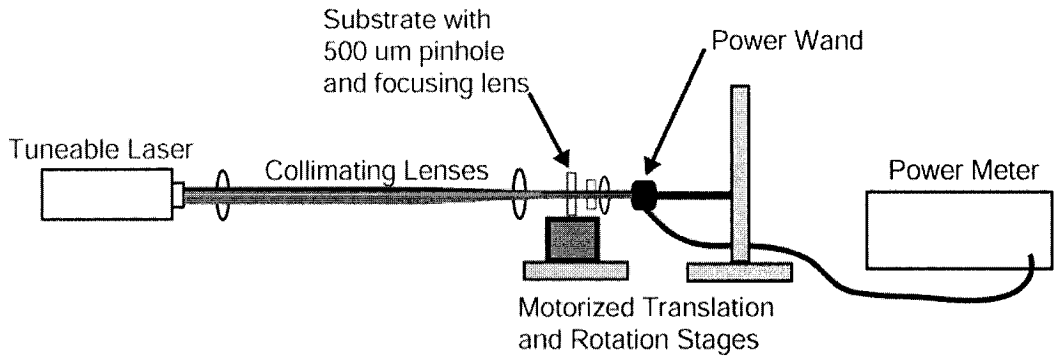

Fig. 48. Test setup to characterize the redirection module

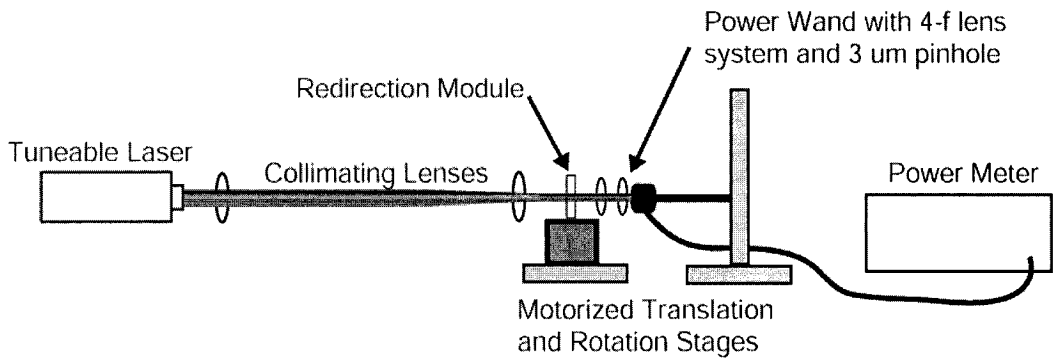

Fig. 49. Test setup to perform a spatial power scan

The test setups for the redirection module also need an extra alignment step. Once the test setups have been implemented, the redirection module must be aligned to be perpendicular to the input beam so as to satisfy the constraint discussed in Section 4.2.5. This alignment is performed by using the center ring of the interferometric lenses on the two substrates. When the laser light hits the center of the rings, the misalignment was calculated (in Section 6.4) to be 0.54°. Afterwards, the beam is aligned with the first facet of DOE1. At this point, it is possible to qualitatively verify that the device successfully performs the redirection operation. A collage of 16 different redirected wavelengths (at DOE2) is shown in Fig. 50.

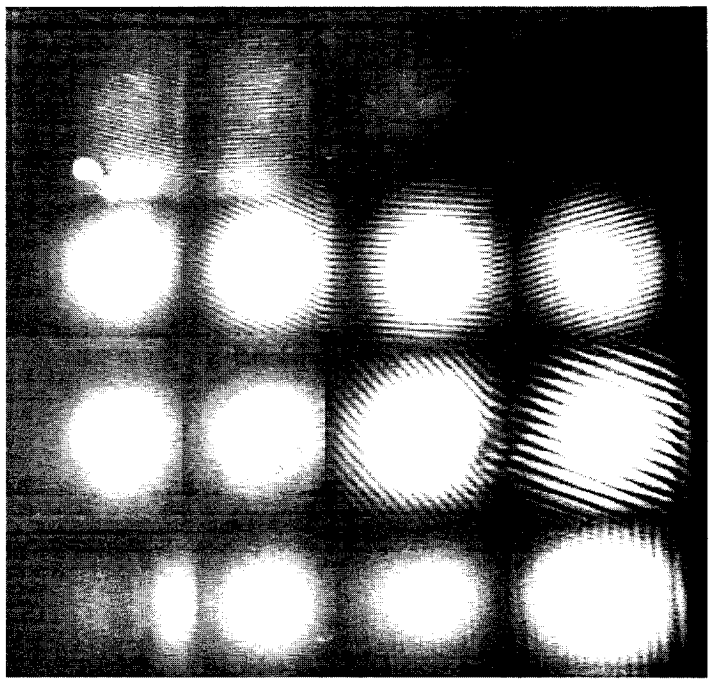

Fig. 50. Collage of the 16 redirected beams at DOE2

7.4 Efficiency and uniformity of the gratings

This section contains three separate analyses of the results of the grating efficiency measurements. Fig. 51 and Fig. 52 show the efficiency of all 64 facets of DOE1 and DOE2, respectively. Fig. 53 and Fig. 54 plot the results with respect to the grating period. Those graphs also contain the theoretical grating efficiency curve for comparison purposes. Finally, Fig. 55 and Fig. 56 demonstrate the polarization dependent loss (PDL) of 16 facets of DOE1 and DOE2, respectively.

The average efficiency of the gratings of DOE1 (which have identical periods to those of DOE2 only with a smaller facet size), is 25.2% with a standard deviation of 7.6%. The maximum efficiency is 40.7% while the minimum is 8.6%. For DOE2, the average efficiency is 41.6% with a standard deviation of 9.8%. The maximum efficiency is 60.7% while the minimum is 19.7%. Considering that the periods of both DOEs are identical, the performance results should have been similar. There are several reasons

that can explain the discrepancy. Firstly, DOE1 has fewer periods (due to its smaller size) than DOE2 which could potentially lead to lower efficiency. Second, potential fabrication defects will have a bigger impact on efficiency for DOE1 because it has fewer features. Finally, it is possible that the fabrication process was not completely uniform and that one substrate was more poorly fabricated.

It can be seen from Fig. 53 and Fig. 54 that the data points follow the trend of the theoretical analysis. As mentioned in Chapter 8, to increase the efficiency and uniformity of the device, only grating periods above 11 μm should be used.

The average PDL of the gratings of DOE1 have been measured to be 7.6% with a standard deviation of 2.5%. For DOE2, the average PDL is 7.2% with a standard deviation of 2.3%. This is less than a dB of average PDL for DOE1 and DOE2. However, when the PDL is combined, the sum is ~1.5dB of PDL, which is quite significant. Considering that all facets have different grating orientations, there is no simple way to mitigate the PDL. However, due to the different facet orientations, the probabilities are that the actual PDL will be lower than the value stated above, which consists of the average of the maximum PDL which can occur for each grating.

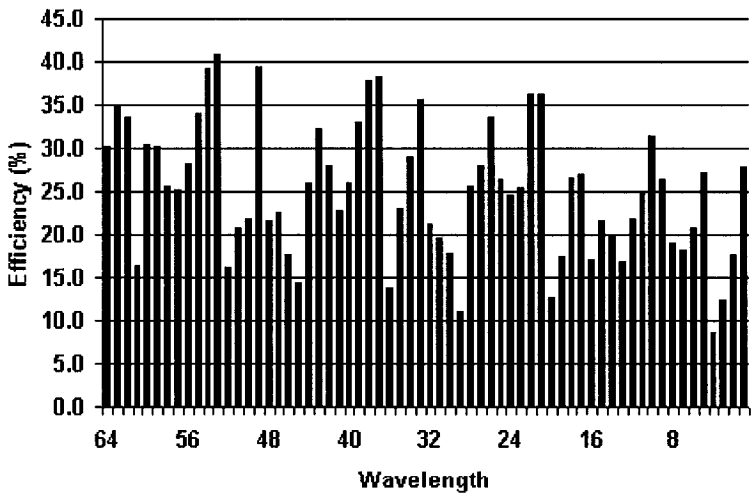

Fig. 51. Measured efficiency for all 64 facets of DOE1

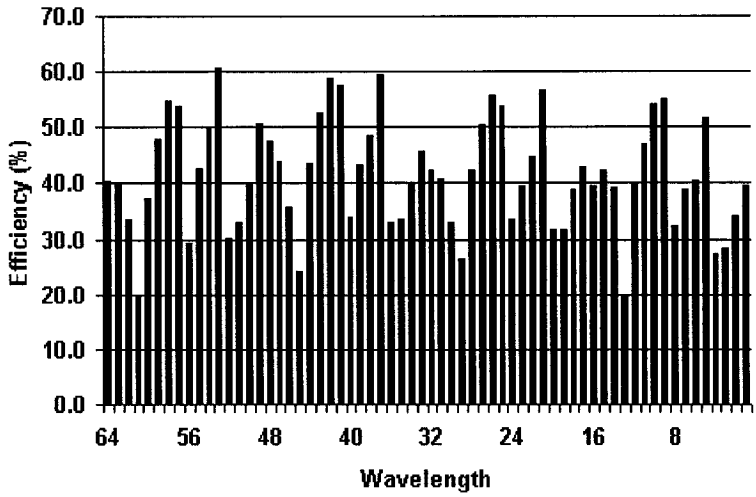

Fig. 52. Measured efficiency for all 64 facets of DOE2

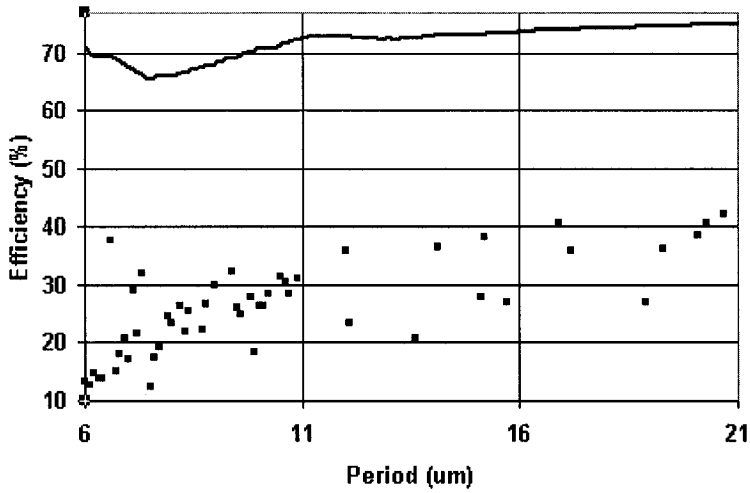

Fig. 53. DOE1 efficiency as a function of period
(continuous line is the calculated value, measured values are shown as points)

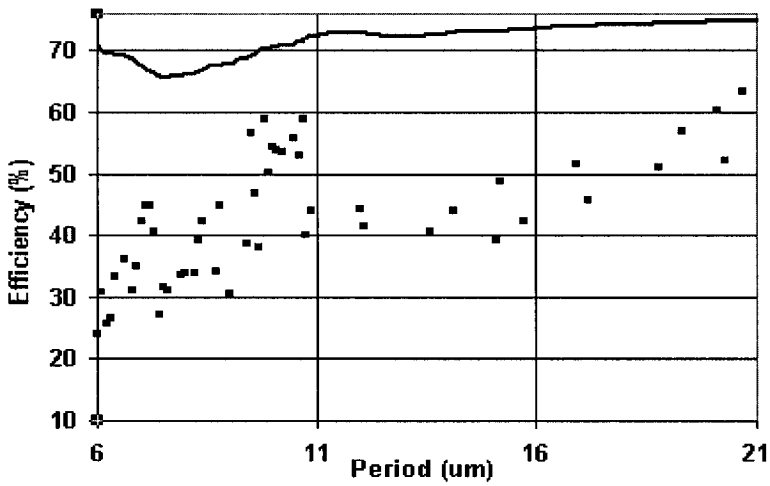

Fig. 54. DOE2 efficiency as a function of period
(continuous line is the calculated value, measured values are shown as points)

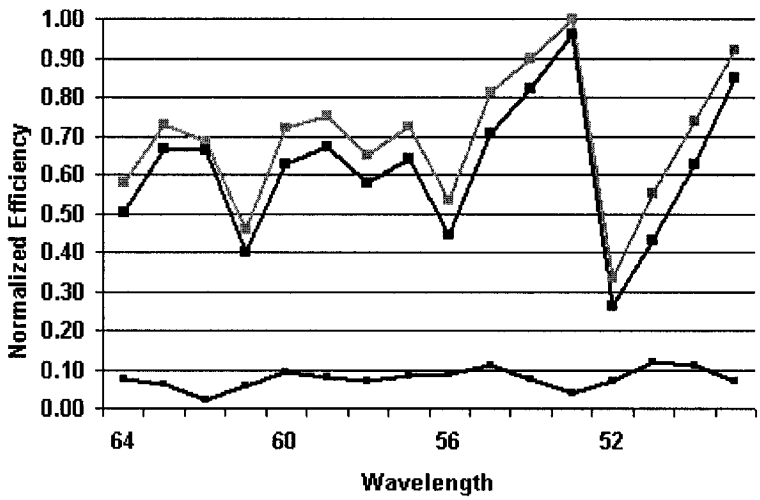

Fig. 55. DOE1 normalized efficiency for "best" and "worst" polarizations
(bottom curve is the difference)

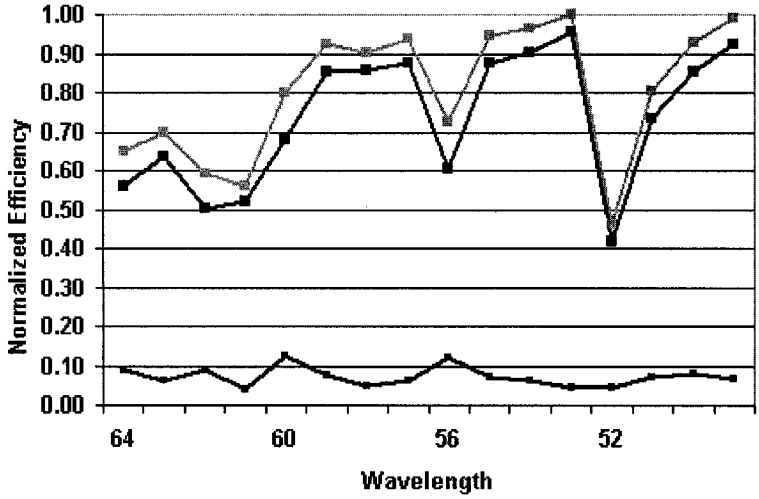

Fig. 56. DOE2 normalized efficiency for "best" and "worst" polarizations (bottom curve is the difference)

7.5 Efficiency and uniformity of the redirection module

This section compares the predicted (or calculated) efficiency and the actual (measured) efficiency. The predicted efficiency was calculated using the measurements of Section 7.4. Essentially, the efficiencies of each corresponding facet on DOE1 and DOE2 were multiplied to obtain the data shown in Fig. 57. The histogram corresponds to the measured results and the white line corresponds to the predicted results.

The average predicted efficiency of the redirection module is 11.0% while the average measured efficiency is 10.4%. Hence, at first glance, the data seems to correspond. However, even though the data for both measured and calculated efficiency follows the same general trend, the uniformity of the actual device is worse than predicted. That is, the standard deviation of the measured efficiency is 9.1% while that of the predicted efficiency is 5.1%. Due to the imprecision with which the device can be aligned with respect to the input beam (see Chapter 4), it was expected that the device perform more poorly than predicted. This is generally the case. However, there are several facets for which the efficiency greatly exceeds the predictions. There is a simple

explanation for this. The pinhole which was used to isolate the facets for power measurements had a diameter of 500 μm (250 μm was too small due to its circularity; the facets and microlenses are square-shaped) and hence, stray light (crosstalk) from the zero order messed up some of the measurements.

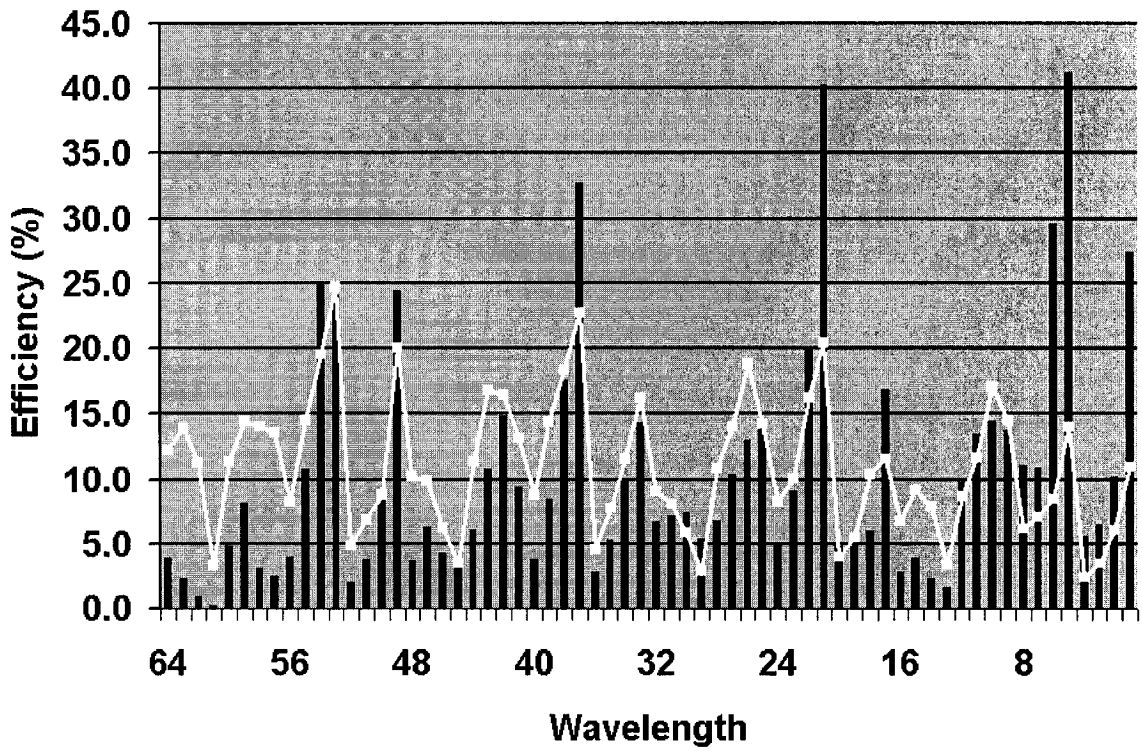

Fig. 57. Measured and calculated efficiency of the redirection module (bars are measured; white line is calculated)

7.6 Spatial power scan

Fig. 58 shows a spatial power scan of a large section (500 μm by 1000 μm) of the redirection module while facet 64 is redirected. It is quite clear that the zeroth order (which is diffracted by several gratings simultaneously) is extremely strong compared the redirected beam. The efficiency of the redirected beam is 2.4%. The efficiency of the same facet shown in Section 7.5 is 3.9%. The difference is due to the sampling of the beam when performing the spatial scan. The spatial scan also shows that the beam is somewhat Gaussian but suffers from aberrations. This is due to the misalignment of the input beam. The reader is reminded of Fig. 23 (in Chapter 4) which demonstrated that this type of misalignment would cause aberrations.

The zero order is 5.4 times more powerful than the redirected spot. Hence, the crosstalk of the device is extremely strong. Chapter 8 will present a method for reducing the crosstalk due to the strong zero order.

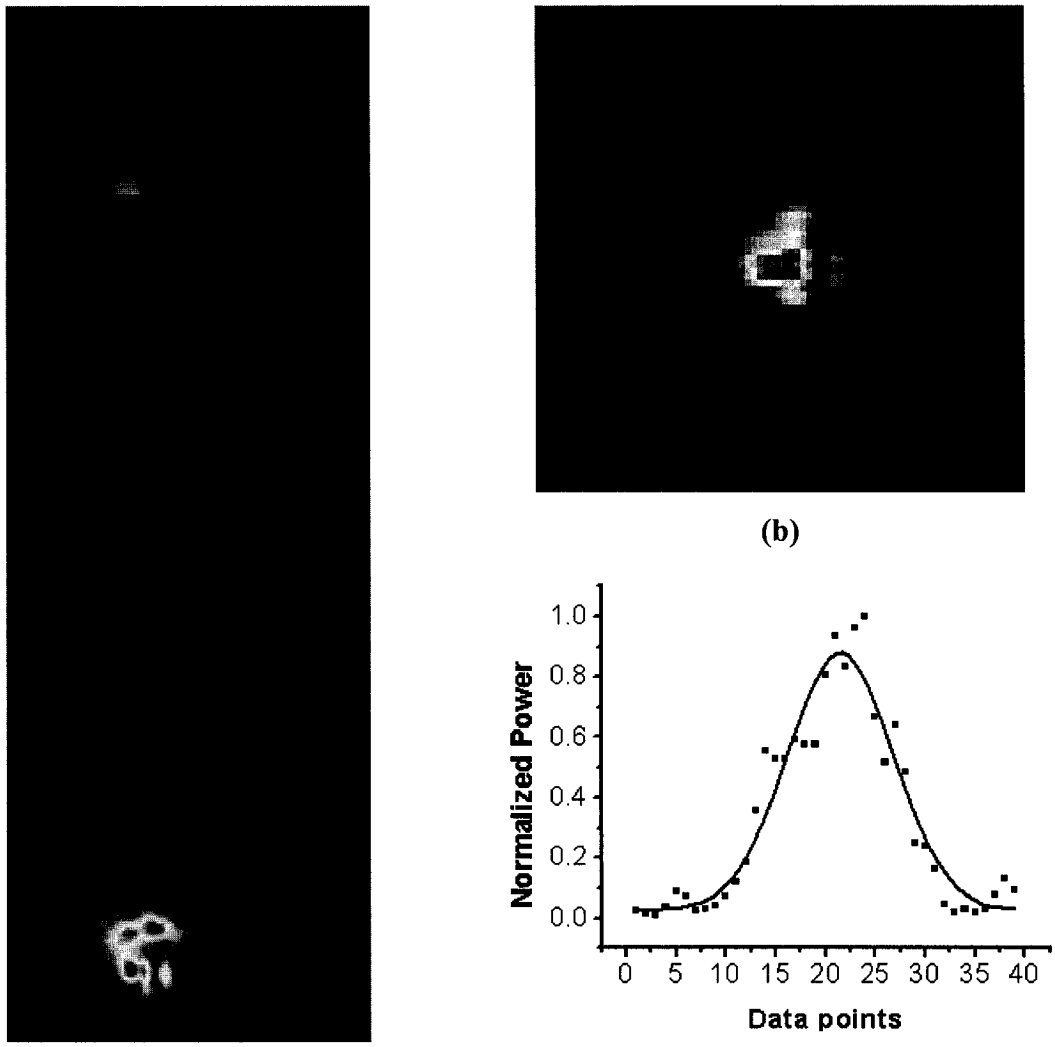

Fig. 58. Spatial power scan of wavelength 64
(a) wavelength 64 and zero order crosstalk; (b) zoom of wavelength 64;
(c) Gaussian fit of wavelength 64

7.7 Summary of the results

It is clear from the results presented in this section that the redirection module performed much more poorly than predicted in Chapter 4. The fabrication defects are the most important factor in decreasing the efficiency and uniformity of the device. As shown in Fig. 59, the defects also cause a significant amount of the energy to be found in

order 0, -1 and even +2. This type of noise causes crosstalk. In addition, Fig. 59 only demonstrates the noise of a single operating facet. If all 64 were to be in operation simultaneously, the crosstalk would be extremely severe. Measurements found that, on average, 25.1% of the energy is sent to order 0. This is 2.4 times more than the average efficiency of the redirected signals. Chapter 8 will present methods to improve efficiency and uniformity while decreasing crosstalk.

In summary, the average efficiency of the redirection module was measured to be 10.4% with a standard deviation of 9.1%. It is important to note that these measurements do not include the losses that would occur when integrating the module in a system. Extra losses could occur due to fiber coupling losses or misalignment at the MEMS, detector, or VCSEL arrays. The maximum average PDL was calculated to be 7.6% and 7.2% for DOE1 and DOE2, respectively giving a maximum average PDL of ~1.5dB.

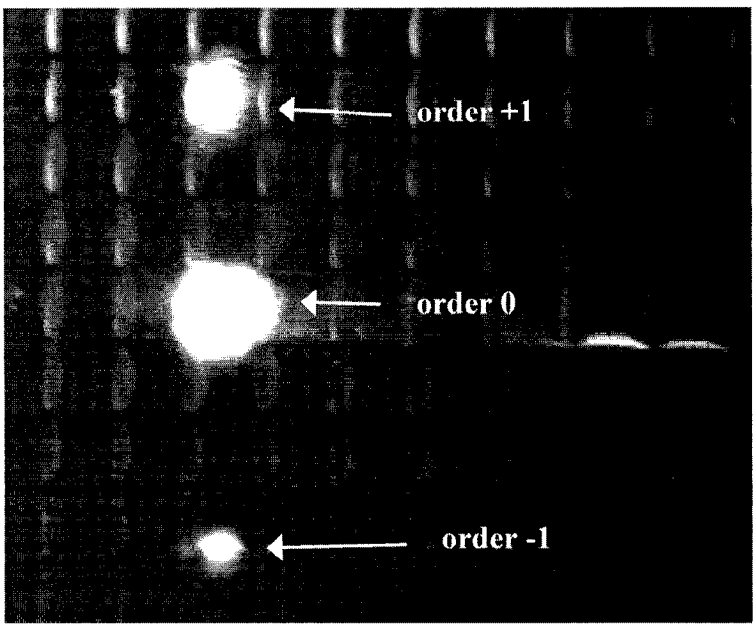

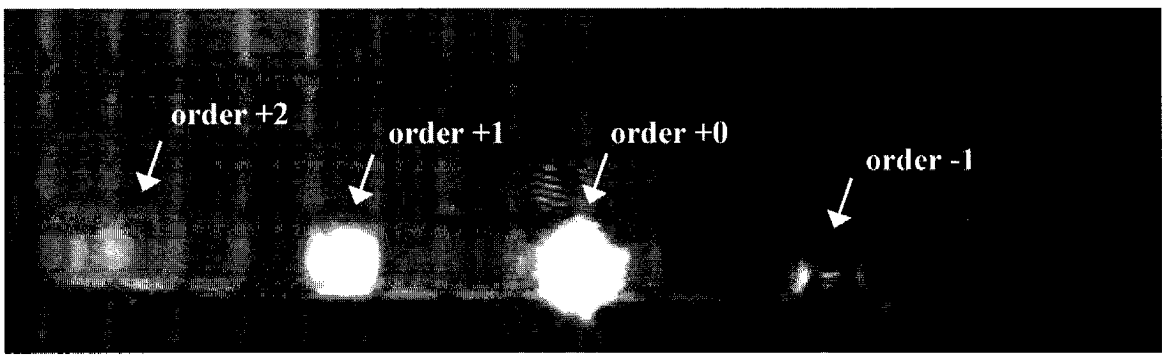

Fig. 59. Photographs illustrating crosstalk in the redirection module

8. FUTURE WORK

8.1 Introduction

It is clear from the experimental results detailed in Chapter 7 that the redirection module suffers from low efficiency, low uniformity and high crosstalk. The reader is reminded that the design and fabrication of the redirection module was done before the efficiency analysis presented in Chapter 4. A curve of grating efficiency (averaged for s and p polarization) versus period and wavelength for the type of grating used in the redirection module is shown in Fig. 60. It is quite obvious, looking at the simulation results, that using grating periods ranging from 6 μm to 11 μm has a detrimental impact on the efficiency and, very importantly, the uniformity of the device. In fact, the design presented in Chapter 3 uses periods ranging from 6 μm to 20.8 μm. Moreover, the etch depth of the gratings used in the design (calculated in Chapter 6) are not optimized for angle of incidence, period (blaze angle changes with period), or wavelength. In this chapter, techniques for enhancing the performance of the redirection module are explained. The techniques are discussed independently from each other but can all be implemented concurrently in a future design. First, using non-rasterized wavelength layout optimization is discussed. Next, the advantage of increasing the number of levels is explained. Third, the use of off-axis Fresnel lenses for simultaneously focusing and diffracting the light is presented. Fourth, etch depth optimization is detailed. Finally, a short justification for plastic injection molding is given.

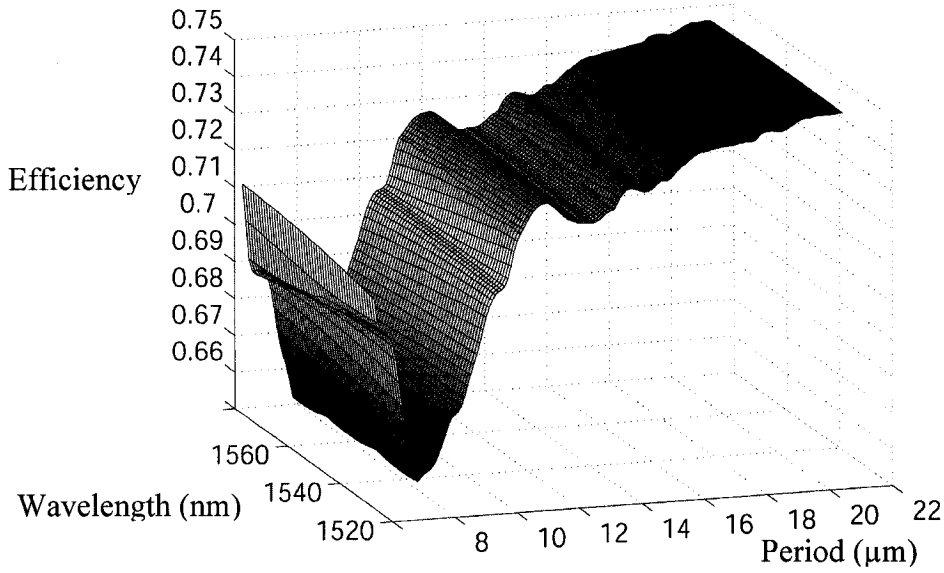

Fig. 60. Efficiency versus wavelength and grating period for a 4-level grating (average of S and P polarization)

8.2 Wavelength Mapping Optimization

As explained in Chapter 3, the mapping of the wavelengths was not optimized to reduce the length of the system. Each batch of 16 wavelengths is transformed to a 4x4 2D array that is rasterized. The system is scaled up to 64 wavelengths 16 wavelengths at a time. This type of wavelength mapping is not optimal. By running an exhaustive search, it is possible to find solutions for which the angular deflections needed to form the 2D array are less severe. Consequently, such a device would not need low-period (6 μm to 11 μm) gratings, which are inefficient, to form the 2D array and could be made significantly more efficient and uniform. It follows that increased efficiency lowers crosstalk.

Currently, the redirection module has DOE1 at the same coordinates as the top row (of the 2D array) of DOE2. Hence, all zero order light passing through DOE1 induces crosstalk. It is shown in Fig. 61 that the efficiency of the zeroth order, which has the most significant impact on crosstalk, can be kept below 5% at optimum groove depth

(discussed later) and with a period above 7 μm. A more clever way of reducing this crosstalk is to change the wavelength mapping such that the zero order light of DOE1 does not illuminate DOE2. Hence, DOE2 could be positioned above and/or below DOE1 either by moving the entire array up/down or by splitting it in half. An example of such a wavelength mapping is shown in Fig. 62. Although this does not increase efficiency or uniformity, it could potentially eliminate crosstalk.

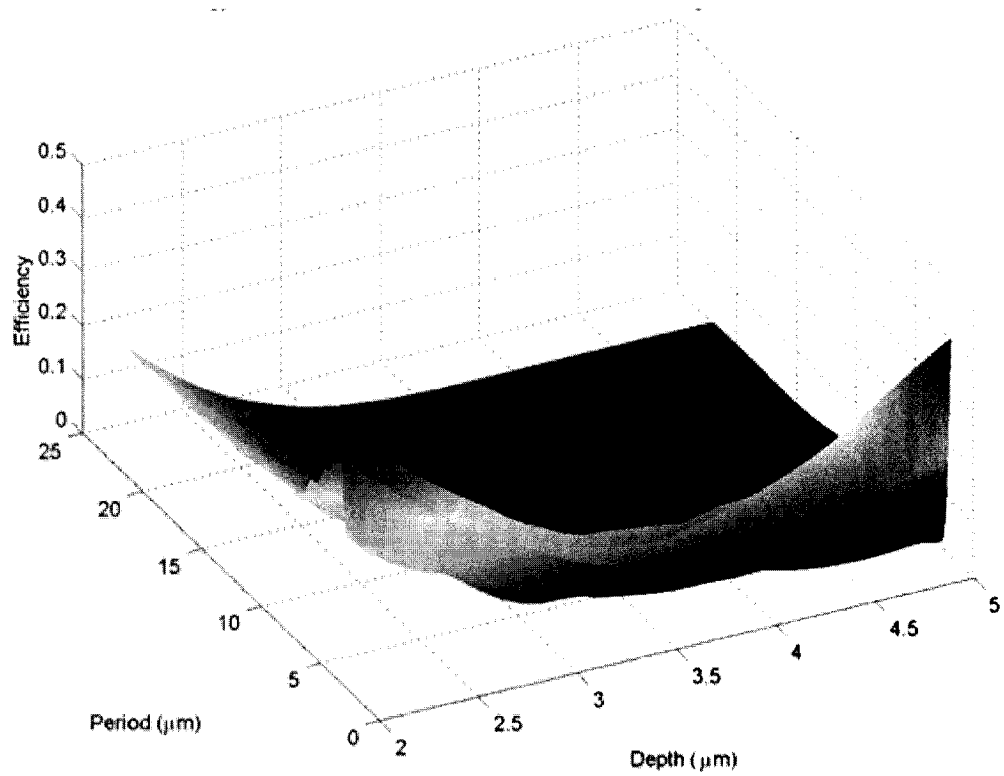

Fig. 61. Efficiency of zeroth order versus period and etch depth (4-level; 1550nm; TE)

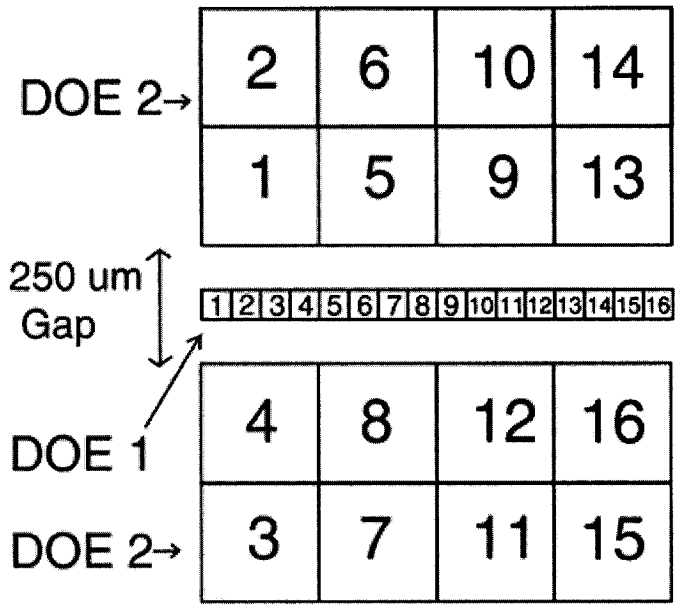

Fig. 62. Illustration of optimized wavelength mapping

8.3 Phase levels

Masks are needed at the rate of 2^n phase levels where n is the number of masks. Hence, multilevel gratings can be fabricated in 2, 4, 8, 16, etc. phase levels. The redirection module designed here had 4 phase levels with a fabrication technology having a minimum feature size of 1.5 μm translating to minimum grating period of 6 μm. If wavelength mapping optimization is performed and that a solution is found where only periods above 12 μm are used, then an extra 13.9% of efficiency could be achieved by using 8 phase level gratings. Using 16 level gratings would be impossible unless the vendor can etch extremely small feature sizes: 0.75 μm feature sizes for a minimum grating period of 12 μm. Hence it is clear that there is a tradeoff between grating period (thus deflection angle and length of the system) and the number of levels.

8.4 Off-axis Fresnel lenses

Using multilevel off-axis Fresnel lenses instead of the 4 level (or even 8 level) gratings can alleviate two significant problems in the design of the redirection module by simultaneously redirecting and focusing (relaying) the light beam. First, the microlens array and its assembly step could be eliminated. Second, the device length could be increased by having the off-axis Fresnel lens relay the incoming diverging light beam. A longer module permits the use of lower deflection angles (hence, bigger periods) to create the 2D array, which will increase efficiency and uniformity.

8.5 Etch depth optimization

The specification of the etch depth was given in Chapter 6. According to scalar theory, the maximum diffraction efficiency in the first order occurs with an etch depth of [1]:

$$d = \lambda/(n-1) \tag{20}$$

where d is the total etch depth, λ is the wavelength of operation and n is the refractive index of the substrate. First, note that the formula is wavelength dependent and that, ideally, the etch depth of each facet should be optimized with respect to wavelength. In addition, the etch depth can be optimized to take into account the period of the grating and the incidence angle of the beam onto the grating (this would only apply to the gratings used off axis, which is DOE2.) The optimized etch depth is:

$$d_{opt} = \frac{\lambda}{n\sqrt{1-[\sin(\theta_i)]^2} - \sqrt{1-\left[\frac{\lambda}{p} + n\sin(\theta_i)\right]^2}} \tag{21}$$

where d_{opt} is the optimized etch depth, λ is the wavelength of operation, p is the period, θ_i is the incident angle (calculated from the normal), and n is the refraction index of the material.

Another technique that could be used is the brute force computational approach. A software which uses rigorous diffraction theory to calculate diffraction efficiency can be used to optimize the etch depth for each facet of the system.

Considering the period, wavelength of operation, and angle of incidence is different for each of the 64 facets, the optimized etch depth would be different for each facet as well. Consequently, the fabrication of the substrates would be much more complex and costly. A greyscale mask would thus be needed for these types of DOEs to be fabricated.

8.6 Plastic Injection Molding

If this device is to be commercially produced, the cost of fabrication of the device would need to be lowered and manufacturing capacity increased. As explained in Chapter 3, the substrates are glued back-to-back so that the features are on the outside. Therefore, it is feasible that this device could be molded by plastic injection from a high-quality master. In addition, to save an extra fabrication step, the master should be designed with off-axis Fresnel lenses to remove the need for a microlens array.

8.7 Summary

As mentioned in the introduction, the future work detailed above can all be implemented simultaneously for maximum improvement of the efficiency, uniformity, and crosstalk. That is, multilevel (8 level) off-axis Fresnel lenses whose etch depths have been optimized with optimized wavelength mapping would provide a compact micro-optical device whose performance characteristics are superior to the redirection module studied in Chapter 7.

8.8 References

[1] B. Kress and P. Meyrueis, Digital Diffractive Optics: An Introduction to Planar Diffractive Optics and Related Technology, John Wiley & Sons, (2000).

9. CONCLUSION

This thesis has presented an investigation of two-dimensional formatting for dense wavelength division multiplexing. First and foremost, the need for two-dimensional formatting was justified by the emergence of two important technologies: micro-electromechanical system (MEMS) optical switches, which can provision or protect wavelengths at speeds of milliseconds and two-dimensional parallel multi-wavelength optical interconnects (2D-POIs) which enable high-density, high-bandwidth communications between VLSI chips in the computing environment and dense wavelength division optical networks. Having justified the need and explained the conceptualization of such a device, the specific objectives of the project were listed in Chapter 2. Chapter 3 explained the design of the redirection module while Chapter 4 detailed simulations and optimization of the device. Chapter 5 presented the design of a simple grating-based (de)multiplexer that could interface with the redirection module. Chapter 6 explained the packaging, fabrication, and assembly of the redirection module. Chapter 7 detailed the test procedure and presented the experimental performance of the redirection module. The results in Chapter 7 demonstrated that the redirection module performed much more poorly than predicted in Chapter 4. Finally, Chapter 8 listed important future work that could be implemented to improve the performance of the redirection module.

The implementation of the system using multilevel multifacet gratings for beam mapping demonstrated the practical feasibility of incorporating these free-space micro-optical devices to interface between WDM optical networks and 2D-POIs and 2D WDM interconnects. It is, to the author's knowledge, the only two-dimensional beam mapping technique to have been implemented and tested for use in WDM optical networks. As mentioned in Chapter 3, the device is scalable 16 wavelengths at a time with a linear scale factor $1/4^{th}$ that of a one-dimensional (de)multiplexer. The average efficiency of the device was measured to be 10.4% with a standard deviation of 9.1%. Essentially, the departure from scalar theory caused high losses and greater non-uniformity. However, Chapter 8 presented several methods by which efficiency, uniformity and crosstalk could

be improved. Most importantly, it was learned that the device should be implemented with periods higher than 11 μm. Moreover, as shown in Fig. 62, wavelength mapping can be optimized to increase the minimum period used in the design (thus increasing efficiency and uniformity) and to avoid zero-order crosstalk.

Although several techniques were listed in Chapter 8 to improve the design of the redirection module, none address the most critical and practical issues that would make the device feasible to integrate in systems, such as: grating fabrication, polarization dependent loss, thermal stability, implementation and alignment of the redirection module, and implementation and alignment of the dispersion module with the redirection module.

The most critical issue governing the performance of the redirection module is the quality of the gratings. Although techniques such as increasing the number of phase levels and using efficient grating periods of greater than 10 μm can significantly increase the theoretical efficiency of the device, they do not address the underlying difficulty of producing high quality gratings. This is especially important for those gratings, on DOE1, which have only a few illuminated periods.

Due to the use of gratings, the device exhibits maximum average PDL of ~1.5dB. Considering that all the facets have gratings with different orientations, there is no simple way of mitigating this affect. An analysis could be performed to determine the polarization that has the least amount of PDL and the system could be implemented using polarization diversity. However, this technique would add complexity because two redirection modules would need to be implemented.

Chapter 4 presented the misalignment analysis. The thermal expansion or contraction of the device could potentially increase the misalignment loss. For this device to be practical, the effect of temperature changes on the module should be investigated and compared to the misalignment graphs. If the effect is important, than active temperature control of the device could be necessary. Another would be to find a material whose index of refraction change (due to thermal changes) counteracts the thermal expansion of contraction of the device.

The next most important issue is the implementation and alignment of the redirection module. As demonstrated in Chapter 4, the two most critical alignments (the microlens array and the input beam with respect to the system) are those that have no precision alignment techniques. That is, the microlens array does not have alignment features such as interferometric lenses. And the input beam cannot be made precisely perpendicular to the system and therefore, the device suffers clipping losses and diffraction effects at DOE2 and the microlens array. Therefore, a technique should be devised to ensure beam perpendicularity at the input.

Although it was demonstrated that a simple grating-based one-dimensional optical wavelength (de)multiplexer can be designed to interface between a fiber containing a WDM signal and the redirection module, implementing the two devices to work together is difficult. The most critical issue is the alignment of the output from the dispersion module to the input of the redirection module. As mentioned in the previous paragraph, to avoid clipping and diffraction effects, the input beam must be perpendicular to the substrate. Second, the available commercial products typically used to (de)multiplex WDM signals are arrayed waveguide gratings and etched grating (de)multiplexers. These technologies have waveguides whose output beams are not Gaussian. Moreover, the waist size of these non-Gaussian beams is not compatible with the facet size of DOE1. Therefore, the module would need to be re-designed to take into account these changes. The new design could employ microlenses or Fresnel lenses on the input. Or, the output waveguides could be modified to be compatible with the input of the redirection module.

In summary, the redirection module successfully performed the reformatting of a one-dimensional linear array to a two-dimensional output array for use in MEMS optical switches or as the interface between optical networks and VLSI two-dimensional parallel optical interconnects. Although the experimental results demonstrated poor efficiency, the technology could feasibly be integrated in systems by solving the critical issues listed above and implementing the design improvements listed in Chapter 8.

APPENDIX A: FACET SIZES

Table 6 gives the pitch between the centers of adjacent facets of DOE 1.

Facet Number	Size in x (μm)	Pitch Between Centers (μm)		
		From	To	Distance
1	62.50	1	2	62.55
2	62.60	2	3	62.60
3	62.60	3	4	62.65
4	62.70	4	5	62.75
5	62.80	5	6	62.80
6	62.80	6	7	62.85
7	62.90	7	8	63.00
8	63.10	8	9	63.05
9	63.00	9	10	63.05
10	63.10	10	11	63.20
11	63.30	11	12	63.30
12	63.30	12	13	63.30
13	63.30	13	14	63.35
14	63.40	14	15	63.45
15	63.50	15	16	63.55
16	63.60	16	17	63.65
17	63.70	17	18	63.70
18	63.70	18	19	63.75
19	63.80	19	20	63.80
20	63.80	20	21	63.90
21	64.00	21	22	64.00
22	64.00	22	23	64.05
23	64.10	23	24	64.15
24	64.20	24	25	64.20
25	64.20	25	26	64.25
26	64.30	26	27	64.35
27	64.40	27	28	64.40
28	64.40	28	29	64.50
29	64.60	29	30	64.60
30	64.60	30	31	64.65
31	64.70	31	32	64.75
32	64.80	32	33	64.80
33	64.80	33	34	64.85
34	64.90	34	35	64.90
35	64.90	35	36	65.00
36	65.10	36	37	65.15
37	65.20	37	38	65.20

Facet Number	Size in x (μm)	Pitch Between Centers (μm)		
		From	To	Distance
38	65.20	38	39	65.25
39	65.30	39	40	65.35
40	65.40	40	41	65.40
41	65.40	41	42	65.50
42	65.60	42	43	65.55
43	65.50	43	44	65.60
44	65.70	44	45	65.75
45	65.80	45	46	65.80
46	65.80	46	47	65.85
47	65.90	47	48	65.95
48	66.00	48	49	66.05
49	66.10	49	50	66.10
50	66.10	50	51	66.15
51	66.20	51	52	66.25
52	66.30	52	53	66.35
53	66.40	53	54	66.45
54	66.50	54	55	66.50
55	66.50	55	56	66.55
56	66.60	56	57	66.65
57	66.70	57	58	66.75
58	66.80	58	59	66.80
59	66.80	59	60	66.85
60	66.90	60	61	66.95
61	67.00	61	62	67.05
62	67.10	62	63	67.20
63	67.30	63	64	67.20
64	67.10	--	--	--

Table 6. Facet sizes

APPENDIX B: SUBSTRATE LAYOUT

B.1 Coordinate System

The coordinates system used for both substrates is shown on Fig. 63. Unless specified, the dimensions are given in micrometers (μm).

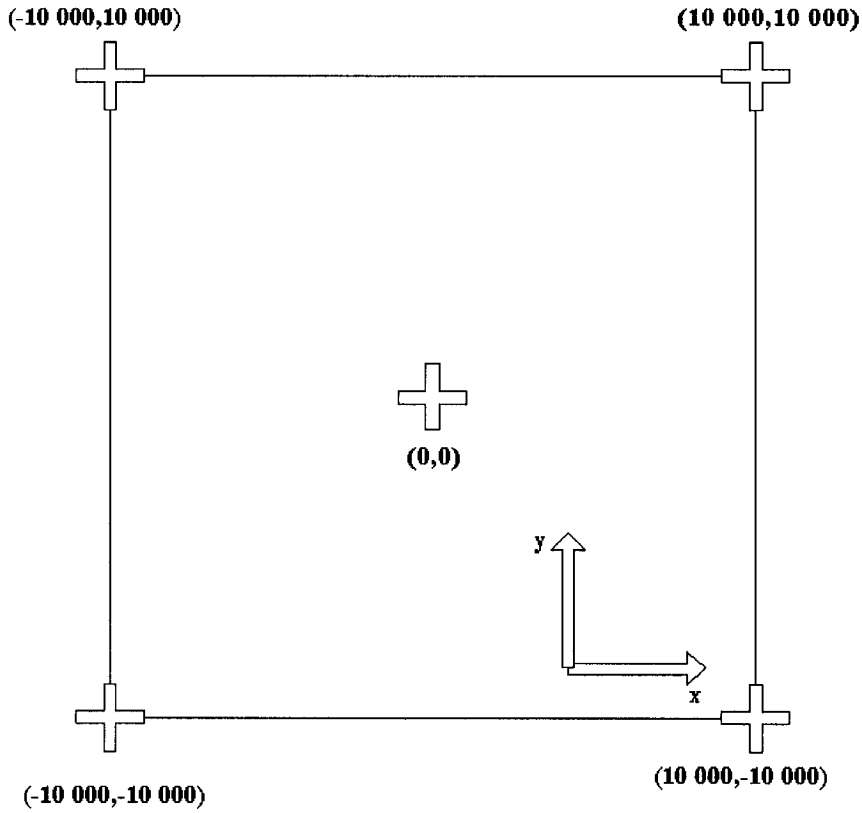

Fig. 63. Reference coordinate system

B.2 DOE 1 Layout

DOE 1 consists of 64 facets along a horizontal line as illustrated in Fig. 64. Note that the drawing is not to scale and that only 48 facets are drawn for simplicity. The line of facets is centered on the substrate. Each facet measures 62.5 μm in the y direction. In the x direction, the facet size increase from left to right, starting at 62.5 μm and ending at 67.3 μm (see Appendix A.) Table 7 provides the specifications of the facets of DOE1. The facet numbers were given from left to right. The coordinates given in the table are of the center of the facets.

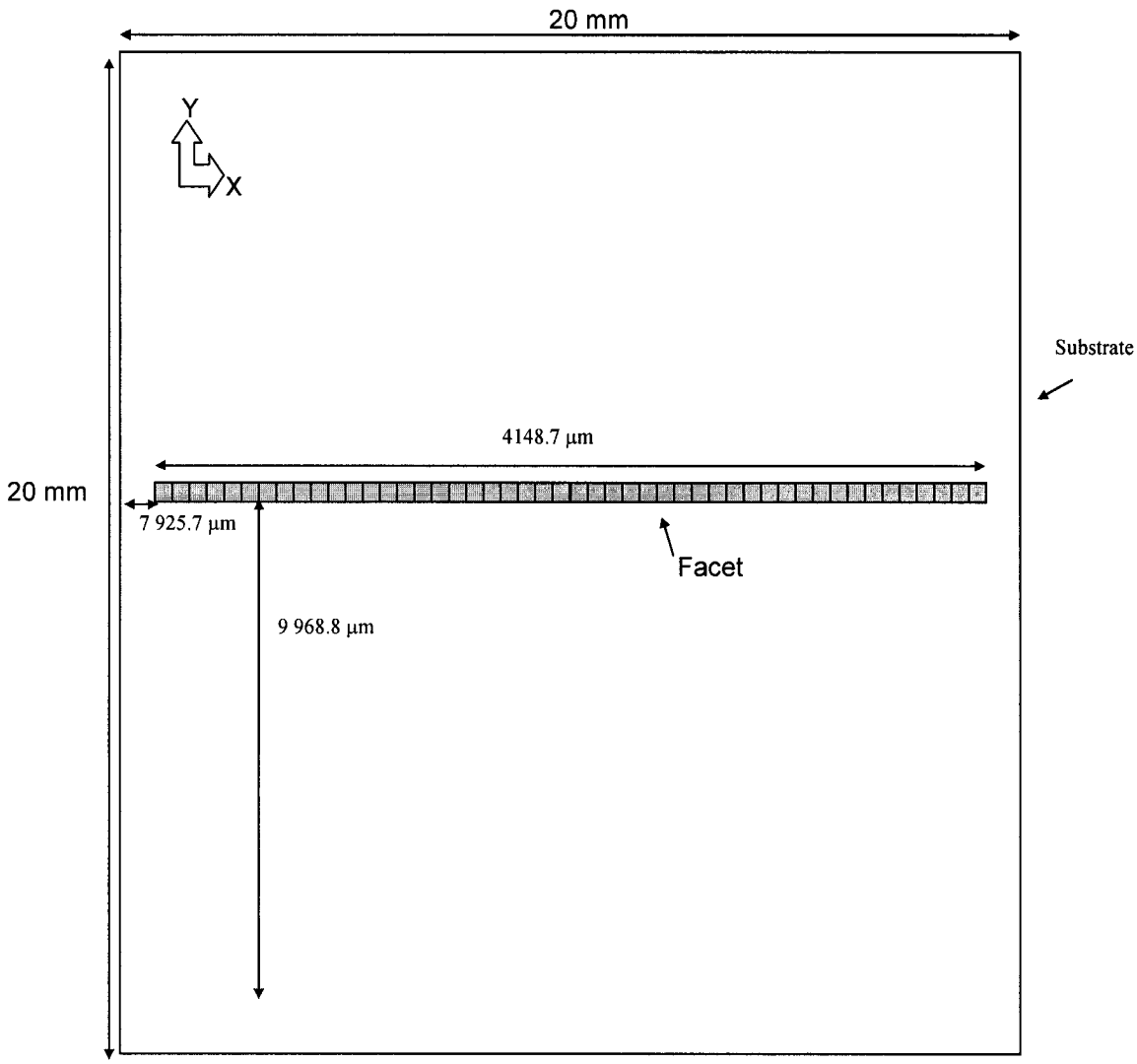

Fig. 64. Schematic of the layout of DOE1

Facet Number	Coordinates (μm)		Period in x	Period in y	Period	Size in x (μm)
	x	y				
1	-2043.05	0.00	15.10	-354.30	-15.09	62.50
2	-1980.50	0.00	10.00	-354.50	-10.00	62.60
3	-1917.90	0.00	7.50	-354.70	-7.50	62.60
4	-1855.25	0.00	6.00	-354.90	-6.00	62.70
5	-1792.50	0.00	52.00	-20.20	-18.83	62.80
6	-1729.70	0.00	18.50	-20.20	-13.64	62.80
7	-1666.85	0.00	11.30	-20.20	-9.86	62.90
8	-1603.85	0.00	8.20	-20.20	-7.60	63.10
9	-1540.80	0.00	-35.80	-10.50	10.08	63.00
10	-1477.75	0.00	141.60	-10.50	-10.47	63.10
11	-1414.55	0.00	23.80	-10.50	-9.61	63.30
12	-1351.25	0.00	13.10	-10.50	-8.19	63.30
13	-1287.95	0.00	-13.40	-7.20	6.34	63.30
14	-1224.60	0.00	-24.90	-7.20	6.92	63.40
15	-1161.15	0.00	-185.20	-7.20	7.19	63.50
16	-1097.60	0.00	34.00	-7.20	-7.04	63.60
17	-1033.95	0.00	15.70	-357.20	-15.69	63.70
18	-970.25	0.00	10.20	-357.40	-10.20	63.70
19	-906.50	0.00	7.60	-357.60	-7.60	63.80
20	-842.70	0.00	6.10	-357.80	-6.10	63.80
21	-778.80	0.00	60.50	-20.30	-19.25	64.00
22	-714.80	0.00	19.60	-20.30	-14.10	64.00
23	-650.75	0.00	11.80	-20.30	-10.20	64.10
24	-586.60	0.00	8.50	-20.40	-7.85	64.20
25	-522.40	0.00	-32.10	-10.60	10.07	64.20
26	-458.15	0.00	297.40	-10.60	-10.59	64.30
27	-393.80	0.00	26.50	-10.60	-9.84	64.40
28	-329.40	0.00	13.90	-10.60	-8.43	64.40
29	-264.90	0.00	-12.80	-7.20	6.28	64.60
30	-200.30	0.00	-22.60	-7.20	6.86	64.60
31	-135.65	0.00	-99.20	-7.20	7.18	64.70
32	-70.90	0.00	41.30	-7.20	-7.09	64.80
33	-6.10	0.00	17.20	-360.20	-17.18	64.80

Facet Number	Coordinates (μm)		Period in x	Period in y	Period	Size in x (μm)
	x	y				
34	58.75	0.00	10.90	-360.40	-10.90	64.90
35	123.65	0.00	8.00	-360.60	-8.00	64.90
36	188.65	0.00	6.40	-360.70	-6.40	65.10
37	253.80	0.00	96.30	-20.50	-20.05	65.20
38	319.00	0.00	22.50	-20.50	-15.15	65.20
39	384.25	0.00	12.80	-20.50	-10.86	65.30
40	449.60	0.00	9.00	-20.50	-8.24	65.40
41	515.00	0.00	-26.50	-10.60	9.84	65.40
42	580.50	0.00	-264.80	-10.70	10.69	65.60
43	646.05	0.00	33.20	-10.70	-10.18	65.50
44	711.65	0.00	15.70	-10.70	-8.84	65.70
45	777.40	0.00	-11.70	-7.30	6.19	65.80
46	843.20	0.00	-19.30	-7.30	6.83	65.80
47	909.05	0.00	-54.90	-7.30	7.24	65.90
48	975.00	0.00	64.10	-7.30	-7.25	66.00
49	1041.05	0.00	20.30	-363.20	-20.27	66.10
50	1107.15	0.00	12.10	-363.40	-12.09	66.10
51	1173.30	0.00	8.70	-363.60	-8.70	66.20
52	1239.55	0.00	6.80	-363.80	-6.80	66.30
53	1305.90	0.00	1331.50	-20.70	-20.70	66.40
54	1372.35	0.00	29.20	-20.70	-16.89	66.50
55	1438.85	0.00	14.80	-20.70	-12.04	66.50
56	1505.40	0.00	10.00	-20.70	-9.00	66.60
57	1572.05	0.00	-20.90	-10.70	9.52	66.70
58	1638.80	0.00	-69.50	-10.70	10.58	66.80
59	1705.60	0.00	52.50	-10.80	-10.58	66.80
60	1772.45	0.00	19.10	-10.80	-9.40	66.90
61	1839.40	0.00	-10.50	-7.30	5.99	67.00
62	1906.45	0.00	-15.90	-7.30	6.63	67.10
63	1973.65	0.00	-33.60	-7.30	7.13	67.30
64	2040.85	0.00	287.50	-7.30	-7.30	67.10

Table 7. Specifications of the facets of DOE1

B.3 DOE 2 Layout

For DOE 2, the facets are disposed in a 4×16 array. The square facets are 250 μm on the sides. **The array is not centred on the substrate; there is an offset of 228 μm in the x direction and of –890 μm in the y direction between the centre of the array and the centre of the substrate**. Table 8 describes specifications of the facets of DOE2. The facet numbers are from the top left corner to the bottom right corner as shown in. Note that the facet numbers do not correspond to the wavelength mapping.

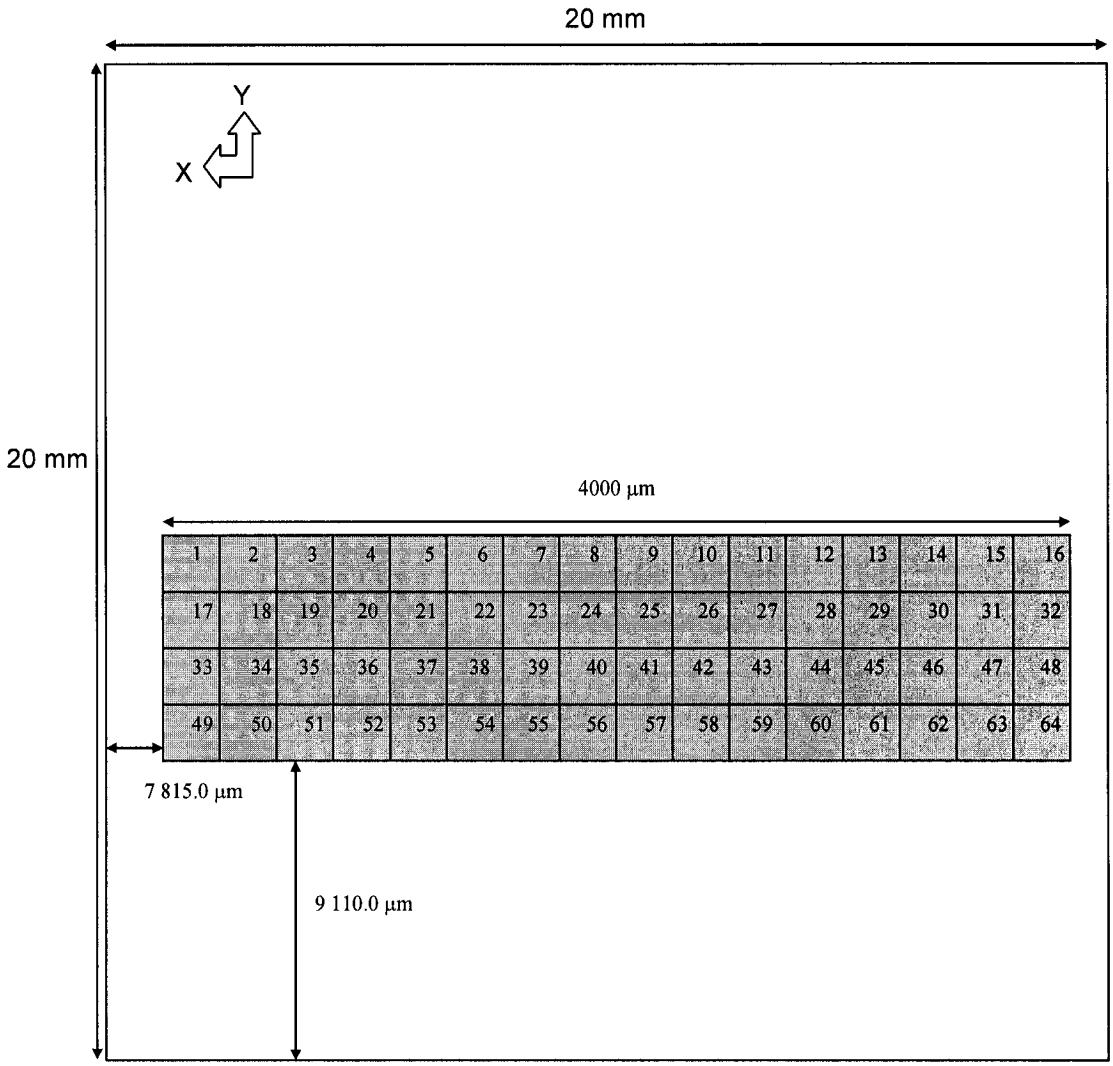

Fig. 65. Schematic of the layout of DOE2

Facet Number	Coordinates (μm)		Period in x	Period in y	Period
	x	y			
1	2060.0	-15.00	6.80	-363.80	-6.80
2	1810.0	-15.00	8.70	-363.60	-8.70
3	1560.0	-15.00	12.10	-363.40	-12.09
4	1310.0	-15.00	20.30	-363.20	-20.27
5	1060.0	-15.00	6.40	-360.70	-6.40
6	810.0	-15.00	8.00	-360.60	-8.00
7	560.0	-15.00	10.90	-360.40	-10.90
8	310.0	-15.00	17.20	-360.20	-17.18
9	60.0	-15.00	6.10	-357.80	-6.10
10	-190.0	-15.00	7.60	-357.60	-7.60
11	-440.0	-15.00	10.20	-357.40	-10.20
12	-690.0	-15.00	15.70	-357.20	-15.69
13	-940.0	-15.00	6.00	-354.90	-6.00
14	-1190.0	-15.00	7.50	-354.70	-7.50
15	-1440.0	-15.00	10.00	-354.50	-10.00
16	-1690.0	-15.00	15.10	-354.30	-15.09
17	2060.0	-265.00	10.00	-20.70	-9.00
18	1810.0	-265.00	14.80	-20.70	-12.04
19	1560.0	-265.00	29.20	-20.70	-16.89
20	1310.0	-265.00	1331.50	-20.70	-20.70
21	1060.0	-265.00	9.00	-20.50	-8.24
22	810.0	-265.00	12.80	-20.50	-10.86
23	560.0	-265.00	22.50	-20.50	-15.15
24	310.0	-265.00	96.30	-20.50	-20.05
25	60.0	-265.00	8.50	-20.40	-7.85
26	-190.0	-265.00	11.80	-20.30	-10.20
27	-440.0	-265.00	19.60	-20.30	-14.10
28	-690.0	-265.00	60.50	-20.30	-19.25
29	-940.0	-265.00	8.20	-20.20	-7.60
30	-1190.0	-265.00	11.30	-20.20	-9.86
31	-1440.0	-265.00	18.50	-20.20	-13.64
32	-1690.0	-265.00	52.00	-20.20	-18.83

Facet Number	Coordinates (μm)		Period in x	Period in y	Period
	x	y			
33	2060.0	-515.00	19.10	-10.80	-9.40
34	1810.0	-515.00	52.50	-10.80	-10.58
35	1560.0	-515.00	-69.50	-10.70	10.58
36	1310.0	-515.00	-20.90	-10.70	9.52
37	1060.0	-515.00	15.70	-10.70	-8.84
38	810.0	-515.00	33.20	-10.70	-10.18
39	560.0	-515.00	-264.80	-10.70	10.69
40	310.0	-515.00	-26.50	-10.60	9.84
41	60.0	-515.00	13.90	-10.60	-8.43
42	-190.0	-515.00	26.50	-10.60	-9.84
43	-440.0	-515.00	297.40	-10.60	-10.59
44	-690.0	-515.00	-32.10	-10.60	10.07
45	-940.0	-515.00	13.10	-10.50	-8.19
46	-1190.0	-515.00	23.80	-10.50	-9.61
47	-1440.0	-515.00	141.60	-10.50	-10.47
48	-1690.0	-515.00	-35.80	-10.50	10.08
49	2060.0	-765.00	287.50	-7.30	-7.30
50	1810.0	-765.00	-33.60	-7.30	7.13
51	1560.0	-765.00	-15.90	-7.30	6.63
52	1310.0	-765.00	-10.50	-7.30	5.99
53	1060.0	-765.00	64.10	-7.30	-7.25
54	810.0	-765.00	-54.90	-7.30	7.24
55	560.0	-765.00	-19.30	-7.30	6.83
56	310.0	-765.00	-11.70	-7.30	6.19
57	60.0	-765.00	41.30	-7.20	-7.09
58	-190.0	-765.00	-99.20	-7.20	7.18
59	-440.0	-765.00	-22.60	-7.20	6.86
60	-690.0	-765.00	-12.80	-7.20	6.28
61	-940.0	-765.00	34.00	-7.20	-7.04
62	-1190.0	-765.00	-185.20	-7.20	7.19
63	-1440.0	-765.00	-24.90	-7.20	6.92
64	-1690.0	-765.00	-13.40	-7.20	6.34

Table 8. Specifications of the facets of DOE2

APPENDIX C: COLLIMATING SYSTEM

The collimating system takes the output beam of an OZ-coupler and changes the beam waist to 20.3 μm. Lens 1 has a focal length of 500 mm and lens 2 has a focal length of 15 mm.

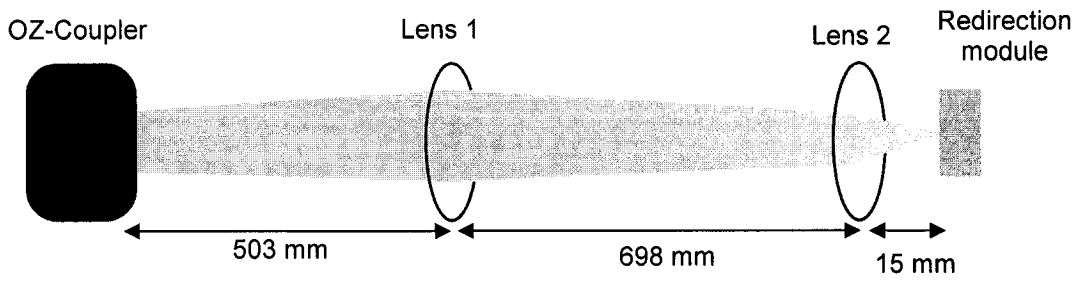

Fig. 66. Collimating System